2022-05-01

# Application of the Continuum Damage Mechanics Wilshire-Cano-Stewart (WCS) Model

Jaime Aaron Cano
*The University of Texas at El Paso*

APPLICATION OF THE CONTINUUM DAMAGE MECHANICS WILSHIRE-CANO-STEWART (WCS) MODEL

JAIME AARON CANO ESCAMILLA

Doctoral Program in Mechanical Engineering

APPROVED:

Calvin M. Stewart, Ph.D., Chair

Yirong Lin, Ph.D.

Jack Chessa, Ph.D.

Cesar Carrasco, Ph.D.

Alejandra G. Castellanos, Ph.D.

Stephen L. Crites, Jr., Ph.D.
Dean of the Graduate School

## DEDICATION

Dedicated to my calling to God

“Ad maiorem Dei gloriam”

# APPLICATION OF THE CONTINUUM DAMAGE MECHANICS WILSHIRE-CANO-STEWART (WCS) MODEL

by

JAIME AARON CANO ESCAMILLA, M.S

DISSERTATION

Presented to the Faculty of the Graduate School of

The University of Texas at El Paso

in Partial Fulfillment

of the Requirements

for the Degree of

DOCTOR OF PHILOSOPHY

Department of Mechanical Engineering

THE UNIVERSITY OF TEXAS AT EL PASO

May 2022

## ACKNOWLEDGEMENTS

I would like to thank my mentor and supervisor Dr. Calvin M. Stewart for his guidance and mentorship during my graduate studies. Through his mentorship I was able to complete this journey. I would also want to thank my parents who constantly supported me and allowed me to purse higher education. Only through their guidance and support I was able to achieve this goal. I would also like to thank my future wife. Her company, advice, and support pushed me to become better which is crucial for the completion of my studies. This is dedicated to her and to the future family that we are building. Lastly, I would like to thank God, as He is the one that allowed me to explore the beauty of scientific research and the One who put the desired of knowledge in my heart.

## ABSTRACT

In this study, the applications of the continuum damage mechanics-based Wilshire-Cano-Stewart (WCS) model are explored to predict rupture time, minimum-creep-strain-rate (MCSR), damage, damage evolution, and creep deformation. Increase knowledge in manufacturing methods has pushed the limit of material science and the development of new materials. Conventional testing is required to qualify materials against creep which according to the ASME B&PV III code, 10,000+ hours of experiments are necessary for each heat before materials are put into service. This process is costly and not feasible for new materials. As an alternative, models have been employed to predict creep behaviors and reduce the amount of time necessary for material qualification. Many models have been developed to predict distinct creep behaviors and the question of which model is best remains. Amongst current models, the WCS model has emerge with the ability to predict multiple behaviors using an explicit analytical approach with the ability to predict long-term creep. In this study the novel continuum damage mechanics WCS is employed in multiple applications. The goals of the study are (a) to discuss and determine the framework of the WCS model and validated it mathematically and using parametric simulations, (b) applied the model to accelerated creep data to show the capabilities of the model with non-conventional data, and (c) applied a novel numerical method, the datum temperature method (DTM) to show the model extrapolations and interpolations capabilities with limited and reduce data sets. To accomplish these goals, data is gathered for alloy P91 and Inconel 718 to develop and post-audit validate the model. The benefits of using the WCS model is that it provides an explicit stress and temperature dependency ideal for extrapolations, the coupled equations are suitable for finite element analysis (FEA) implementation, and it follows an explicit calibration approach. The model also proves that it can be applied to accelerated testing data and using the DTM.

## TABLE OF CONTENTS

## LIST OF TABLES

## LIST OF FIGURES

# CHAPTER 1 INTRODUCTION

## 1.1 Motivation

Increase knowledge in advance manufacturing methods, such as additive manufacturing, has increased the development of new materials. Most of these materials are desired for high-temperature applications such as power plants, aerospace, boilers, pressure vessels, etc. [1]. An example of such applications are the Advance Ultrasupercritical (A-USC) and Fossil Energy (FE) power plants that have designs with steam pressures exceeding 4000 psi with temperatures ranging from $0.3T_m < T < 0.6T_m$, where $T_m$ is the melting temperature of alloys. Another example are industrial gas turbines (IGTs) where the hot gas path requires understanding of mechanical and material properties to operate successfully [2]. Examples of components required to operate at high temperatures is shown in Figure 1.1 for IGTs, GIGATOP 4-pole generator, and a boiler component. Most failures that occur in high temperature applications and components (A-USC, FE components, IGTs, generators, boilers, pressure vessels), as shown in Figure 1.2, are caused by creep, fatigue, creep-fatigue, and combined damage factors [3-5]. In, Figure 1.2 multiple case studies of creep failures are shown for an IGT, a fastened threaded rod, and a turbine blade. To prevent this, maintenance and material qualification must be performed. The maintenance cost in IGTs is a concern as they are performed every 2 years for component changes and 4 to 5 years for a major inspection [8]. In this time, catastrophic failures can occur. New emerging materials required to work under this high temperature conditions, must be qualify for long-term ($\geq 10^5$ hrs.) creep resistance. The average time to qualify new creep-resistant materials is between 10 to 20 years [10-12]. The ASME B&PV III code calls for creep tests out to 10,000+ hours per heat of material [11]. This process is not cost effective and delays the use of innovative materials as

companies decide to use conventional materials instead. There is a need for rapid qualification of materials, especially with methods that are cost efficient such as the use of creep models.

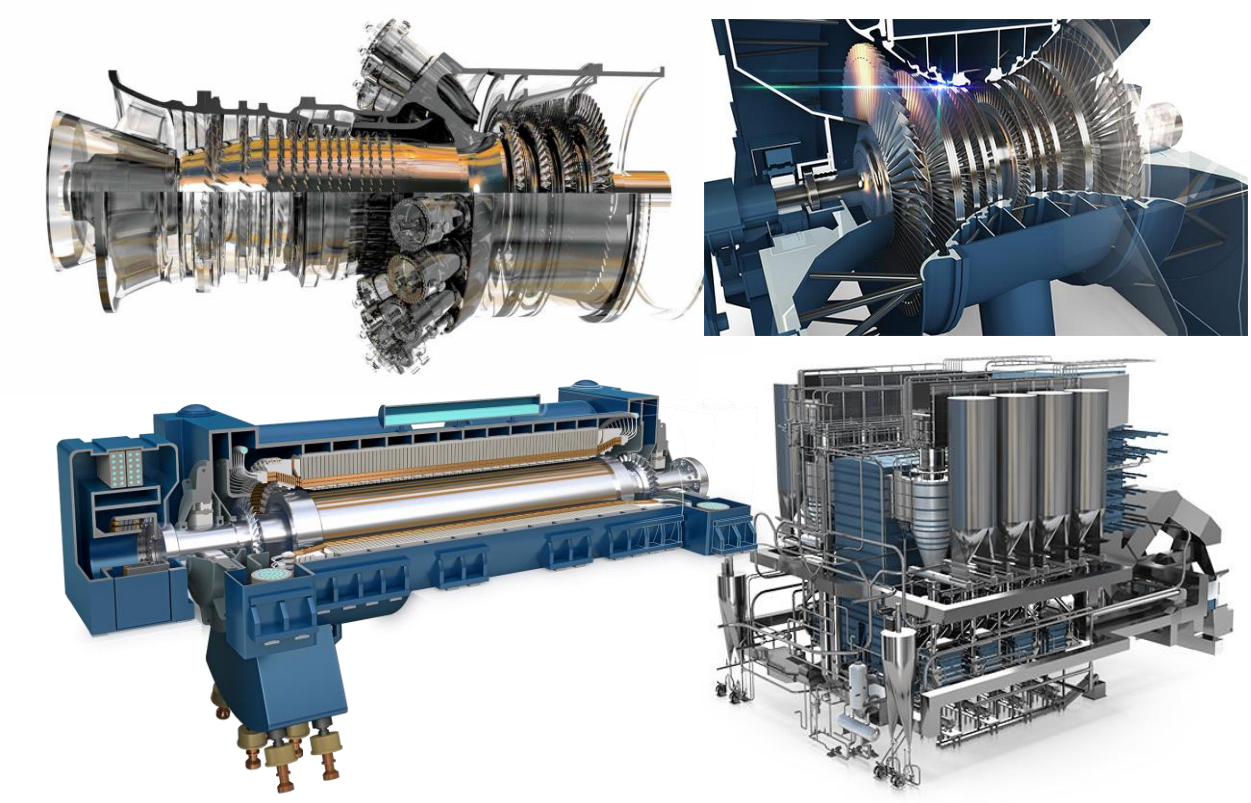

Figure 1.1 - GE components and systems use in high temperature applications; industrial gas turbines, GIGATOP 4-pole generator, and a boiler [8-9].

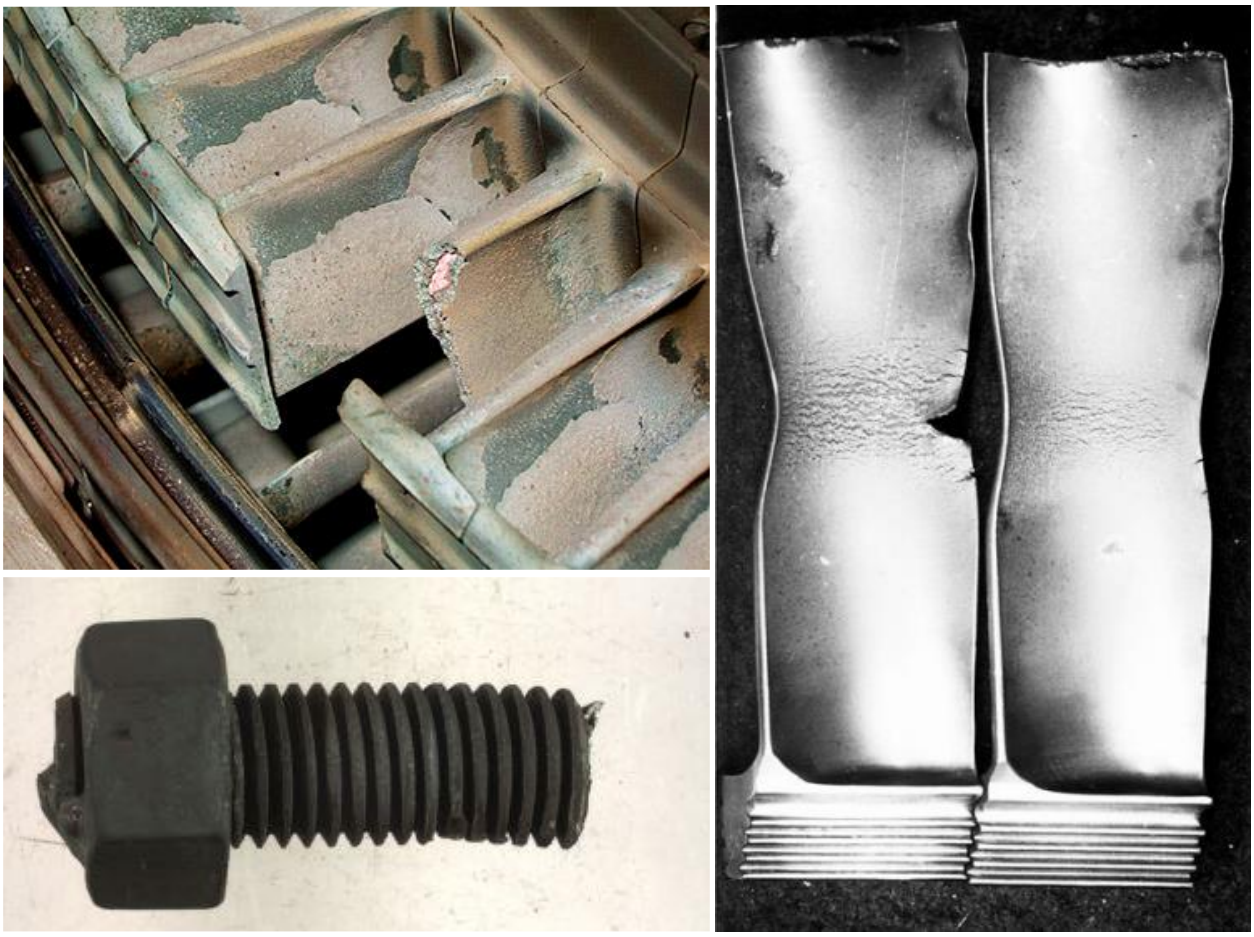

Figure 1.2 - Industrial gas turbine blade creep failure (Berkeley Research Company, Berkeley California), fastener failure of threaded rods, and a turbine blade with large creep deformation [5-7].

Many creep models have emerged to expand the knowledge of long-term creep behaviors $\geq 10^5$ hours) such as rupture time, minimum-creep-strain-rate (MCSR), creep deformation, and damage. There exist limitations when modeling such as the limited data available for long-term creep where experiments can continuously run for 10+ years especially with the requirements from the ASME code [11-12]. The increase in models over the years have work as an alternative to conduction long duration experiments. Numerous constitutive models have been developed to predict creep deformation of materials, such as time-temperature parameter (TTP), however, extrapolations are not as accurate as many models do not adjust for uncertainty, complex

geometries, and stress and temperature dependencies [12-14]. There is a need for a reliable prediction method that has an explicit stress and temperature dependency to extrapolate accurately the creep behaviors of alloys.

### 1.2 Research Objectives

The objective of this study is to show some applications of the recently develop Wilshire-Cano-Stewart (WCS) model to predict rupture time, minimum-creep-strain-rate (MCSR), damage, damage evolution, and creep deformation. The goals of the study are (a) to discuss and determine the framework of the WCS model and validated, (b) applied the model to accelerated creep data to show the capabilities of the model with non-conventional data, and (c) applied a newly numerical method called the datum temperature method (DTM) to show the model capability of using limited data sets to make accurate predictions. To accomplish these goals:

(a) The framework of the WCS model is discuss and validated using P91 data. The model is calibrated using the conventional Wilshire approach to obtain material constants as well as the Sine-Hyperbolic (Sinh) methods. After material constants are obtained, then predictions of rupture time, MCSR, damage, and creep deformations are made.

(b) The WCS model is then applied to accelerated creep data of Inconel-718 obtained from the stepped isostress method (SSM). The model is modified using an energy approach to address the accelerated data and material constants are obtained to make prediction of conventional data.

(c) The WCS model is applied to a numerical approach recently develop name the datum temperature method (DTM). This method allows predictions of limited datasets. The model is calibrated using this method and new DTM equations are develop for MCSR

predictions allowing a fully DTM WCS model. The data is compared with the predictions of the conventional approach with P91 data.

### 1.3 Organization

The organization of this study is as follows: Chapter 2 provides background information on creep deformation, damage, and fatigue. Some constitutive models for MCSR, creep deformation, and fatigue are discussed in a non-exhaustive manner. The Wilshire model, which is the framework use in the WCS model, is introduced, as well as the process in which material constants are calibrated using this method and the work done with the model. Chapter 3 discusses the materials use in other chapters. A brief description of the microstructure and mechanical properties is provided as well as the nominal chemical compositions. Chapter 4 is the introduction of the WCS model already modified from the Wilshire and Sinh models. Predictions for rupture, MCSR, damage, and creep deformation are made to validate the feasibility of the model. Chapter 5 is the WCS model applied to accelerated data with the stepped isostress method (SSM). This chapter modifies the calibration approach to consider the accelerated data and predictions are made with the obtained material constants for conventional data. Chapter 6 introduces a newly develop numerical approach name the datum temperature method (DTM) which transfers conventional data to an accelerated datum (median) temperature to address the limited data use by engineers to predict creep behaviors. The model is then compared to the conventional calibration approach. Chapter 7 concludes the entire studies and proposes future work.

# CHAPTER 2 BACKGROUND

## 2.1 Introduction

To understand the applications of the novel WCS model, a background study is provided in creep phenomena, fatigue, creep-fatigue, and constitutive models. Creep is phenomenological in nature and is divided into regimes. Models exists to predict and understand different behaviors such as rupture time, MCSR, damage history, creep deformation and creep-fatigue. A summary of a few traditional models is provided as well as some limitations of such models. The Wilshire-Cano-Stewart (WCS) model addresses these limitations and issues. The author reserves both the Wilshire model and the Sinh model for later discussion as those are the basis for the WCS model.

## 2.2 Creep Phenomena

Creep is a rate-dependent non-recoverable plastic deformation of materials as a function of stress and temperature [15]. An idealized conventional creep deformation curve is illustrated in Figure 2.1 where stress and temperature are constant, $t_r$ is the rupture time, and the three regimes of creep are shown [15]. Creep strain is activated thermally, and when stress is applied, typically to a metal or ionic solid, deformation leading to failure arises [17]. Most high temperature failures in materials are attribute to creep, fatigue, and combinations of damage [18]. Temperature ranges for creep deformation are: $T > 0.6T_m$ for high temperature, where $T_m$ is the melting temperature, $0.3T_m < T < 0.6T_m$ for intermediate temperatures, and $T < 0.3T_m$ for low temperature [3]. Assuming constant stress, high and intermediate temperatures generate short rupture times and low temperatures might extend to infinite life. There is an interest in such low temperature studies as many models intend to predict decades of life. Mechanical systems such as gas turbines, nuclear reactors, chemical industries, IGTs, aircrafts, and many others operate at these temperature ranges

[18]. Therefore, creep is dependent on high temperatures as well as mixed conditions such as applied stress, geometry, and time.

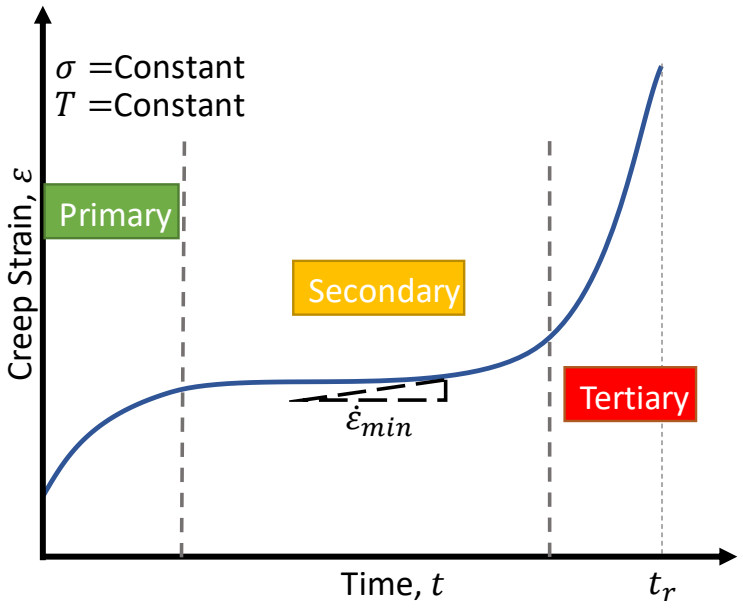


Figure 2.1 – Idealized conventional creep deformation curve [15].

In 1910, Andrade divided the creep deformation curve into three stages or regimes [16]. Those regimes are: the primary regime also called transient creep, the secondary regime called steady-state creep, and the tertiary regime called the accelerating creep, where rupture comes in the tertiary regime as shown in Figure 2.1 [15-21]. Depending on the material the arrangement of these creep regimes might vary. Many materials lack a primary regime or at high stress and temperatures exhibit only a short (transitional) secondary regime. Some brittle materials have little to no tertiary creep while ductile materials would have an extensive tertiary creep regime [17-18].

Some materials have an instantaneous response called $\varepsilon_0$ that depends on the magnitude of the applied stress, this instantaneous response is most of the primary creep regime [15]. Other materials have microstructural mechanism such as precipitate carbides that prevents grain

boundary sliding. Such materials exhibit little primary creep which, in many models, is typically neglected. Primary creep normally reaches its peak in a short time which contributes to the case of neglecting it in modeling. The secondary regime is large and has similar characteristics as plastic deformations [21]. Most mathematical models use this dominant steady-state behavior to approximate the creep curve. Such behavior is called the minimum-creep-strain-rate, $\dot{\varepsilon}_{\min}$ which as shown in Figure 2.1 is almost constant [15]. In the tertiary regime failure happens at a rapid rate and arrives as an unexpected behavior most of the time. Grain boundary sliding contributes to crack propagation and void nucleation and growth which ultimately leads to rupture of a specimen [18].

The dependency of creep from stress and temperature, strongly impacts the creep deformation curves. The influenced in stress where temperature is constant is observed in Figure 2.2 (a). Notice that as stress increases creep ductility is achieved at a faster time. Similarly, the temperature dependency at constant stress portraits a similar behavior as shown in Figure 2.2 (b). It is observed that when the temperature is constant and different stress levels are applied ( $\sigma_3 > \sigma_2 > \sigma_1$) then the rupture time has dramatic impact that can range even for decades of life. Similarly, when stress is constant and distinct isotherms are applied ($T_3 > T_2 > T_1$). Additionally, each individual curve generated has a corresponding $\dot{\varepsilon}_{\min}$ where some creep curves can even transition from the primary to the tertiary regime at high levels of stress and temperature [15,18].

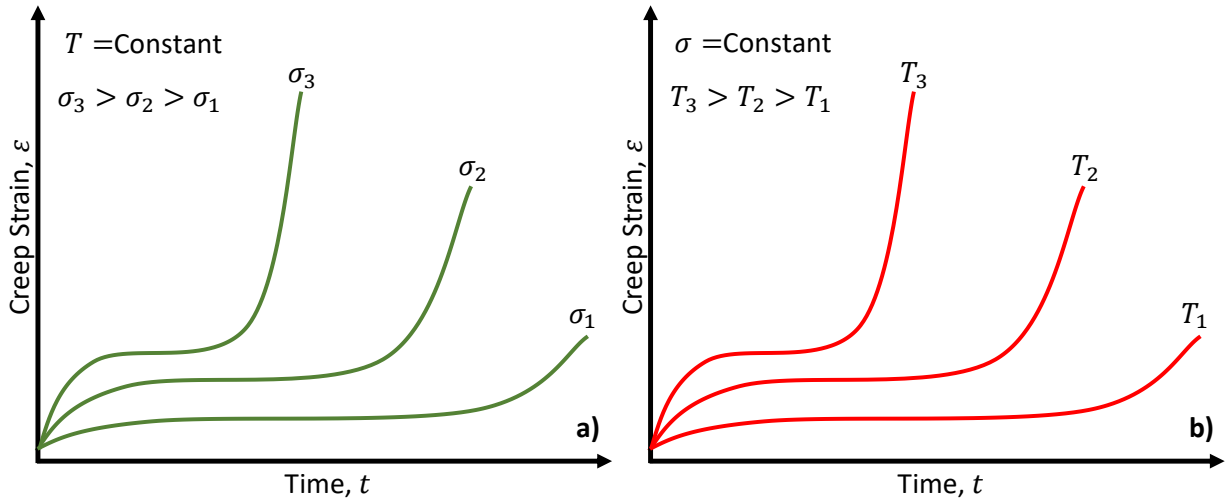


Figure 2.2 – Idealized creep deformation curves as a function of a) stress at constant temperature and b) temperature at constant stress. [15,18].

## 2.3 Creep Testing

A creep test measures, the load carrying ability for limited deformations according to the ASTM standard code E139 [22]. To perform a creep test, and according to ASTM standards E4, the suggested testing machine to perform creep tests is a lever-arm type testing machine [23]. Creep is more predominately under high temperature applications, typically a furnace is attached to the load frame to perform high temperature testing. An example of a commercial creep testing machine is given in the schematic shown in Figure 2.3. Note that the schematic contains a pull rod which is the one that applies the force onto the specimen and the furnace for high temperature testing. Together with the load frame and not included in the schematic, an extensometer is recommended to measure the strain. Perfect axial alignment with the extensometer and the pulls rods, especially when both pass-through packing at the end of a furnace [22]. The grips should be capable of applying force precisely so that a maximum of 10% of the axial strain is not exceed [22]. Isothermal conditions should be reach with limited manual adjustments (automatic temperature control is preferred). The extensometer sensitivity and accuracy are application driven with the capabilities to capture the creep characteristic that are desired [22].

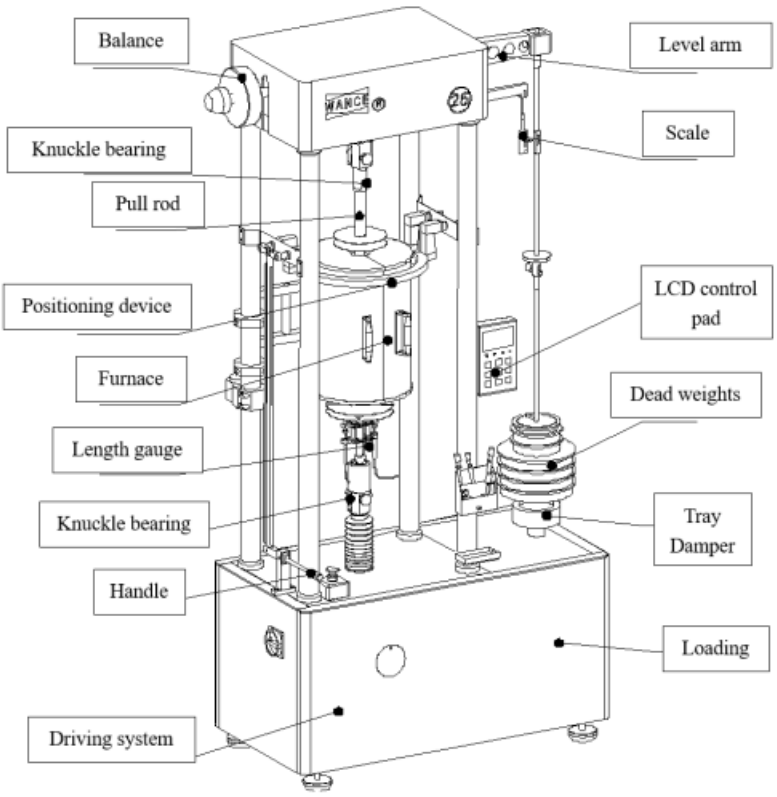


Figure 2.3 – Schematic of a creep testing machine from a commercial company [24].

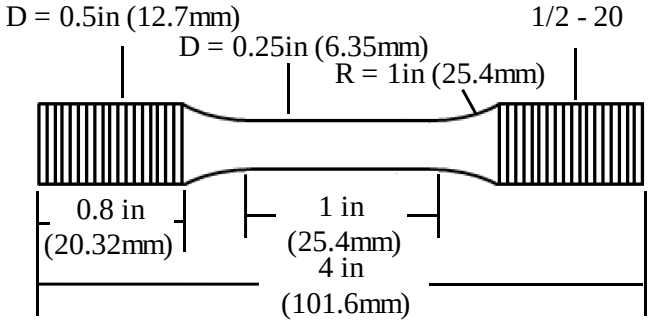


Figure 2.4 – Example of a specimen use for creep testing with a gauge length of 1 inch.

The specimen's size and shape are application driven as well; an example of a specimen use for creep testing is shown in Figure 2.4. Recommendations to apply to the experiment and obtain results according to ASTM code E139 are [22]

- for rolled and extruded specimens, the test orientation is parallel to the direction of fabrication.
- diameter at the ends of the reduce section should not be less than the diameter at the center.
- for measurements obtain the cross-sectional area and the largest diameter in the reduced section.
- measure the original length.

An important consideration when performing testing, is to consider the deformation mechanisms of a material as shown in Figure 2.5 and Figure 2.6.

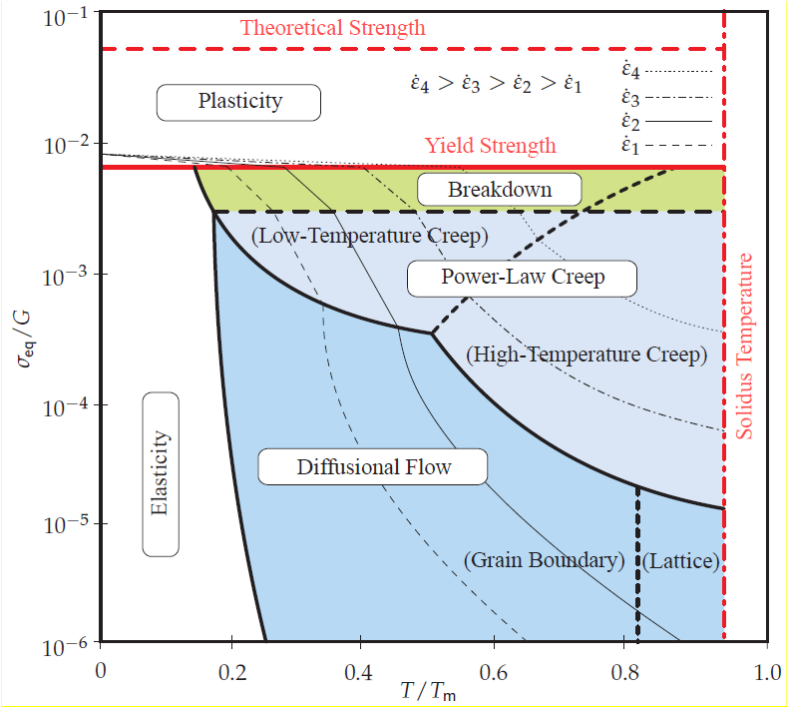


Figure 2.5 – Schematic illustration of a typical deformation mechanism map [19-20].

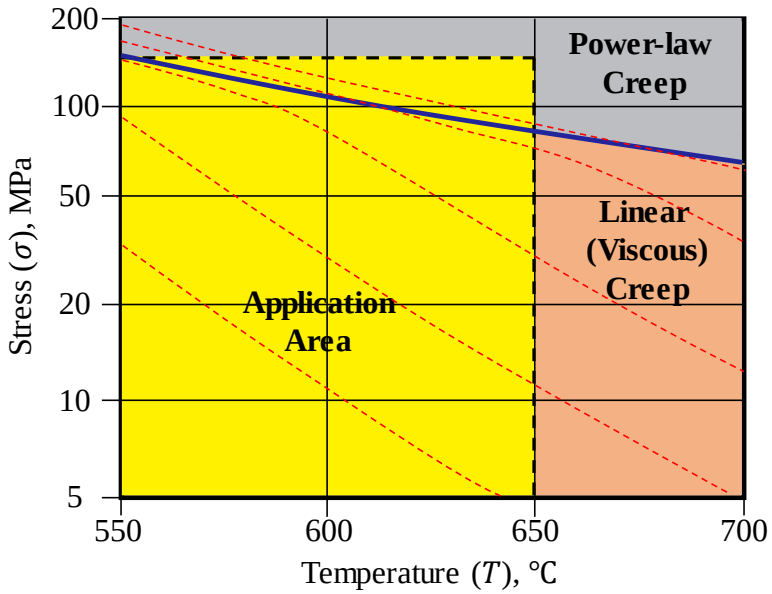


Figure 2.6 – Creep deformation mechanism map 9Cr-1Mo-V-Nb (P91) steel [20].

Creep mechanisms restricts the experiments to a range of temperatures and stresses. According to Frost and Ashby polycrystalline solids yield strength and material properties of materials are define by the processes occurring at the atomic scale [19]. Mechanisms which describe such atomic processes are therefore called deformation mechanisms. There are mainly five groups of deformation mechanisms

- *Collapse at ideal yield strength.* After exceeding a shear strength flow occurs.
- *Low-temperature plasticity by dislocation glide.* Limited by the lattice resistance, discrete obstacles, phonon, drags, and influenced by adiabatic heating.
- *Low-temperature plasticity by twinning.* Dislocation glides involving partial dislocation motions.

- *Power-law creep by dislocation glide.* Limited by glide processes, lattice-diffusion controlled climb, core diffusion-controlled climb, power-law breakdown, Harper-Dorn creep, and creep with dynamic recrystallization.
- *Diffusional flow*. Limited by Nabarro-Herring lattice-diffusion creep or bulk diffusion, coble creep or grain boundary diffusion, and interface-reaction controlled diffusion flow.

If available, during a test, a deformation mechanism should be consulted and especially in some applications.

## 2.4 Wilshire Model

Numerous models for models for creep behaviors have been developed. The Wilshire model has emerged as a well-accepted model due to its explicit stress and temperature dependance that allows predictions of stress-rupture and MCSR at multiple isotherms and stress levels.

Minimum-creep-strain-rate (MCSR) is one of the earliest creep parameters measured as discussed by Norton proposing a power-law to describe it [25]. Many stress-dependence models to describe MCSR have been developed and some of the most common are listed in Table 2.1 [26].

Table 2.1 – Minimum-creep-strain-rate (MCSR) models [25,27-32,53-56].

| Source | MCSR Model |
|---|---|
| Norton, 1929 [25] | $\dot{\varepsilon}_{\min} = A\left(\frac{\sigma}{\sigma_0}\right)^n$ |
| Simplified Norton, 1929 [25] | $\dot{\varepsilon}_{\min} = A\sigma^n$ |
| Nadai, 1931 [27] | $\dot{\varepsilon}_{\min} = A\exp\left(\frac{1}{\sigma_0} + c\sigma\right)$ |
| Soderberg, 1936 [28] | $\dot{\varepsilon}_{\min} = A\left\{\exp\left(\frac{\sigma}{\sigma_0}\right) - 1\right\}$ |
| McVetty, 1943 [29] | $\dot{\varepsilon}_{\min} = A\sinh\left(\frac{\sigma}{\sigma_0}\right)$ |
| Dorn, 1955 [30] | $\dot{\varepsilon}_{\min} = A\exp\left(\frac{\sigma}{\sigma_0}\right)$ |
| Johnson-Henderson-Kahn (JHK), 1936 [31] | $\dot{\varepsilon}_{\min} = A_1\left(\frac{\sigma}{\sigma_0}\right)^{n_1} + A_2\left(\frac{\sigma}{\sigma_0}\right)^{n_2}$ |
| Garofalo, 1965 [32] | $\dot{\varepsilon}_{\min} = A\left\{\sinh\left(\frac{\sigma}{\sigma_0}\right)\right\}^n$ |
| Wilshire, 2007 [53-56]. | $\dot{\varepsilon}_{\min} = \frac{\left[-\ln(\frac{\sigma}{\sigma_{TS}}) \Big/ k_2\right]^{\frac{1}{v}}}{\exp\left(Q_c^* \Big/ RT\right)}$ |

The base theory of the MCSR models comes from three deformation mechanism which are the diffusional-flow, the power-law, and breakdown, illustrated in Figure 2.7. Diffusional flow, also known as the Harper-Dorn creep, is separated in the Nabarro-Herring and coble creep [26].

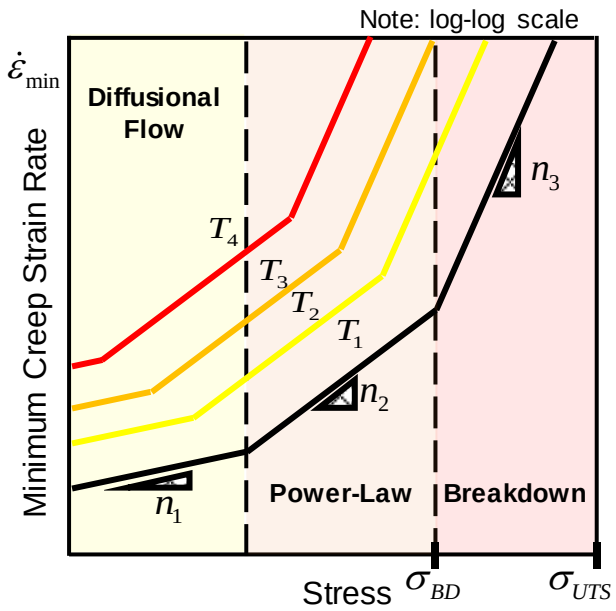


Figure 2.7- Master curve of the minimum-creep-strain-rate based on Norton-power law [26].

Considering the power-law deformation mechanism the Norton-power law form arrives. The Norton-power law is one of most classic models for MCSR and commonly is shown in the following form

$$\dot{\varepsilon}_{\min} = A\left(\frac{\sigma}{\sigma_0}\right)^n \tag{2.1}$$

where $A$ and $n$ are unitless material constant, $\sigma_0$ normalizes stress also known as activation stress and has units of $MPa$. A most simplified form of the Norton-power law is given without the normalized stress shown as

$$\dot{\varepsilon}_{\min} = A\sigma^n \tag{2.2}$$

where now $A$ must be in units of $MPa^{-n}$ [25]. Both material constants $A$ and $n$ exhibit temperature-dependency. This means that the constants obtained at low stress levels are different

from those obtained at high levels as shown in the $n$ constant on Figure 2.7. If the Norton-power law tries to model across multiple isotherms and stress levels, large levels of uncertainty would arrive. The slope for the distinct $n$ from Figure 2.7, is typically 5 but several authors have discovered that it can range between 2 and 12 depending on the creep resistance of materials [33-40].

Soderberg, McVerry and made contributions to addresses temperature dependency and finally Dorn used an Arrhenius function [30]. Dorn suggested that after the material constant $A$ is modified using the Arrhenius approach, the Norton temperature dependent equation takes the following form

$$\dot{\varepsilon}_{\min} = A\left(\frac{\sigma}{\sigma_0}\right)^n \exp\left(\frac{-Q_c}{RT}\right) \tag{2.3}$$

where $Q_c$ is the apparent creep activation energy in $J\ mol^{-1}$, $R$ is the universal gas constant $8.314\ J\ K^{-1}\ mol^{-1}$. It is observed that material constants $Q_c$ and $n$ have stress dependence still.

Although the secondary creep regime is the most dominant, using the MCSR equations does not predict failure. Many rupture models are also developed, and the combination of both the MCSR and the creep rupture equations can be used to recreate a complete creep deformation curve. Typical, CDM models are based on these two conditions.

Creep rupture is a major concern in modeling. There exist time-temperature prediction models, relationships with MCSR, and many others which are summarized in Table 2.2.

Table 2.2 – Creep rupture models [41-42,69,76, 53-56].

| Source | MCSR Model |
|---|---|
| Larson-Miller, 1952 [41] | $LMP = T\left(\log t_r + K_1\right)$, $t_r = 10^{\frac{LMP - T\cdot K_1}{T}}$ |
| Monkman Grant, 1956 [42] | $\log\left(t_r\right) + m\log\left(\dot{\varepsilon}_{\min}\right) = k_{MG}$, $t_r = \frac{10^{k_{MG}}}{\dot{\varepsilon}_{\min}}$ |
| Kachanov-Rabotnov, 1967-69 [69-70] | $t_r = \left[\left(\phi+1\right)M\bar{\sigma}_r^{\chi}\right]^{-1}$ |
| Evan-Wilshire (Theta Projection), 1984 [75] | $\varepsilon_F = \theta_1\left(1-e^{-\theta_2 t_r}\right)+\theta_3\left(e^{\theta_4 t_r}-1\right)$, solve for $t_r$ |
| Omega Method, 1996 [76] | $\frac{t_s}{t_r} = \frac{\dot{\varepsilon} t_s \Omega_p}{\dot{\varepsilon} t_s \Omega_p + 1}$ |
| Wilshire, 2007 [53-56]. | $t_f = \frac{\left[-\ln\left(\frac{\sigma}{\sigma_{TS}}\right)\Big/ k_1\right]^{\frac{1}{u}}}{\exp\left(-\frac{Q_c^*}{RT}\right)}$ |

One of the earliest prediction models is the Larson Miller parameter (LMP) model which is a time-temperature model [41]. The LMP model is defined as follows

$$LMP = T\left(\log t_r + K_1\right) \tag{2.4}$$

where $LMP$ is a function of stress, $T$ is the temperature, $K_1$ is a material constant typically ranging between 10 to 50 [43-45]. Monkman Grant recognized that there exists a relationship between the MCSR and rupture time [42]. Creep fractures appears to be inversely related to the MCSR and is given in the following form

$$\dot{\varepsilon}_{\min} \cdot t_r = M \tag{2.5}$$

where $M$ is just the Monkman Grant constant. Further work from Monkman Grant work leads to the current work from Wilshire.

The Wilshire model comes from some of the classic models describe the Norton-power law for MCSR and the Monkman-Grant law for rupture prediction [25, 46-49]. The Naorton-power law models the MCSR, $\dot{\varepsilon}_{\min}$ as follows

$$\dot{\varepsilon}_{\min} = A\sigma^n \exp\left(-\frac{Q_c}{RT}\right) \tag{2.6}$$

where it takes a similar form as [Eq. (2.3)] but using the simplified Norton. The material parameters $A$, $n$, and $Q_c$ are functions of stress and temperature; suggesting that different creep mechanism become dominant at different stress and temperature regimes. To mitigate this problem, stress can be normalized by the ultimate tensile strength, $\sigma_{TS}$ as follows

$$\dot{\varepsilon}_{\min} = A^*\left(\frac{\sigma}{\sigma_{TS}}\right)^n \exp\left(-\frac{Q_c^*}{RT}\right) \tag{2.7}$$

where the coefficient, $A^*$ and creep activation energy, $Q_c^*$ are stress- and temperature-independent [50-51]. Unfortunately, stress-dependence persists in the $n$ constant due to the nonlinearity observed in normalized stress-rupture data when plotted on a log-log scale. The change in the $n$ constant is associated with distinct creep deformation mechanism such as diffusional flow (Harper-Dorn), power-law, and breakdown as illustrated in Figure 2.7 [50-52].

The Monkman-Grant law arises from the inverse relationship between the minimum-creep-strain-rate, $\dot{\varepsilon}_{\min}$ and rupture time, $t_f$ as shown in [Eq. (2.5)]. Subsequently, rupture time can be predicted by combining the Norton-power and Monkman-Grant laws, [Eq. (2.7)] into [Eq. (2.5)] and rearranging as follows

$$t_f = M\left[A^*(\frac{\sigma}{\sigma_{TS}})^n \exp(-\frac{Q_c^*}{RT})\right]^{-1} \tag{2.8}$$

where $\dot{\varepsilon}_{\min}$ and $t_f$ predictions take the same functional form distinguished by different coefficients and exponents.

Wilshire determined that the Norton-power and Monkman-Grant laws have limitations predicting creep behaviors [53-56]. The stress-dependence of the stress exponent, $n$ persists where $n$ can varied from $n > 5$ at high-stresses to $n \cong 1$ at low-stresses [50-51,57]. Diffusional flow is theorized to exist at low stress $(\sigma < 0.5\sigma_{YS})$; however, literature suggests that diffusion flow does not exist [52]. Rather, diffusion flow is an artefact of the methodology being utilized (i.e., Norton-power law) [57]. Note, this problem persists in the Wilshire model where the material constants may need to be segregated into low-, intermediate-, and high-stress regimes depending on the creep data [51,53]. Based on these observations, Wilshire proposed alternative rupture time, $t_f$ and minimum-creep-strain-rate, $\dot{\varepsilon}_{\min}$ laws as follows

$$\frac{\sigma}{\sigma_{TS}} = \exp\left(-k_1\left[t_f \exp\left(-\frac{Q_c^*}{RT}\right)\right]^u\right) \tag{2.9}$$

$$\frac{\sigma}{\sigma_{TS}} = \exp\left( -k_2 \left[ \dot{\varepsilon}_{\min} \exp\left( \frac{Q_c^*}{RT} \right) \right]^{\nu} \right) \tag{2.10}$$

where $k_1$ (in $hr^{-u}$), $u$, $k_2$ (in $\left(hr^{-1}\right)^{-\nu}$), and $\nu$ are material constants. The $\dot{\varepsilon}_{\min}$ and $t_f$ predictions take the same functional form and are distinguished by different coefficients ($k_1, k_2$) and exponents ($u, \nu$) [50-51,53-56,58]. Note the $\dot{\varepsilon}_{\min}$ prediction lacks a negative sign ahead of $Q_c^*$. An analytical solution to determine the material constants of the Wilshire model is well established.

The six material constants of the Wilshire model ($\sigma_{TS}$, $Q_c^*$, $k_1$, $u$, $k_2$, and $\nu$) can be analytically determined using the approach illustrated in Figure 2.8. Three isotherms of creep data or more are required for calibration. First, monotonic tensile tests shall be performed at each isotherm to gather the ultimate tensile strength, $\sigma_{TS}$. Next, creep tests at fixed stress ratio, $\sigma_i / \sigma_{TS}$ $i = 1,2,3$ shall be performed per isotherm. Creep activation energy, $Q_c^*$ appears in both [Eq. (2.9)] and [Eq. (2.10)] and must be determined first. To obtain $Q_c^*$, take a fixed stress ratio and plot $\ln(\dot{\varepsilon}_{\min})$ or $\ln(t_f)$ versus $1/T$. The fixed stress ratio enables [Eq. (2.9)] and [Eq. (2.10)] to be simplified such that the slope in Figure 2.8 reveals the creep activation energy, [57,59-60]. The remaining constants arise from plotting $\ln[-\ln(\sigma/\sigma_{TS})]$ versus $\ln[t_f \exp(-Q_c^*/RT)]$ and $\ln[-\ln(\sigma/\sigma_{TS})]$ versus $\ln[\dot{\varepsilon}_{\min} \exp(Q_c^*/RT)]$. The stress-rupture constants $k_1$ and $u$ and the MCSR constants $k_2$ and $\nu$ are the y-intercept and slope [53-57]. When properly calibrated, the Wilshire model is one of the best models for predicting the stress-rupture and MCSR over a wide range of temperatures and stress when compared to existing models [57,59].

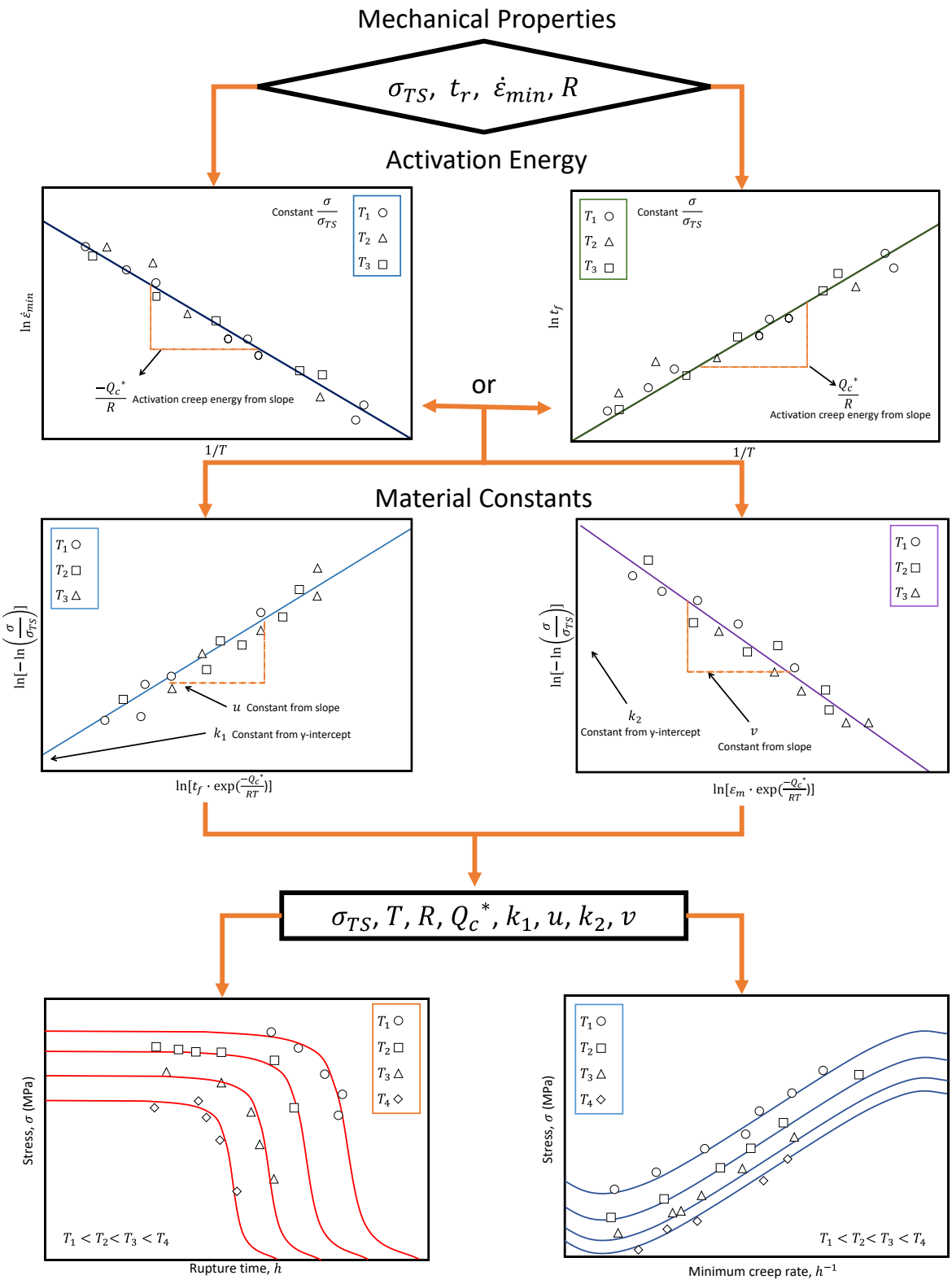


Figure 2.8 - Wilshire material constant determination flow chart.

Generally, the Wilshire model is sensitive to deformation mechanisms. When the dominant deformation mechanism changes, the material constants of the model change. This transition is readily observed as a shift in the slope within calibration plots. Wilshire et al introduced the region-splitting approach where the material constants $Q_c^*$, $k_1$, $u$, $k_2$, and $v$ are split into two sets for low and high stress ratios, $\sigma/\sigma_{TS}$ respectively [53-56]. Wilshire et al found that if region-splitting is not considered, the model when calibrated to short-term (high-stress ratio) data, over predictions the stress-rupture and under predictions for MCSR of long-term data. Initially, Wilshire identified the yield strength ratio, $\sigma_{YS}/\sigma_{TS}$ as the split point where material constants change [53-56]. In this Chapter, a more detailed approach is applied where the deformation mechanism maps are consulted to define the split regions. Region splits are defined at the field boundaries in a deformation mechanism map (bold lines) which indicate where two or more mechanisms have equal flow rates. Thus, region splits match the physical deformation processes within the material as a function of stress and temperature.

Gray and Whittaker, found two different methods for region splitting: one where the activation energy, $Q_c^*$ also splits, another where $Q_c^*$ does not split [61]. The former is more accurate to the physical processes (where activation energy changes with deformation mechanism), while the latter is easier to implement. Cedro et al studied both methods on alloys HR6W and Sanicro 25 and found that splitting $Q_c^*$ has a minor but positive effect on the goodness of fit of the Wilshire equations to the experimental data [63]. The magnitude of the $Q_c^*$ splitting effect greatly depends on the quantity and range of experimental data. In this Chapter, $Q_c^*$ is not split due to the limited experimental data under study.

The Wilshire equations have been applied to a variety of alloys including polycrystalline copper, 9-12% chromium steels (Grade 122, 11Cr-2W, and 12Cr stainless steel bars), 1Cr-1Mo-0.25V, 316H stainless steel, among others [53-56, 64-66]. Wilshire and others demonstrated that the model, calibrated to short-term data (30,000 hrs or less), can accurately extrapolate the 100,000 hr strength of materials across multiple isotherms [53-57]. Reasonable estimates of 100,000 hr strength can also be made with as little as 5,000 hrs of creep data. Differences in chemistry, thermomechanical processing, product form, and finish make a considerable impact on the material constants and predictions of the Wilshire model. Recently, Evans introduced a more generalized model that can regress into either the Wilshire or Yang models depending on the state of an additional material constant [67].

Wilshire introduced a third equation for predicting the time-to-creep-strain, $t_{\varepsilon_{cr}}$ as follows

$$\frac{\sigma}{\sigma_{TS}} = \exp\left( -k_3 \left[ t_{\varepsilon_{cr}} \exp\left( -\frac{Q_c^*}{RT} \right) \right]^w \right) \tag{2.11}$$

where $k_3$ and $w$ are material constants calibrated at a specific creep strain, $\varepsilon_{cr}$ value [55-56,59].

The time-to-creep-strain [Eq. (2.11)] can be employed to predict creep strain. The process is complicated. Creep deformation curves are converted into a tabular form where the stress, temperature, and time-to-creep-strain ($\sigma, T, t_{\varepsilon_{cr}}$) are reported with respect to specific values of creep strain, $\varepsilon_{cr}$ (e.g. 0.01%, 0.1%, 1%, etc. to creep ductility). For each specific value of creep strain, $\varepsilon_{cr}$, an independent set of $k_3$ and $w$ constants must be determined. The $k_3$ and $w$ material constants are obtained by plotting the experimental data $\ln\left[ -\ln\left( \sigma/\sigma_{TS} \right) \right]$ versus $\ln\left[ t_{\varepsilon_{cr}} \exp\left( -Q_c^*/RT \right) \right]$ where the slope is $w$ and the y-intercept is the $k_3$ constant. Regression

analysis is applied to convert $k_3$ and $w$ into functions of creep strain $k_3(\varepsilon_{cr})$ and $w(\varepsilon_{cr})$. Adding the $k_3(\varepsilon_{cr})$ and $w(\varepsilon_{cr})$ functions to [Eq. (2.11)] and rearranging to solve for $\varepsilon_{cr}$, furnishes a creep strain prediction. A closed-form creep strain equation may or may not exist dependent on the functional form of $k_3(\varepsilon_{cr})$ and $w(\varepsilon_{cr})$ respectively. If a closed-form creep strain equation does not exist, then the creep strain increment does not exist and must be determined numerically followed by (or simultaneous to) the radial-return method for the update stress. In FEA, this procedure is required at every integration point and global iteration resulting in the Wilshire model being computationally expensive. Thus far, the Wilshire creep strain has not been implemented in FEA and is used exclusively for analytical problems [55,59]. In addition, damage is not tracked; therefore, the Wilshire model is not appropriate for dynamic loading conditions (service loading, stress redistribution, confined creep, notched creep, etc.) where load history influences the constitutive response and rupture. Continuum-damage-mechanics is employed to resolves these limitations.

## 2.5 Continuum Damage Mechanics

Previous sections model the MCSR, and the rupture of materials subjected to a loading, but it is known that materials have a history of damage that causes the loss of mechanical properties, strength, and creep resistance [68]. The creep deformation and the damage history of the materials are typically not models describe in Table 2.1 and Table 2.2. Therefore, creep deformation constitutive models and continuum damage mechanics (CDM) models are needed to predict the creep strain of materials.

Continuum damage mechanics (CDM) allows the description of materials with a continuous deterioration, also known as, damage. Damage is measure from its initial state, which

constitutes to no damage, to the final stage which generally corresponds to macro-cracking, failure of the material, or the end of life [71]. First introduced by Kachanov and Rabotnov, CDM was used to predict the tertiary creep regime and the change of creep ductility using effective stress [69-71]. The advantage of using CDM model is that it allows the description of heterogenous microprocesses that exist because of the straining of materials. Elastic and plastic strains and the strain hardening effects of materials are accepted and included in the global description of continuum variables although they involve homogenous effects such as microdefects, grains, sub grains, and dislocations [77-78]. This description allows predictions of lifetime properties such as rupture strength, fatigue life, and creep rupture life [71]. Material defects can be classified with respect to their geometry; point defects which are vacancies and impurity atoms, line defects known as dislocations, plane defects which are slip planes and cracks, and volume defects which are cavities and inclusions in the materials [71]. These defect are measure to a corresponding micromechanical or phenomenological response which are the (1) measurements at the microstructural scale, (2) measurements at the macro physical scale and effective stress (3) measurements of remaining life, and (4) measurements of variations in the macro mechanical behavior [71-80].

Chaboche describes the first three processes starting with the (1) measure at the microstructural scale which is the observation of irreversible effects such as intergranular cavities in creep, surface microcracks in fatigue, and the dimension of cavities in ductile fracture [78]. The disadvantage of this measure is that is destructive, the phase of no damage is difficult to observed, and the quantification is done through macroscopic variables [77-80]. The following equation defines it in terms of area reduction

$$D_n = \frac{S_D}{S} = \frac{S - S^*}{S} \tag{2.12}$$

where $D_n$ is the damage variable with a $n$ direction, and $S$ is the entropy of the material. Microstructural changes are best measure through the nucleation and growth of cavities on the grain boundaries. The area reduction theory is used assuming the distribution of such cavities and a symmetric tensor is developed

$$\Omega = \frac{3}{S_g(V)} \sum_{k=1}^{N} \int_V \vec{v}^{(k)} \otimes \vec{v}^{(k)} dS_d{}^{(k)} \tag{2.13}$$

where $dS_d{}^{(k)}$ is the area of a given boundary with a k$^{th}$ cavity in a volume and $\vec{v}^{(k)}$ is the unit of the normal vector. Note that this definition considers the direction which naturally impact the damage and more approaches are necessary for anisotropic materials [77-78].

The (2) measure through physical parameters and effective stress impacts the physical properties of materials which allows it to be measurable. An example is in density changes where the damage can be understood as the ductile failure of a material [71-80]. Theory of effective stress has been developed where damage results in the loss of effective area written as

$$\bar{\sigma} = \sigma \frac{S}{\bar{S}} = \frac{\sigma}{1 - D} \tag{2.14}$$

which is defined by Chaboche and Duvaut [78,81]. Expanding on this theory Lemaitre measures the ductile rupture using the modulus of elasticity define as

$$\bar{\sigma} = \sigma \frac{E}{\bar{E}} = \frac{\sigma}{1 - D} \rightarrow D = 1 - \frac{\bar{E}}{E} \tag{2.15}$$

for both undamaged and damage materials [16,78]. Brittle creep is then study and define using strain rate measurements of the tertiary creep and the effective stress shown as

$$D = 1 - \left( \frac{\dot{\varepsilon}}{\dot{\varepsilon}_s} \right)^{1/N} \tag{2.16}$$

where $\dot{\varepsilon}_s$ is the secondary creep and $N$ is a exponent using the power law and obtain from multiple tests [16,78-79].

The (3) damage measure of the remaining life is one of the most natural ways of describing damage, as from an engineering and design point, the end of life is one of the objectives to developed damage theory [71-78]. Damage is easily obtained through the life ratio later implemented in the following form

$$\frac{N_2}{N_{F2}} = 1 - D = 1 - \frac{N_1}{N_{F1}} \tag{2.17}$$

where $N_2$ is the remaining life at the second level after damage from $N_1/N_{F1}$, and $N_{F2}$ is the nominal life [71-80].

Damage is accumulated in materials and some of the best models to describe creep deformation are based on CDM. A summary of the CDM mechanics models as well as additional constitutive equations are provided in Table 2.3 with the regime that they typically model [69-76,82].

Table 2.3 – Summary of creep constitutive equations [72,69-76,82].

| Source | Creep Law | Regimes |
|---|---|---|
| Kachanov-Rabotnov, 1967-69 [69-70] | $\dot{\varepsilon}_{cr} = A\left( \frac{\sigma}{1-\omega} \right)^n,\ \dot{\omega} = \frac{M\sigma^{\chi}}{(1-\omega)^{\phi}}$ | Secondary Tertiary |
| Evans-Wilshire (Theta Projection), 1984 [75] | $\varepsilon = \theta_1\left(1 - e^{-\theta_2 t}\right) + \theta_3\left(e^{\theta_4 t} - 1\right)$ | Primary Secondary Tertiary |

| | | |
|---|---|---|
| Prager, M. (MPC Omega), 1995 [76] | $\dot{\varepsilon}_{cr} = \dot{\varepsilon}_0 \exp\left(\Omega_p \varepsilon\right)$ | Secondary Tertiary |
| Liu and Murakami, 1998 [82]. | $\dot{\varepsilon}_{cr} = \frac{3}{2} A \sigma_{eq}{}^{n} \frac{S_{ij}}{\sigma_{eq}} \exp\left(\frac{2(n+1)}{\pi\sqrt{1+3/n}} \cdot \frac{\sigma_1}{\sigma_{eq}} \cdot \omega^{3/2}\right)$ <br> $\dot{\omega} = B \frac{\left(1-\exp(-q_2)\right)}{q_2} \sigma_r{}^{\chi} \exp(q_2 \omega)$ | Secondary Tertiary |
| Sinh Model 2013, [72] | $\dot{\varepsilon}_{cr} = A \sinh\left(\sigma/\sigma_s\right) \exp\left(\lambda \omega^{3/2}\right)$ <br> $\dot{\omega} = \frac{M\left[1-\exp(-\phi)\right]}{\phi} \sinh\left(\frac{\sigma}{\sigma_t}\right)^{\chi} \exp(\phi\omega)$ | Secondary Tertiary |

The Kachanov-Rabotnov model came as a contribution between the work of Kachanov introducing phenomenological CDM for damage modeling and Rabotnov incorporated damage into the creep strain rate equation [69-70]. The Kachanov-Rabotnov model for creep strain and damage rate are as follow

$$\dot{\varepsilon}_{cr} = \frac{d\varepsilon_{cr}}{dt} = A\left(\frac{\sigma}{1-\omega}\right)^{n} \tag{2.18}$$

$$\dot{\omega} = \frac{d\omega}{dt} = \frac{M\sigma^{\chi}}{(1-\omega)^{\phi}} \tag{2.19}$$

where $A$ and $n$ are the Norton-power law constants, $\sigma$ is equivalent stress, $M$, $\chi$, $\phi$ are material constants that model the tertiary creep regime. The Kachanov-Rabotnov model has predicted accurately creep deformation, however, is limited on its fundamental forms [68-76,82-85]. Kachanov-Rabotnov is considered a local CDM approach which means rupture is achieve when damage variable is unity, however, rupture occurs below unity. The Kachanov-Rabotnov

model has stress sensitivity which means that damage rate becomes unrealistically huge near rupture time [68].

The theta-projection model proposed by Evans and Wilshire is a multistage model that connects the primary and tertiary regimes using the material constants [75]. The classic theta-projection model is shown as follows

$$\varepsilon = \theta_1\left(1-e^{-\theta_2 t}\right)+\theta_3\left(e^{\theta_4 t}-1\right) \tag{2.20}$$

where the theta-constants $\theta_1$ and $\theta_2$ generate the primary creep regime and $\theta_3, \theta_4$ control the tertiary regime. The theta constants are functions of stress and temperature that are numerical in nature. A limitation the theta-projection model shows is that a single set of theta values are not always accurate when predicting multiple isotherms and stress levels. There is especially a problem with $\theta_4$ as for long rupture life predictions creep strain becomes very large and if $\theta_4$ is set low underpredictions arrive at an early stage of the creep deformation curve [85].

The MPC Omega model was first introduced by Prager in 1995 [76]. The damage model of the MPC Omega is given as

$$\omega = \frac{t}{t_r} = \frac{\dot{\varepsilon}\Omega_p t}{1+\dot{\varepsilon}\Omega_p t} \tag{2.21}$$

where $t$ is the current time, $t_r$ is the rupture time, and $\Omega_p$ is a material constant susceptible to creep [85]. Material constant $\Omega_p$ is obtained through experimental data and by taking the natural logarithm, rearranging, and simplifying [Eq. (2.21)] the following creep strain form is obtained

$$\dot{\varepsilon}_{cr} = \dot{\varepsilon}_0 \exp\left(\Omega_p \varepsilon\right) \tag{2.22}$$

where $\varepsilon$ is the current creep strain and the logarithm of both sides is as follows

$$\ln\left(\dot{\varepsilon}_{cr}\right) = \ln\left(\dot{\varepsilon}_0\right) + \varepsilon\Omega_p \tag{2.23}$$

where $\Omega_p$ is determined from the slope of $\ln\left(\dot{\varepsilon}_{cr}\right)$ versus $\varepsilon$. If the plot between $\ln\left(\dot{\varepsilon}_{cr}\right)$ and $\varepsilon$ determines if the plot does not have a straight line in which at this moment it is not recommended to use the MPC Omega model [85].

As a modification of the Kachanov-Rabotnov model Liu and Murakami creep damage model is obtained [82]. Liu and Murakami model creep and damage models are in the following form

$$\dot{\varepsilon}_{eq} = \frac{3}{2} A \sigma_{eq}{}^{n} \frac{S_{ij}}{\sigma_{eq}} \exp\left( \frac{2\left(n+1\right)}{\pi\sqrt{1+3/n}} \cdot \frac{\sigma_1}{\sigma_{eq}} \cdot \omega^{3/2} \right) \tag{2.24}$$

$$\dot{\omega} = B \frac{\left(1-\exp\left(-q_2\right)\right)}{q_2} \sigma_r{}^{\chi} \exp\left(q_2 \omega\right) \tag{2.25}$$

where $A$, $n$, $B$, $q_2$, and $\chi$ are material constants, $\sigma_r$ is the rupture stress, $\dot{\varepsilon}_{eq}$ and $\sigma_{eq}$ are the equivalent strain and stress respectively, $S_{ij}$ is the deviatoric stress and $\omega$ is damage. In this case, when $\omega$ reaches a critical value, typically 0.99, failure is assumed to occurred [83]. Note that through this work the Sinh model is developed which is discussed later.

Recent models have been developed which are not listed such as some TTP models and power-law variations. Further, the Wilshire model and the Sine-Hyperbolic (Sinh) models are

discussed and integrated into the WCS model to obtain predictions of rupture, MCSR, damage, damage rate, and creep deformation.

### 2.6 Sinh Model

The sin-hyperbolic (Sinh) model is a continuum damage mechanics (CDM)-based model for creep deformation, damage, and rupture prediction [2,12-13,72,68,85]. Creep-strain-rate takes the form

$$\dot{\varepsilon}_{cr} = A\sinh\left(\frac{\sigma}{\sigma_s}\right)\exp\left(\lambda\omega^{3/2}\right) \tag{2.26}$$

where $A$ and $\sigma_s$ are the minimum-creep-strain-rate (MCSR) constants and $\omega$ is damage ranging from $0 < \omega < 1$. The constant $\lambda$ is defined as

$$\lambda = \ln\left(\dot{\varepsilon}_{final}/\dot{\varepsilon}_{\min}\right) \tag{2.27}$$

where the MCSR, $\dot{\varepsilon}_{\min}$ and final-creep-strain-rate, $\dot{\varepsilon}_{final}$ are measured from experimental data and $\lambda > 0$. When damage is zero, the MCSR predictions arises in [Eq. (2.26)] as follows

$$\dot{\varepsilon}_{\min} = A\sinh\left(\frac{\sigma}{\sigma_s}\right) \tag{2.28}$$

where regression analysis of MCSR data furnishes the $A$ and $\sigma_s$ material constants. Damage evolution takes the form

$$\dot{\omega} = \frac{\left[1-\exp(-\phi)\right]}{\phi} M\sinh\left(\frac{\sigma}{\sigma_t}\right)^{\chi}\exp\left(\phi\omega\right) \tag{2.29}$$

where $M$ , $\chi$ , $\sigma_t$, and $\phi$ are material constants and $\omega$ is damage. The damage-trajectory constant $\phi$ is defined as

$$\phi = \ln\left(\dot{\omega}_{final} / \dot{\omega}_{ini}\right) \tag{2.30}$$

where the initial-damage-rate, $\dot{\omega}_{ini}$ and final-damage-rate, $\dot{\omega}_{final}$ are not experimentally measured but can be analytical calculated and $\phi \geq 1$. Analytical damage, $\omega^*$ and damage rates, $\dot{\omega}^*$ data can be calculated from creep deformation data by rearranging [Eq. (2.26)] as follows

$$\omega^* = \left[\frac{1}{\lambda}\ln\left(\frac{\dot{\varepsilon}_{cr}}{\dot{\varepsilon}_{\min}}\right)\right]^{2/3} \tag{2.31}$$
$$\dot{\omega}^* = \frac{\Delta\omega^*}{\Delta t}$$

from which the material constant $\phi$ can be calibrated using [Eq. (2.30)].

Finite integration of damage evolution [Eq. (2.29)] from $0 < t < t_f$ and $0 < \omega < 1$, furnishes rupture prediction as

$$t_f = \left[M \sinh\left(\frac{\sigma}{\sigma_t}\right)^{\chi}\right]^{-1} \tag{2.32}$$

where regression analysis of stress-rupture (SR) data furnishes the $M$ , $\chi$ and $\sigma_t$ material constants.

Indefinite integration of damage evolution [Eq. (2.29)] furnishes damage as

$$\omega(t) = -\frac{1}{\phi}\ln\left[1-\left[1-\exp(-\phi)\right]\frac{t}{t_f}\right] \tag{2.33}$$

where again $\phi \geq 1$.

A deficient of the Sinh model is that temperature-dependence is not explicitly stated. Typical of CDM models, temperature-dependence is added using Arrhenius functions after calibration resulting in high-quality individual predictions at the expense of interpolation and extrapolation ability [2,12-13,72,68,85]. Ongoing studies show the $\lambda$ and $\phi$ constants exhibit a co-dependence with stress and temperature [86]. It is hypothesized that replacing the stress-dependent sine-hyperbolic functions [Eq. (2.28),(2.32)] in the Sinh model with the stress- and temperature-dependent functions in Wilshire [Eq. (4.1),(4.2)] will improve interpolation and extrapolation ability.

The Sinh model has been shown to accurately predict the creep deformation, damage, and rupture of several alloys including: 304SS, 316SS, Waspaloy, Hastelloy X, among others [2,12-13,72,68,85]. The Sinh model exhibits less stress-sensitive, less mesh-dependent, and better convergence when compared to other classic CDM models [2,12-13,72,68,85]. In the Sinh model, critical damage is always equal unity, $\omega = 1$ irrespective to loading conditions (uniaxial or multiaxial). The model has been implemented in commercial FEA software to simulate multiaxial creep including notches and cracks [2,12-13,72,68,85]. A method for calibrating the Sinh model using data from disparate sources has been developed [12]. A probabilistic modeling framework has been developed for the Sinh model, where probability distribution functions and Monte Carlo simulations are employed to replicate the uncertainty in creep experiments including the effect of pre-existing defects, boundary condition fluctuations, and material uncertainty [86].

## 2.7 Summary of Research Questions

The objective of the study is to show applications of a novel model, the Wilshire-Cano-Stewart (WCS) model. There are multiple questions that remain after discussing both the Wilshire and Sinh models. The following questions summarize some of the goals of this study

- How can the Wilshire model be combining with the CDM Sinh model to predict stress-rupture, MCSR, damage, and creep deformation?
- How is the new model calibrated? Does it change or does it follow a similar approach?
- How are the capabilities of both models preserve?
- What impact does the WCS model have on accelerated testing methods?
- How can the model be used combined with numerical methods such as the datum temperature method and what is the benefits?

These questions are pivotal for the upcoming chapters and address the research objectives and the goals of the study.

# CHAPTER 3 MATERIALS

## 3.1 P91

Material used in Chapter 4 and Chapter 6 is 9Cr-1Mo-V-Nb steel better known as P91 alloy. Some applications for P91 are pipelining, boiling components, and steam generators due to the high resistance to stress corrosion and oxidation [87-88]. Alloy P91 is a ferritic-martensitic steel due to the 9 wt% Cr and with the addition of Nb and V creep strength increases [89]. The microstructure of a P91 tube is obtained from the National Institute of Materials Science (NIMS) database and is illustrated in Figure 3.1, where the material has been heat treated to reference code MGC. Precipitate carbides, which most typically are $M_{23}C_6$, are located at the grain boundaries [90-91]. There are carbonitrides finely distributed within the ferritic-martensitic matrix as well. The microalloying elements Nb, V, and Mo are the ones that formed these fine and stable carbides and carbonitrides. These prevents dislocation within the grain boundaries and retains finer grains during austenization delaying plastic deformation due to grain boundary sliding.

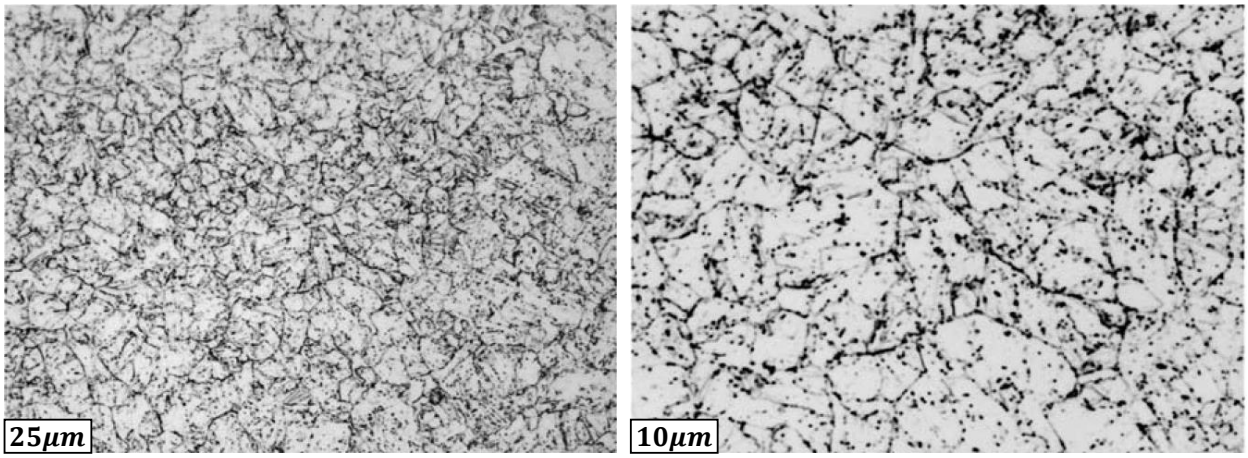


Figure 3.1 – Microstructure of 9Cr-1Mo-V-Nb (P91) steels tube MGC at center of wall thickness [91].

The NIMS nominal chemical composition in mass percent of alloy P91 is reported in Table 3.1 for the different material forms (tube, plate, and pipe) [91].

Table 3.1- Nominal chemical composition (mass percent) of tube, plate, and pipe for 9Cr-1Mo-V-Nb (P91) [91].

| Element | Tube | Plate | Pipe |
|---|---|---|---|
| Fe | Bal. | Bal. | Bal. |
| C | 0.07-0.14 | 0.06-0.15 | 0.08-0.12 |
| Si | 0.20-0.50 | 0.18-0.56 | 0.20-0.50 |
| Mn | 0.30-0.60 | 0.25-0.66 | 0.30-0.60 |
| P | ≤0.020 | ≤0.025 | ≤0.020 |
| S | ≤0.010 | ≤0.012 | ≤0.010 |
| Ni | ≤0.40 | ≤0.43 | ≤0.40 |
| Cr | 8.00-9.50 | 7.90-9.60 | 8.00-9.50 |
| Mo | 0.85-1.05 | 0.80-1.10 | 0.85-1.05 |
| V | 0.18-0.25 | 0.16-0.27 | 0.18-0.25 |
| Nb* | 0.06-0.10 | 0.05-0.11 | 0.06-0.10 |
| N | 0.30-0.070 | 0.025-0.080 | 0.030-0.070 |
| Al* | ≤0.04 | ≤0.05 | ≤0.04 |
| | ≤0.02 | ≤0.02 | ≤0.02 |
| Ti* | - | - | - |
| | ≤0.01 | ≤0.01 | ≤0.01 |
| Zr* | - | - | - |
| | ≤0.01 | ≤0.01 | ≤0.01 |

The heat treatments for each material form for alloy P91 is presented in Table 3.2 which is taken from the NIMS database [91]. Heat treatments are denoted as; MGA, MGB, MGC, MGD, MGF, and MGD for tube, MgA, MgB, MgC, MgD for plate, and MGQ for pipe. Each batch of material is reported alongside with its type of melting, process, thermal history, and the Rockwell hardness (HRC). The types of melting are basic electric arc (BEA) furnace, LD converter (LDC), and top and bottom blown converter (TBBC). The processing is either hot extruded and cold drawn, how extruded, and hot rolled with air cooling (AC) or furnace cooling (FC).

Table 3.2- Details of heat treatment for alloy 9Cr-1Mo-V-Nb (P91) in tube, plate, and pipe form [91].

| Tube | | | |
|---|---|---|---|
| Heat Treatment | Type of Melting | Processing and thermal history | Rockwell hardness (HRC) |
| MGA | BEA | Hot extruded and cold drawn<br>1045 °C /10 min AC<br>780 °C /60 min AC | 16 |
| MGB | BEA | Hot extruded and cold drawn<br>1050 °C /60 min AC<br>760 °C /60 min AC | 16 |
| MGC | BEA | Hot extruded and cold drawn<br>1050 °C /10 min AC<br>765 °C /30 min AC | 18 |
| MGD | LDC | Hot extruded and cold drawn<br>1050 °C /10 min AC<br>780 °C /40 min AC | 18 |
| MGF | BEA | Hot extruded<br>1045 °C /60 min AC<br>780 °C /60 min AC | 18 |
| MGG | TBBC | Hot rolled<br>1050 °C /15 min AC<br>790 °C /60 min AC | 18 |

| Plate | | | |
|---|---|---|---|
| Heat Treatment | Type of Melting | Processing and thermal history | Rockwell hardness (HRC) |
| MgA | BEA | Hot rolled<br>1050 °C /10 min AC<br>770 °C /60 min AC<br>740 °C /8.4 h FC | 13 |
| MgB | BEA | Hot rolled<br>1050 °C /10 min AC<br>770 °C /60 min AC<br>740 °C /60 min FC | 14 |
| MgC | LDC | Hot rolled<br>1060 °C /90 min AC<br>760 °C /60 min AC | 17 |

| | | | |
|---|---|---|---|
| | | 730 °C /8.4 h FC | |
| MgD | LDC | Hot rolled<br>1050 °C /30 min AC<br>780 °C /30 min AC | 16 |

Pipe

| Heat Treatment | Type of Melting | Processing and thermal history | Rockwell hardness (HRC) |
|---|---|---|---|
| MGQ | BEA | Hot rolled<br>1060 °C /60 min AC<br>780 °C /60 min AC | 15 |

Considering each material form and knowing that each heat treatment produces different properties the tensile strengths, $\sigma_{TS}$ is given in Table 3.3. The average tensile strength for each form is given across the different heat treatments.

Table 3.3- Average tensile strength for alloy P91 for tube, plate and pipe interpolating and using the NIMS database [91]

| | Average Tensile Strength, $\sigma_{TS}$ | | |
|---|---|---|---|
| Temperature (°C) | Tube (MPa) | Plate (MPa) | Pipe (MPa) |
| 100 | 658.33 | 635.75 | 621 |
| 200 | 620.83 | 589.25 | 583 |
| 300 | 592.50 | 561.00 | 554 |
| 400 | 568.67 | 492.25 | 533 |
| 450 | 527.67 | 516.75 | 512 |
| 500 | 486.67 | 469.75 | 464 |
| 550 | 418.00 | 414.00 | 402 |
| 575 | 382.09* | 375.5* | 367.5* |
| 600 | 346.17 | 337.00 | 333 |
| 625 | 309.09* | 306.13* | 299.5* |
| 650 | 272.00 | 275.25 | 266 |
| 675 | 237.25* | 240.25* | 483 |
| 700 | 202.50 | 205.25 | 200 |

*tensile strengths that are interpolated

In total, 200 stress-rupture and 350 MCSR experimental data points are available which are gathered and illustrated in Figure 3.2. Both stress-rupture and MCSR data are presented with respect to the isotherm. The heat treatment and the material forms are not considered in Figure 3.2. Each material form has data for calibration and for further post-audit validation. The available data is presented in Table 3.4.

Table 3.4– Available datapoints for stress-rupture and MCSR obtained from NIMS [91]

| | Tube | Plate | Pipe |
|---|---|---|---|
| Stress-Rupture Available Data | 80 | 80 | 40 |
| Stress-Rupture Isotherms (°C) | 500, 550, 600, 650, and 700 | 450, 500, 550, 600, and 650 | 450, 500, 550, 600, and 650 |
| MCSR Available Data | 180 | 130 | 30 |
| MCSR Isotherms (°C) | 500, 550, 575, 600, 625, 650, 675 and 700 | 450, 500, 550, 575, 600, 625, 650, and 700 | 500, 550, 575, 600, 625, 650, and 700 |

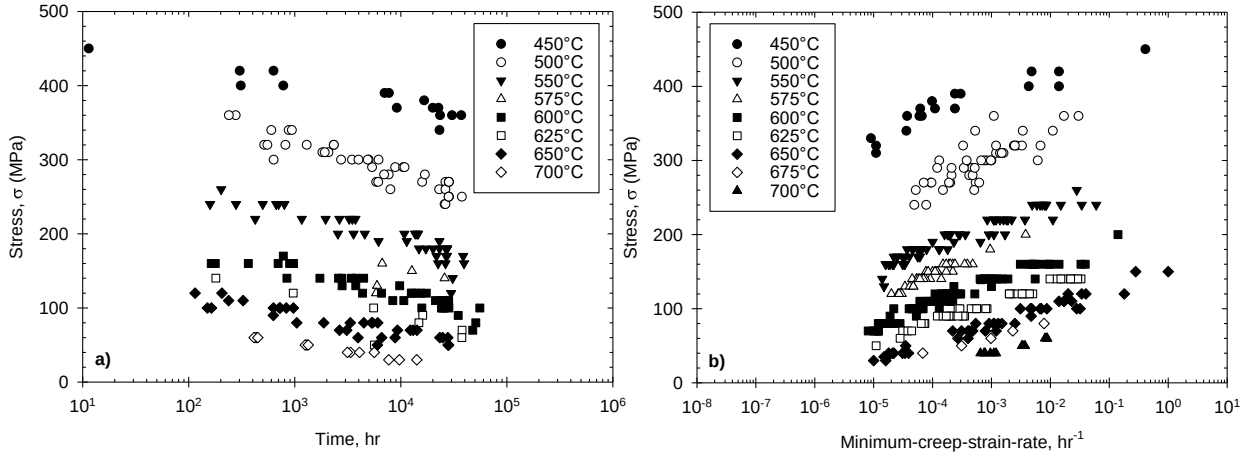


Figure 3.2 – Data gathered from the NIMS database for a) stress-rupture and b) minimum-creep-strain-rate for multiple forms, isotherms, and heat treatments [91].

Creep deformation data is also collected from the work of Kimura et al for P91 as illustrated in Figure 3.3 [92]. The data is given for a single isotherm 600°C and six stress levels (100, 110, 120, 140, 160, and 200 MPa). The data expands for more than $10^4$ hours which is more than three years of data. The data for P91 in this study is reported to be heat treated to the reference code MGC. The chemical composition is specified in this study and is shown in Table 3.5. The material is assumed to be a tube as the chemical compositions matches the one in NIMS. In this particular case for alloy P91, yield stress of the material at 600°C is $289\ MPa$ and the $\sigma_{TS} = 357\ MPa$.

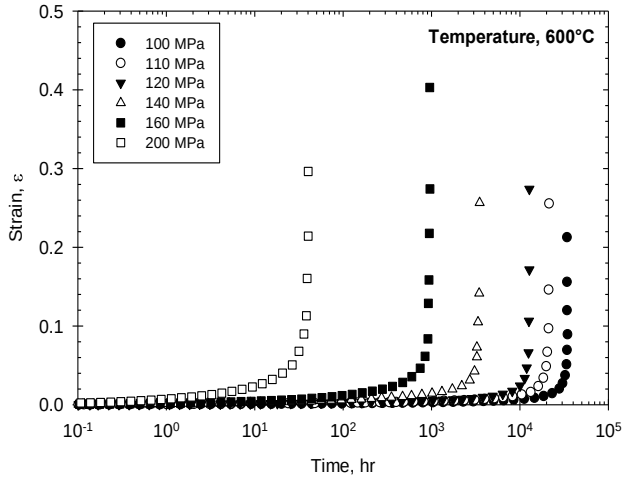


Figure 3.3 - Creep deformation curves for alloy P91 at 100, 110, 120, 140, 160, and 200 MPa and 600°C [92]. Note the x-axis is on a logarithmic scale.

Table 3.5– Nominal chemical composition (mass percentage) of Heat MGC for alloy 9Cr -1Mo-V-Nb (P91) [92]

| Element | Mass percent (mass%) |
|---|---|
| Fe | Bal. |
| C | 0.09 |
| Si | 0.29 |
| Mn | 0.35 |
| P | 0.009 |
| S | 0.002 |

| | |
|---|---|
| Ni | 0.28 |
| Cr | 8.70 |
| Mo | 0.90 |
| Cu | 0.032 |
| V | 0.22 |
| Nb* | 0.072 |

### 3.2 Inconel 718

The material used in Chapter 5 is Inconel-718. Data is obtained from the NIMS database and a study conducted from Stewart [95]. Inconel-718 is a nickel-based superalloy used in elevated temperature applications due to its heat and corrosion resistance. Applications of nickel-based superalloys are on aviation, combustion systems, gas turbines and others as it is creep resistant as well [93]. The unique properties of nickel-based alloys such as Inconel 718 are attributed to the strengthening phases γ′-Ni3(Al, Ti) and γ"-Ni3Nb precipitates [93-94]. The microstructure for Inconel-718 from NIMS and from Stewart's study are shown in Figure 3.4. It is observed that both specimens have $M_{23}C_6$, $M_7C_3$ carbides and $M_6C$ which is iron and molybdenum rich. Also, it is observed that in Stewart's specimen there are slip bands and $MC$ (vanadium rich).

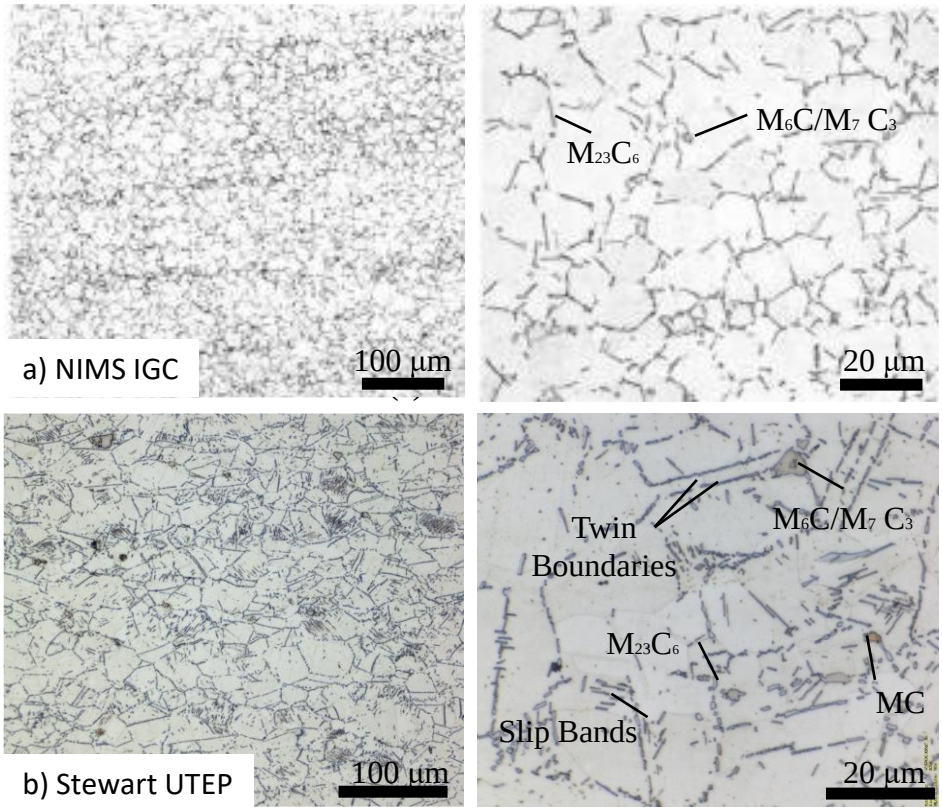


Figure 3.4 – Microscopy of Inconel-718 for (a) the NIMS database for heat treatment reference code IGC and (b) Stewart's study at UTEP.

Specimen used in the study conducted by Stewart, Figure 3.4 (b), is heat treated to $1325^{\circ}F$ for 8 hours, furnace cooled at $100^{\circ}F/hr$ to $1150^{\circ}F$ and held for 8.25 hours, and air cooled for a total aging time of 18 hours [95]. The chemical composition as reported from the mill test report (MTR) is shown in Table 3.6.

Table 3.6 - Chemical composition (wt%) of Inconel 718

| Element | MTR |
|---|---|
| Ni | 52.55 |
| Cr | 18.52 |
| Fe | 18.2 |
| Nb | 5.2 |

| | |
|---|---|
| Mo | 2.92 |
| Ti | 0.93 |
| Al | 0.52 |
| Co | 0.52 |
| C | 0.04 |
| Mn | 0.05 |
| Si | 0.08 |
| P | 0.007 |
| S | 0.0005 |
| B | 0.004 |
| Cu | 0.05 |

The average ultimate tensile strength of the specimen presented from Stewart as well as the ones reported by the NIMS database are shown in Table 3.7. It is observed that the ultimate tensile strength (UTS) of Stewart's specimens is lower, this is due to the larger and coarser grains obtained from the slow cooling rate [95]. Although, the coarse grains lead to a higher creep resistance. Chapter 5 considered the NIMS and Asadi's data sets to post-audit validation purposes [98-102]. The stress-rupture data from NIMS are presented for five isotherms (550, 600, 650, 700, 750 °C) at multiple heat treatments with their respective UTS. The study from Asadi has MCSR data for three isotherms (593, 649, 704 °C) but no UTS is reported, therefore, the average from NIMS is used for predictions.

Table 3.7 - Average ultimate tensile strength Inconel 718

| **Source** | Temperature (°C) | UTS (MPa) |
|---|---|---|
| **Stewart's** | 750 | 689 |
| **NIMS** | 550 | 1224 |
| **NIMS** | 593 | 1218 |
| **NIMS** | 600 | 1217 |
| **NIMS** | 649 | 1145 |
| **NIMS** | 650 | 1144 |

| | | |
|---|---|---|
| **NIMS** | 700 | 1003 |
| **NIMS** | 704 | 988 |
| **NIMS** | 750 | 818 |

Additionally, the creep activation energy, $Q_c^*$ of Inconel 718 has been determined by Sellers model to be between 300-450 $kJ/mol$. Other studies from Shöcks-Seeger-Wolf and by Chaturvedi reports values between 175-225 or 264 $kJ/mol$ [96-97]. As discussed for the ultimate tensile strength, the coarser gains give lower mechanical properties to the specimen, making it unrealistic to assume the higher properties suggested by Seller. Therefore, in this study, $Q_c^*$ is assumed to be 200 $kJ/mol$ which is the midpoint of the range suggested by Shöcks-Seeger-Wolf and Chaturvedi.

# CHAPTER 4 WILSHIRE-CANO-STEWART (WCS) MODEL

## 4.1 Introduction

In this chapter, the continuum damage mechanics (CDM) Wilshire-Cano-Stewart (WCS) model is introduced which enables long-term prediction of creep deformation, damage, and rupture. The WCS model is derived by combining the existing Wilshire and Sin-Hyperbolic (Sinh) equations [99]. The advantages and disadvantages of these individual models are detailed below. Regarding Wilshire,

- the stress-rupture and MCSR predictions [Eq. (2.6)-(2.7)] include temperature-dependence, can be calibrated analytically, and are accurate over a wide range of temperature and stress [48-54].
- the calibration process for creep deformation prediction [Eq. (2.8)] is complicated and tedious. A large database of creep deformation data is needed. Tables of time-to-strain for each creep strain, $\varepsilon_{cr}$ of interest must be generated and a set of $k_3$ and $w$ constants calibrated. The $k_3$ and $w$ constants are then regressed into a function of creep strain. Depending on the $k_3$ and $w$ functions, a closed and differentiable creep deformation equation may not exist. If a closed form does not exist, additional iterations are required at all material integration points of the elements, every time step, in a finite element problem. Subsequently, the Wilshire time-to-strain [Eq. (2.8)] has slower convergence rates in finite element analysis when compared to other creep models [51-59].
- the time-to-creep strain method is complicated to calibrate and does not track damage which lead to less accurate predictions [57,61].

Regarding Sinh,

- the Sinh model has been demonstrated to predict the creep deformation of a variety of alloys, with less stress-sensitivity, less mesh-dependence, and better convergence rates than other continuum damage mechanics-based creep models [2, 12-13, 72, 68, 85].
- disparate data is a problem in modeling where not enough data is given in the desire conditions, the Sinh model has been successful in calibrating disparate data and interpolating and extrapolating stress-rupture, minimum-creep-strain-rate (MCSR), and creep deformation [12].
- in the introduction of the accelerated creep testing (ACT) methods for metallic materials, the Sinh model predicted the ACT stepped isostress method (SSM) creep deformation data by tracking the damage at each step and the conventional response is then back out [95].
- the Sinh model has been used to predict uncertainty of creep deformation, damage, and rupture in alloys using probabilistic predictions [100].
- temperature-dependence is not stated explicitly in the Sinh model such that there exists a challenge in calibrating and validating the model for non-isothermal conditions [99].

The WCS model combines the capabilities of Wilshire and Sinh while overcoming the known deficits. The model is then to predict long-term creep deformation, damage, and rupture across a wide range of stresses and temperatures. The capabilities mention for each model are carried out which expands the capacities of the model for multiple applications.

### 4.2 Wilshire-Cano-Stewart (WCS) Model

Stress-rupture and MCSR, [Eq. (2.9)] and [Eq. (2.10)] respectively, are arranged as follows

$$t_f = \frac{\left[-\ln\left(\frac{\sigma}{\sigma_{TS}}\right)\Big/ k_1\right]^{\frac{1}{u}}}{\exp\left(-\frac{Q_c^*}{RT}\right)} \tag{4.1}$$

$$\dot{\varepsilon}_{\min} = \frac{\left[-\ln(\frac{\sigma}{\sigma_{TS}})\Big/ k_2\right]^{\frac{1}{v}}}{\exp\left(Q_c^*/RT\right)} \tag{4.2}$$

to obtain the $t_f$ and $\dot{\varepsilon}_{\min}$ as a function of stress and temperature. This allows the models to be incorporated the WCS model in the CDM Sinh framework.

The Wilshire stress-rupture [Eq. (2.9)] and MCSR [Eq. (2.10)] are then pulled into the Sinh creep-strain-rate [Eq. (2.26)] and damage evolution [Eq. (2.29)] equations respectively to furnish the WCS model as shown below

$$\dot{\varepsilon}_{cr} = \frac{\left[-\ln(\frac{\sigma}{\sigma_{TS}})\Big/ k_2\right]^{\frac{1}{v}}}{\exp\left(Q_c^*/RT\right)}\exp\left(\lambda\omega\right) \tag{4.3}$$

$$\dot{\omega} = \frac{\left[1-\exp(-\phi)\right]}{\phi}\frac{\exp\left(-\frac{Q_c^*}{RT}\right)}{\left[-\ln\left(\frac{\sigma}{\sigma_{TS}}\right)\Big/ k_1\right]^{\frac{1}{u}}}\exp\left(\phi\omega\right) \tag{4.4}$$

Note: the exponent 3/2 in the Sinh creep-strain-rate [Eq. (2.26)] is dropped for the ease of differentiation and has little impact on the accuracy of predictions. Damage [Eq. (2.33)] is preserved.

The WCS model is summarized in Table 4.1. The Wilshire material constants $\left(\sigma_{TS}, Q, k_1, u, k_2, v\right)$ remaining unchanged. The constants are calibrated following the classic

approach described in Figure 2.8 and in literature [53-56]. The Sinh material constants $(\lambda,\phi)$ change slightly due to the removal of the 3/2 exponent. This change can be accounted for by replacing the 3/2 and 2/3 exponents with unity in [Eq. (2.26)] and [Eq. (2.31)] respectively and solving for the material constants using the classic approach [2,12-13,72,68,85].

Table 4.1– Summary of WCS Model

| Feature | Equation | Origin | Material Constants |
|---|---|---|---|
| MCSR | [Eq. (4.2)] | Wilshire | $\sigma_{TS}, Q, k_2, v$ |
| SR | [Eq. (4.1)] | Wilshire | $\sigma_{TS}, Q, k_1, u$ |
| Creep-strain-rate | [Eq. (4.3)] | Combined | $\sigma_{TS}, Q, k_2, v, \lambda$ |
| Damage evolution | [Eq. (4.4)] | Combined | $\sigma_{TS}, Q, k_1, u, \phi$ |
| Damage | [Eq. (2.33)] | Sinh | $\phi$ |

The accuracy of the WCS model is assessed using one of the following quantitative measures: mean logarithmic error (MLE), the root mean square logarithmic error (RMSLE), or any desired objective function. The following equations ([Eq. (4.5)-(4.6)]) are examples used in literature to calibrate the WCS model the MLE approach

$$MLE = \frac{1}{N}\sum_{i=1}^{N}\frac{\left|\log\left(X_{sim,i}\right)-\log\left(X_{\exp,i}\right)\right|}{\left|\log\left(X_{\exp,i}\right)\right|} \tag{4.5}$$

where again $X_{\exp,i}$ and $X_{sim,i}$ are the experimental and simulated data respectively. Another form like the RMSLE is the following

$$RMSLE = \sqrt{\frac{1}{N}\sum_{i=1}^{N}\left(\log\left(X_{\exp,i}\right)-\log\left(X_{sim,i}\right)\right)^2} \tag{4.6}$$

where $X_{\exp,i}$ and $X_{sim,i}$ are the experimental and simulated data values respectively and $N$ is the number of data points.

### 4.3 Summary of Previous WCS Work

Introduced in 2021, the WCS model was first calibrated to alloy P91 at 600°C for multiple stress levels using the region splitting principle [63]. The Wilshire constants are calibrated following the steps in Figure 2.8. Steps to be completed are to

**(a)** determine the ultimate tensile strength and creep activation energy $Q_c^*$

**(b)** obtain Wilshire material constants $\left(k_1, u, k_2, v\right)$ from linear regression analysis.

**(c)** obtain stress-rupture and MCSR predictions using

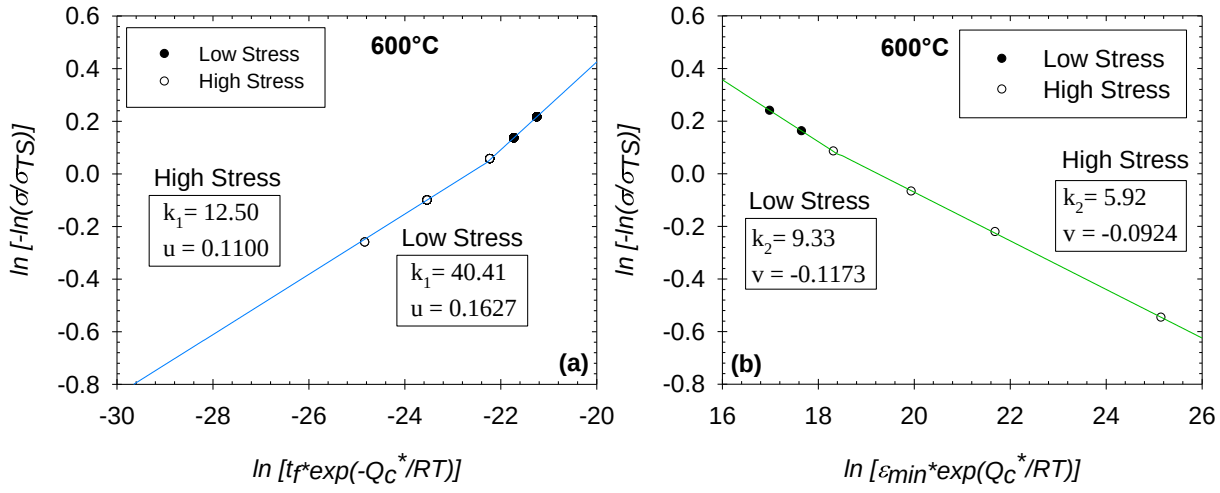


Figure 4.1– Normalized (a) stress-rupture (SR) and (b) minimum-creep-strain-rate (MCSR) data of P91 at 600°C for the calibration of $k_1, u$ and $k_2, v$ respectively with region splitting at a stress ratio of 0.31.

as illustrated in Figure 2.8, (a) the ultimate tensile strength of P91 at 600°C is $\sigma_{TS} \cong 347$ MPa. Literature furnishes an activation energy of $Q_c^* \cong 230\ kJmol^{-1}$ for a P91 tube [101]. step (b), described in 2.4Wilshire Model, shows the procedure to obtain $(k_1, u, k_2, v)$ as shown in Figure 4.1. The normalized stress-rupture and MCSR data of P91 for $(k_1, u, k_2, v)$ with region splitting at stress ratio $\sigma/\sigma_{TS} = 0.31$ is shown in Figure 4.1. Note that $k_1, k_2$ are obtained from the y-intercept, and $u$ ,$v$ from the slope of a linear regression equation. If $\sigma/\sigma_{TS} > 0.31$, then it is considered a high stress region. Material constants are summarized in Table 4.2 for both low stress and high stress. The high stress ratio material constants are of a lower magnitude than those obtained at low stress ratio.

Table 4.2– WCS material constants for P91 tube at 600˚C stress-rupture and MCSR with region splitting at a stress ratio of $\sigma/\sigma_{TS} = 0.31$

| Stress Ratio | $Q_c^*$ | $k_1$ | $u$ | $k_2$ | $v$ |
|---|---|---|---|---|---|
| $\sigma/\sigma_{TS}$ | $kJmol^{-1}$ | $hr^{-u}$ | unitless | $hr^{v}$ | unitless |
| Low | 230 | 40.41 | 0.1627 | 9.33 | -0.1173 |
| High | -- | 12.50 | 0.1100 | 5.92 | -0.0924 |

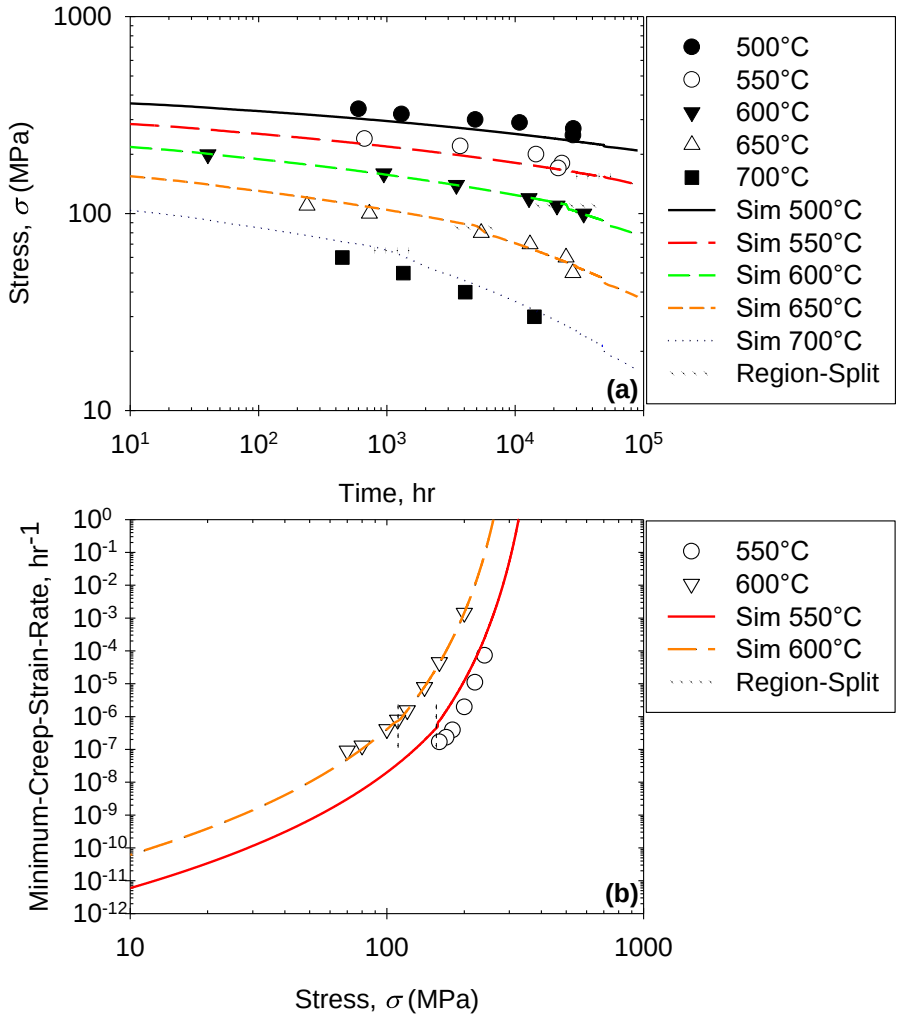


Figure 4.2– Predictions of alloy P91 for (a) stress-rupture (SR) and (b) minimum-creep-strain-rate (MCSR) using the WCS model [Eqs. (4.1)-(4.2)] compared to data from NIMS. Plotted on a log-log scale. The bold dotted line indicates the stress at which region-splitting occurs for each isotherm.

Finally in step (c), predictions of stress-rupture and MCSR are obtained as shown in Figure 4.2 where qualitatively the model has accurately predictions. Predictions of alloy P91 are made using region-splitting for stress-rupture and MCSR with a high degree of accuracy. Note the bold dotted line indicates the region-splitting. A summary of the quantitative errors is shown in Table 4.3 using the MLE approach [Eq. (4.5)]. Notice that the region splitting is used to determine

material constants and predictions. This method provides accurate predictions for P91, but a more in-depth analysis can be made to determine the impact on a larger data set and various materials.

Table 4.3– Mean logarithmic error (MLE) for stress rupture (SR) and minimum-creep-strain-rate (MCSR) predictions of alloy P91 at various isotherms

| Temperature, $T$ (°C) | **SR** unitless | **MCSR** unitless |
|---|---|---|
| 500 | 0.2235 | NA |
| 550 | 0.1121 | 0.1272 |
| 600 | 0.0079 | 0.0077 |
| 650 | 0.0608 | NA |
| 700 | 0.0879 | NA |

The Sinh approach is then used to calibrate material constants $\lambda$ and $\phi$ for damage and creep deformation predictions, after completing the outlined steps in Figure 2.8. The model was first calibrated using the Sinh analytical approach which consists of using [Eq. (2.27)] and the creep-strain-rate data to obtain $\lambda$ and [Eq. (2.30)] and the analytical damage rates [Eq. (2.31)] to obtain $\phi$. This calibration is done after the removal of the power 3/2 in the original Sinh approach [Eq. (2.26)]. A summary of the calibrate material constants for P91 is shown in Table 4.4. An alternative to calibrate these material constant, especially $\phi$, is using a numerical method with objective functions such as those describe in [Eq. (4.5)-(4.6)].

Table 4.4– WCS material constants $\lambda$ and $\phi$ for P91 Tube at 600°C

| Temperature, $T$ (°C) | Stress, $\sigma$ (MPa) | $\lambda$ unitless | $\phi$ unitless |
|---|---|---|---|
| 600 | 100 | 5.72 | 5.03 |
| 600 | 110 | 5.30 | 3.99 |
| 600 | 120 | 5.13 | 3.23 |
| 600 | 140 | 4.30 | 2.61 |
| 600 | 160 | 4.03 | 2.53 |
| 600 | 200 | 3.81 | 2.25 |

The $\lambda$ and $\phi$ material constants, from Sinh, are temperature and stress dependent. To account for these dependency, Eyring functions are applied to $\lambda$ and $\phi$ as follows

$$\lambda = \lambda_0 \exp\left(\frac{-V_\lambda^* \sigma}{k_b T}\right) \tag{4.7}$$

$$\phi = \phi_0 \exp\left(\frac{-V_\phi^* \sigma}{k_b T}\right) + 1 \tag{4.8}$$

where $V_\lambda^*$ and $V_\phi^*$ are the activation volumes (or stress coefficients) corresponding to $\lambda$ and $\phi$, $k_b$ is the Boltzmann constant (1.3806E-23 J·K$^{-1}$), and $\lambda_0, \phi_0$ are material constants [109-110].

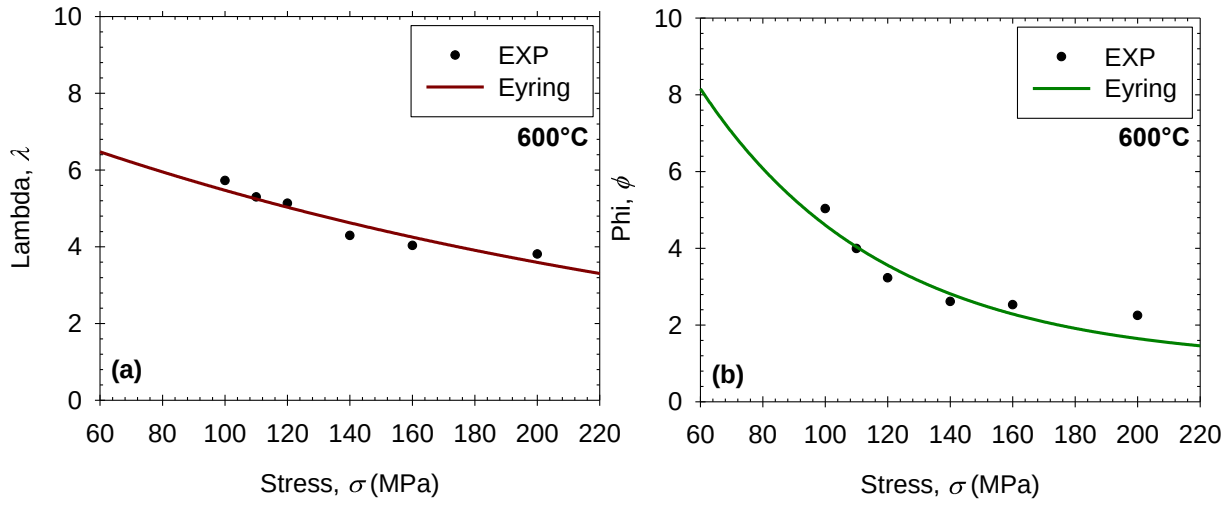


Figure 4.3 – Eyring relationship of the (a) $\lambda$ [Eq. (4.7)] and (b) $\phi$ [Eq. (4.8)] material constants plotted against calibrated values for alloy P91.

The Eyring functions of $\lambda$ [Eq. (4.7)] and $\phi$ [Eq. (4.8)] are plotted with respect to the calibrated constants Table 4.4 as shown in Figure 4.3. Region splitting is not observed in the $\lambda$

and $\phi$ constants. The Eyring constants are shown in Table 4.5 which are used for parametric simulations at a variety of temperatures and stresses.

Table 4.5– Eyring constants for $\lambda$ and $\phi$ material constants [Eqs. (4.7)-(4.8)] for P91 Tube

| Equation | Coefficients, $\lambda_0, \phi_0$ unitless | Activation Volumes, $V_\lambda^*, V_\phi^*$ $(cm^3)$ |
|---|---|---|
| [Eq. (4.7)] | 8.33 | 5.07E-23 |
| [Eq. (4.8)] | 20.02 | 2.07E-22 |

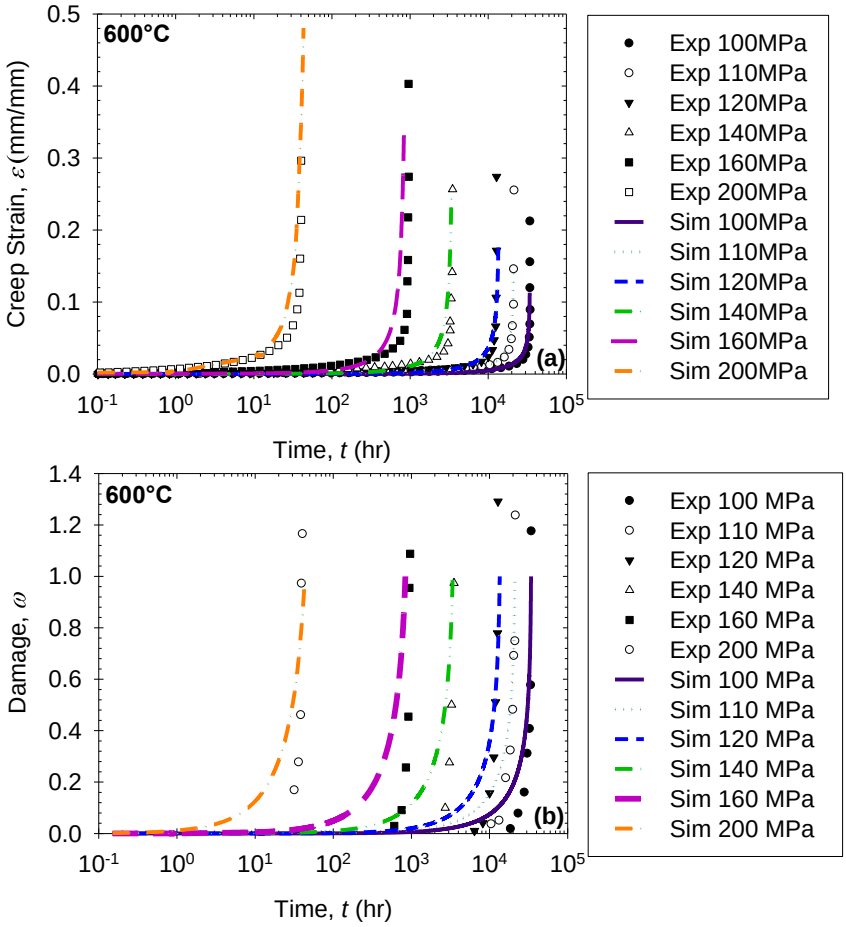


Figure 4.4 – Predictions of (a) creep deformation and (b) damage using the WCS model [Eqs.(4.3),(4.4)] for alloy P91 subject to 100, 110, 120, 140, 160, and 200 MPa at 600°C. Time is on a logarithmic scale.

Creep deformation and damage predictions using the WCS model [Eq. (4.3)-(4.4)] are shown in Figure 4.4(a) and (b) respectively. Qualitatively, the creep deformation predictions are accurate, closely matching the creep deformation curves through rupture at each stress level. Creep ductility is under-predicted, non-conservative, but reasonable considering the massive creep-strain-rate ratios observed in the experiments as well as typical scatter observed creep ductility data. The correct trend is predicted where creep ductility increases with stress. Damage predictions are compared to analytical damage in Figure 4.4(b). Only the analytical damage after the MCSR has been reached is reported. In all cases, the model predictions are accurate, and damage is unity at rupture. The MLE of the predictions are presented in Table 4.6. Quantitative, the creep deformation predictions do not exceed a 0.20 error for each stress level. The error is reasonable considering that the rupture and MCSR prediction are accurate and most of the error is carried in the creep ductility under-prediction. The damage errors as well are on a reasonable level as well. It is observed that 160 MPa has almost a 0.30 error this is expected as it corresponds to the highest creep ductility presented from the experimental data.

Table 4.6 – Mean logarithmic error (MLE) of creep deformation and damage predictions of alloy P91 at 600°C

| Stress (MPa) | **Creep Deformation** unitless | **Damage** unitless |
|---|---|---|
| 100 | 0.1776 | 0.0931 |
| 110 | 0.1710 | 0.0772 |
| 120 | 0.1821 | 0.1356 |
| 140 | 0.2062 | 0.1220 |
| 160 | 0.1964 | 0.2925 |
| 200 | 0.1274 | 0.1031 |

### 4.4 Mathematical Extremes

Multiple mathematical extreme conditions are considered to understand the WCS model and create boundary conditions for multiple applications. The following conditions are considered as mathematical extremes of the model; when the specimen is under compression $\sigma = -\sigma$, when the nominal stress reaches the ultimate tensile strength $\sigma = \sigma_{TS}$ and at a negative tensile strength, $\sigma = -\sigma_{TS}$ at initial testing conditions where $\sigma = 0$, if $\sigma = \sigma_{ys}$, when temperature $T = T_m$ where $T_m$ is the melting temperature.

The first conditions considered are for stress which relates to the numerator of the creep strain rate and denominator of the damage rate as shown

$$\left[ -\ln\left(\frac{\sigma}{\sigma_{TS}}\right) \Big/ k_2 \right]^{\frac{1}{v}} \tag{4.9}$$

$$\frac{1}{\left[ -\ln\left(\frac{\sigma}{\sigma_{TS}}\right) \Big/ k_1 \right]^{\frac{1}{u}}} \tag{4.10}$$

Applying the conditions for creep strain rate, and using a limit approach

$$\lim_{\sigma \to -\sigma_{TS}} \left[ -\ln\left(\frac{\sigma}{\sigma_{TS}}\right) \Big/ k_2 \right]^{\frac{1}{v}}$$

Compressive UTS $$\left[ -\ln\left(\frac{-\sigma_{TS}}{\sigma_{TS}}\right) \Big/ k_2 \right]^{\frac{1}{v}} \tag{4.11}$$

$$\left[ -\left(\pi \cdot i\right) / k_2 \right]^{\frac{1}{v}}$$

Compressive Creep $$\lim_{\sigma \to -\sigma} \left[ -\ln\left(\frac{\sigma}{\sigma_{TS}}\right) \Big/ k_2 \right]^{\frac{1}{v}} \tag{4.12}$$

$$\left[-\ln\left(\frac{-\sigma}{\sigma_{TS}}\right)\Big/k_2\right]^{\frac{1}{v}}$$

$$\left[\left(-\ln\left(\frac{-\sigma}{\sigma_{TS}}\right)-\pi\,\mathrm{i}\right)\Big/k_2\right]^{\frac{1}{v}}$$

$$\lim_{\sigma\to 0^{+}}\left[-\ln\left(\frac{\sigma}{\sigma_{TS}}\right)\Big/k_2\right]^{\frac{1}{v}}$$

Stress = 0

$$\left[-\ln\left(\frac{0}{\sigma_{TS}}\right)\Big/k_2\right]^{\frac{1}{v}} \qquad (4.13)$$

*undefined*

$$\lim_{\sigma\to\sigma_{TS}}\left[-\ln\left(\frac{\sigma}{\sigma_{TS}}\right)\Big/k_2\right]^{\frac{1}{v}}$$

Stress = UTS

$$\left[-\ln\left(\frac{\sigma_{TS}}{\sigma_{TS}}\right)\Big/k_2\right]^{\frac{1}{v}} \qquad (4.14)$$

0

Applying the stress conditions to the damage rate equation then

$$\lim_{\sigma\to-\sigma_{TS}}\frac{1}{\left[-\ln\left(\frac{\sigma}{\sigma_{TS}}\right)\Big/k_1\right]^{\frac{1}{u}}}$$

Compressive UTS

$$\frac{1}{\left[-\ln\left(-\frac{\sigma_{TS}}{\sigma_{TS}}\right)\Big/k_1\right]^{\frac{1}{u}}} \qquad (4.15)$$

$$\frac{1}{\left[-\left(\pi\cdot i\right)/k_1\right]^{\frac{1}{u}}}$$

$$\lim_{\sigma \to -\sigma} \frac{1}{\left[ -\ln\left( \frac{\sigma}{\sigma_{TS}} \right) \Big/ k_1 \right]^{\frac{1}{u}}}$$

Compressive Creep

$$\frac{1}{\left[ -\ln\left( -\frac{\sigma}{\sigma_{TS}} \right) \Big/ k_1 \right]^{\frac{1}{u}}} \tag{4.16}$$

$$\frac{1}{\left[ \left( -\ln(\frac{-\sigma}{\sigma_{TS}}) - \pi \mathrm{i} \right) \Big/ k_1 \right]^{\frac{1}{u}}}$$

$$\lim_{\sigma \to 0^+} \frac{1}{\left[ -\ln\left( \frac{\sigma}{\sigma_{TS}} \right) \Big/ k_1 \right]^{\frac{1}{u}}}$$

Stress = 0

$$\frac{1}{\left[ -\ln\left( \frac{0}{\sigma_{TS}} \right) \Big/ k_1 \right]^{\frac{1}{u}}} \tag{4.17}$$

*undefined*

$$\lim_{\sigma \to \sigma_{TS}} \frac{1}{\left[ -\ln\left( \frac{\sigma}{\sigma_{TS}} \right) \Big/ k_1 \right]^{\frac{1}{u}}}$$

Stress = UTS

$$\frac{1}{\left[ -\ln\left( \frac{\sigma_{TS}}{\sigma_{TS}} \right) \Big/ k_1 \right]^{\frac{1}{u}}} \tag{4.18}$$

*undefined*

It is shown that at the compressive ultimate tensile strength, the limit of the equation is a complex number $\left[-\left(\pi\cdot i\right)/k_2\right]^{\frac{1}{v}}$ for the strain rate [Eq. (4.11)] and $1\Big/\left[-\left(\pi\cdot i\right)/k_1\right]^{\frac{1}{u}}$ for the damage rate [Eq. (4.15)]. Likewise, it is observed under compressive creep where the limit as it approaches negative stress (compression) is $\left[\left(-\ln(\frac{-\sigma}{\sigma_{TS}})-\pi\,\mathrm{i}\right)\Big/k_2\right]^{\frac{1}{v}}$ for the strain rate [Eq. (4.12)] and $1\Big/\left[\left(-\ln(\frac{-\sigma}{\sigma_{TS}})-\pi\,\mathrm{i}\right)\Big/k_1\right]^{\frac{1}{u}}$ for the damage rate [Eq. (4.16)]. The domain for a $\mathrm{f}\left(x\right)=\ln\left(x\right)$ is $\left(0,\infty\right)$, which means that as $\sigma/\sigma_{TS}\rightarrow$ *negative* then it is outside the domain. This behavior is expected as the current form of the model is uniaxial, which can be replace by the von mises stress and transform it to a multiaxial model capable of capturing shear and compressive stress. Using the creep potential hypothesis in the following form accommodates for von mises

$$d\dot{\varepsilon}_{ij,cre}=\frac{3}{2}\frac{d\varepsilon^{*}}{\sigma^{*}}\frac{d\psi}{d\sigma_{ij}} \tag{4.19}$$

where $d\varepsilon^{*}$ is the equivalent strain increment, $\sigma^{*}$ is the equivalent stress, and $\psi\left(\sigma_{ij}\right)=\sigma^{*2}/3$ is the von mises potential function [62]. It is recommended, in the current form, to use the model under the domain $\left(0,\infty\right)$ to avoid dealing with complex numbers. As stress approaches 0, the logarithmic function tends to infinity but as evaluated in [Eq. (4.13)] and [Eq. (4.17)], the model becomes undefined because of the power function, this is true for both the strain rate and damage rate. As the model approaches the ultimate tensile strength, the strain rate, evaluated in [Eq. (4.14)] is 0 which is desired, as it means the model turns itself off in the ultimate tensile strength, which means almost instant rupture. As it approaches ultimate tensile strength for the damage rate, [Eq.

(4.18)], the model should tend to an infinitely large number, but because of the power the model becomes undefined as well.

A condition not evaluated from [Eq. (4.11)-(4.18)] is when stress is at the yield point or near the yield point, $\sigma = \sigma_{ys}$. The damage rate of the model even at the first step, is drastically high, which causes creep ductility to be exaggerated as well, discussed more in-depth in the parametric simulation section. The WCS model, as many creep models, increases in ductility as stress increases. Even when the model is close to yield (typically at $0.8\sigma = \sigma_{ys}$), a drastic increase in ductility is observed. It is recommended to use the WCS model at least under the following conditions $\sigma < \sigma_{ys}$ for more accurate predictions.

The next conditions considered are for temperature which relates to the denominator of the creep strain rate and numerator of the damage rate as shown

$$\frac{1}{\exp\left(Q_c^* / RT\right)} \tag{4.20}$$

$$\exp\left(-Q_c^* / RT\right) \tag{4.21}$$

where the conditions applied are at $T = T_m$. Applying this condition then both strain rate and damage rate temperature portion are in the following form

$$\frac{1}{\exp\left(Q_c^* / RT_m\right)} \tag{4.22}$$

$$\exp\left(-Q_c^* / RT_m\right) \tag{4.23}$$

where the model at the melting temperature has no mathematical constraints. If the material constants calibrated for alloy P91 at the melting temperature and at 1MPa and considering an ultimate tensile strength of almost 4MPa the model predicts rupture in less than 10 minutes which is in accordance with what it is expected for a material at the melting point. Considering the

material constants use for P91 and the melting temperature, there is a discrepancy as the rupture time is predicted in minutes but material constants $\lambda$ and $\phi$ prevents the model to reach unity at the rupture. Any temperature below, the creep range $0.3T_m < T < 0.6T_m$ has no mathematical constraints either and has almost infinite life depending on the loading conditions. A summary of the mathematical extreme conditions applied to the WCS model is provided in Table 4.7.

Table 4.7 – Summary of mathematical extreme conditions for the WCS model.

| | $\dot{\varepsilon}_{cr}$ | $\dot{\omega}$ |
|---|---|---|
| $\sigma = -\sigma_{TS}$ | $\left[-(\pi \cdot i)/k_2\right]^{\frac{1}{v}}$ | $\frac{1}{\left[-(\pi \cdot i)/k_1\right]^{\frac{1}{u}}}$ |
| $\sigma = -\sigma$ | $\left[\left(-\ln(\frac{-\sigma}{\sigma_{TS}}) - \pi \mathrm{i}\right)/k_2\right]^{\frac{1}{v}}$ | $\frac{1}{\left[\left(-\ln(\frac{-\sigma}{\sigma_{TS}}) - \pi \mathrm{i}\right)/k_1\right]^{\frac{1}{u}}}$ |
| $\sigma = 0$ | Undefined | Undefined |
| $\sigma = \sigma_{ys}$ | High Ductility | High Damage Rate |
| $\sigma = \sigma_{TS}$ | 0 | Undefined |
| $T < 0.3T_m$ | Low Ductility/ Low MCSR | Low damage rate/ Approaches Infinite life |
| $T = T_m$ | $\lambda$ and $\phi$ prevents accurate ductility | $\lambda$ and $\phi$ prevents damage development |

### 4.5 WCS Parametric Simulations

Parametric simulations are performed to understand the behavior of the WCS model under non-extreme conditions. Isothermal and isostress simulations are executed with variations of stress and temperatures respectively. Four cases of isothermal simulations (400, 500, 600, 700˚C) are

performed as well as fours cases for isostress (200, 300, 400, 500 MPa). Parametric simulations are performed for alloy P91 using material constants outline in Table 4.2 and Table 4.5. Region-slipping is not considered and rather the material constants for high stress ratios are utilized. The purpose of the simulations is to provide an understanding of the model's behavior rather than a validation of the extrapolation ability. Both $\lambda$ and $\phi$ are calibrated for every iteration of the simulations. Isothermal parametric simulations are given in Figure 4.5 and isostress simulations are given in Figure 4.6 for alloy P91.

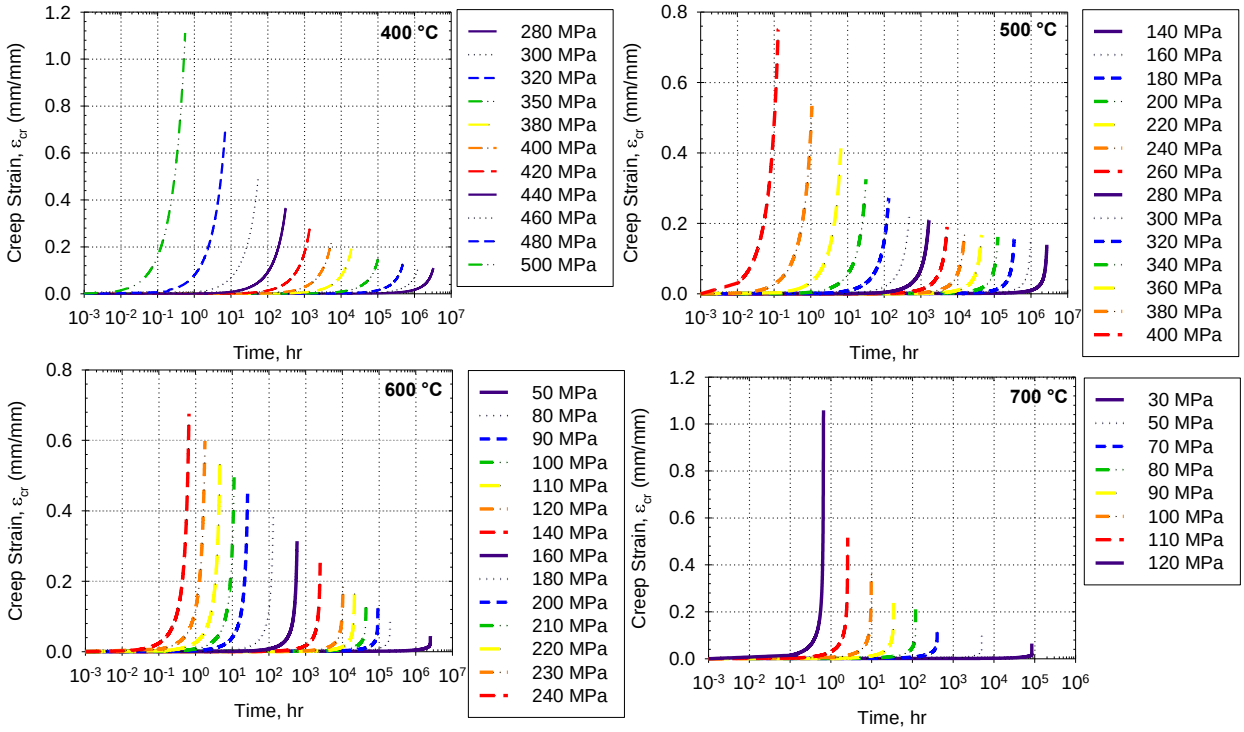


Figure 4.5 – Isothermal WCS parametric simulations (400, 500, 600, 700°C) for alloy P91 at multiple stress levels.

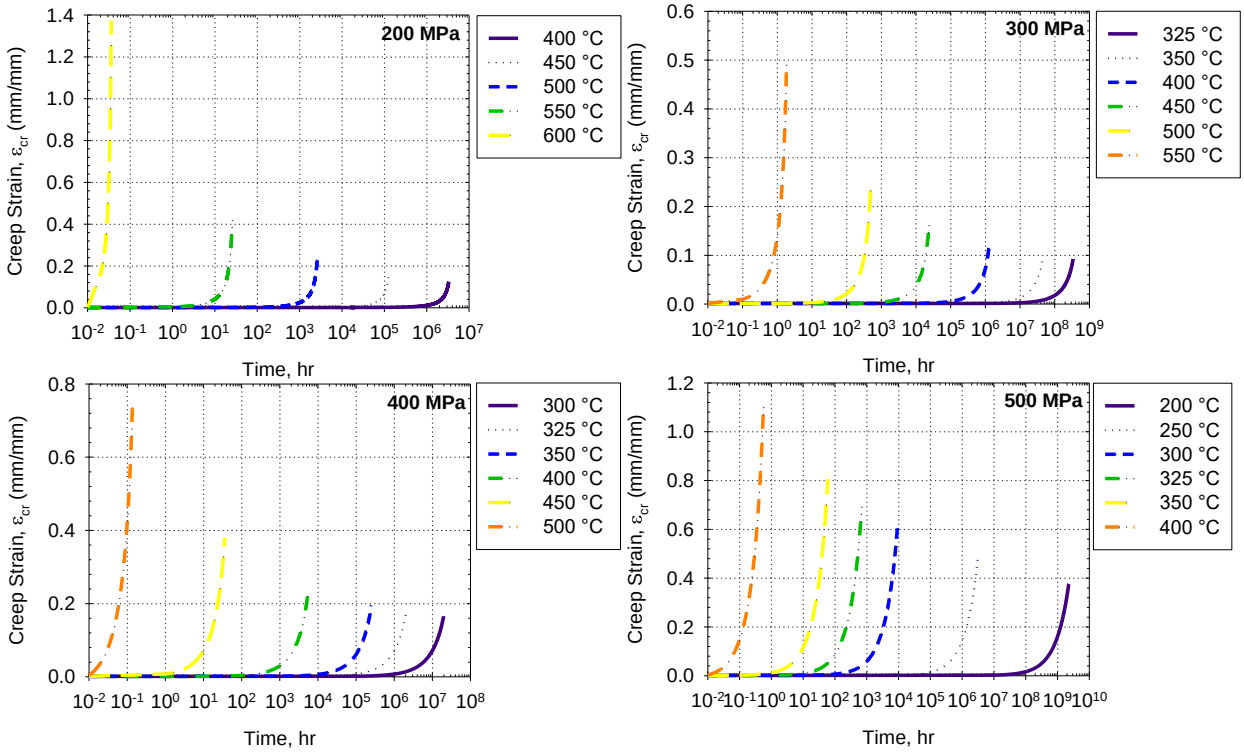


Figure 4.6 – Isostress WCS parametric simulations (200, 300, 400, 500 MPa) for alloy P91 at multiple temperatures.

Parametric simulations given in Figure 4.5 and Figure 4.6 are performed at arbitrary temperatures and stresses. At isothermal simulations (Figure 4.5), it is observed that the closer the stress gets to the yield strength, there is an increase in creep ductility. Simulations are performed in non-extreme conditions, and therefore yield strength is never reached, rather it was kept under $0.85\sigma_{ys}$. A creep ductility reaching unity or 100% strain is not typical for many materials, as shown for temperatures 400 and 700˚C as well as stresses 200 and 500 MPa. Many factors can contribute to such a high ductility such as the lack of isotherms to calibrate the creep deformation, therefore resulting in a $\lambda$ and $\phi$ calibrated only through the Eyring's approach for multiple isothermal predictions. Because $\lambda$ and $\phi$ control both the trajectory of the damage and the damage evolution, it is safe to assume that a limited data set to calibrate both material constants

would result in uncertainty in ductility and damage. In Figure 4.6, the ductility increase is seen more drastically as less temperatures are considered for the parametric study. Note that when variating temperature, the ultimate tensile strength varies as well, therefore only those temperatures reported by NIMS in Table 3.3 for P91 are considered. It is important to note that any lower stresses or temperatures than those use for both Figure 4.5 and Figure 4.6 results in what is known as infinite life. Overall, the WCS model has good extrapolative and interpolative abilities capable of reproducing multiple combinations of stress and temperature predictions with just one calibrated isotherm. The model has reasonable mathematical limitations and follows the expected trend for ductility whereas stress increases so as ductility.

### 4.6 Design Requirements

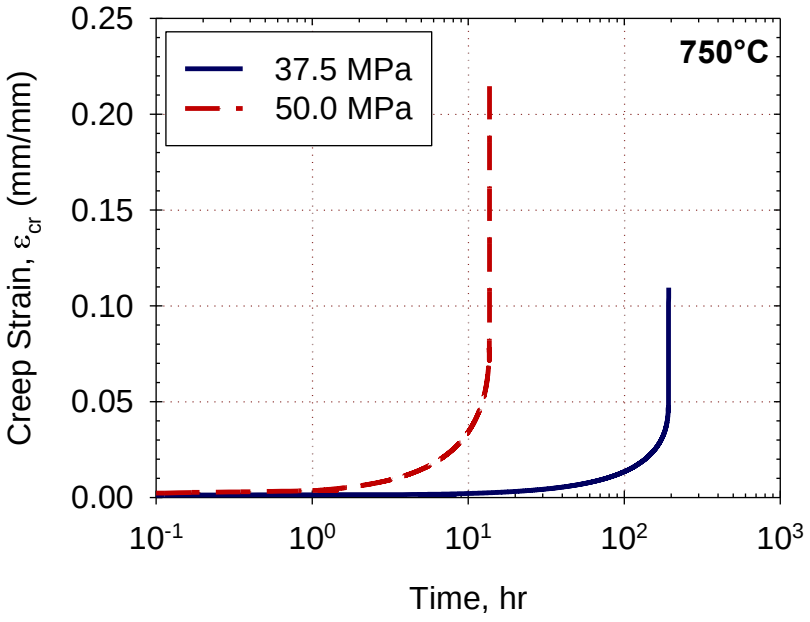


Figure 4.7 – Parametric simulation of design requirements for coal fired Advance Ultrasupercritical (A-USC) power plant for alloy P91 at 750˚C. Note the x-axis are logarithmic scale.

After parametric simulations are performed, simulations of design requirements can be performed as well. A parametric simulation of the design requirements of coal fired advance Ultrasupercritical (A-USC) power plants is given in Figure 4.7 for alloy P91 at 750°C and stress levels (37.5 and 50 MPa). Requirements of 100,000 hours of stress rupture for new alloys at 100 MPa and 750°C has been imposed by the THERMIE consortium for new alloys for coal fired A-USC application [107-108]. Alloy P91 does not perform under these conditions and failure is reach almost instantaneously thus the simulated stresses are lower than 100MPa. It is observed that, the model captures ductility consistently and that rupture times are around 193 and 13 hours respectively. Further analysis is required to conclude that P91 is not suitable under these conditions but according to the parametric simulation it is recommended to find a material with greater resistance.

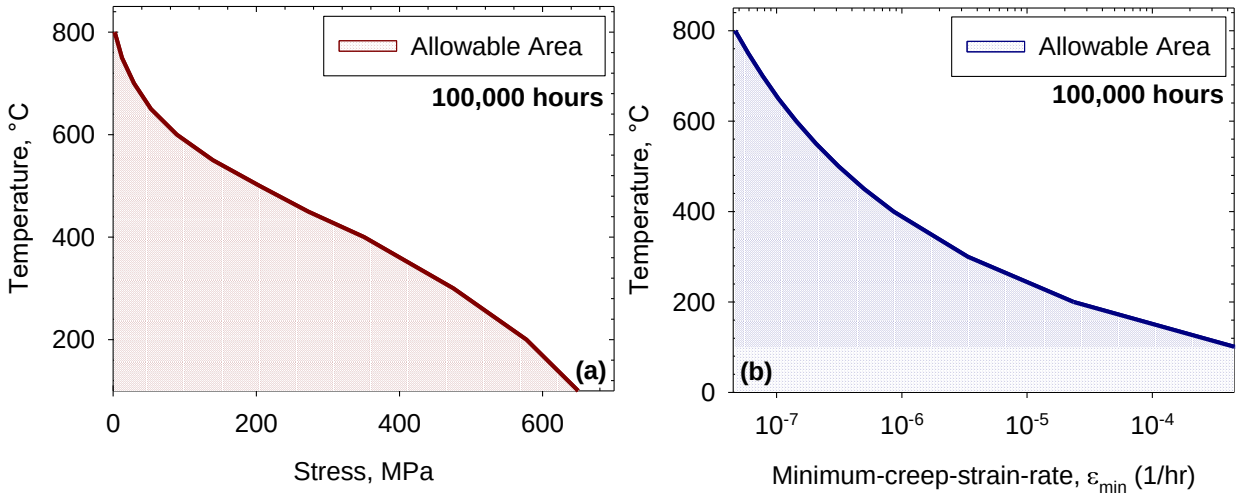


Figure 4.8 – Maximum allowable temperature compared to (a) stress and (b) minimum-creep-strain-rate (MCSR) for 100,000 hours for alloy P91 using the WCS model stress-rupture and MCSR equations. Note that the x-axis of (b) MCSR is on logarithmic scale for better visibility.

As a tool for design engineers, plots of allowable temperature compared to stress and MCSR for 100,000 hours of alloy P91 using the WCS stress-rupture and MCSR equations are shown in Figure 4.8. This tool is beneficial as decisions can be made depending on the application that is desired. Typically, a plot of temperature and stress is enough to make decisions but if a

specific minimum rate is desired Figure 4.8 (b) can be useful as well. Note that the x-axis on Figure 4.8 (b) is in logarithmic scale for better visibility.

## 4.7 Conclusions

The "WCS" continuum-damage-mechanics-based (CDM) Wilshire model has been introduced. The WCS model is demonstrated to accurately predict the stress-rupture, minimum-creep-strain-rate, creep deformation, and damage of alloy P91 across a range of stress and temperature. The model is calibrated analytically with the calibration approaches of the Wilshire and Sinh models preserved; meaning, existing constants for each model can be employed in the WCS model. The explicit definitions of stress and temperature-dependence provided by the Wilshire equations along with additional Eyring functions ensure accurate interpolation and extrapolations across multiple isotherms and isostress conditions. The CDM approach allows the model to accurate predict creep under dynamic loading conditions and account for increased creep-strain-rates due to the exhaustion of the material. The coupled-differential equations of the WCS model are convenient for FEA implementation and are proven to have reasonable mathematical limitations. Parametric simulations are given to validate the ability of the model to interpolate and extrapolate outside of the conditions use for calibration.

# CHAPTER 5 ACCELERATED CREEP TEST QUALIFICATION OF CREEP-RESISTANCE USING THE WCS CONSTITUTIVE MODEL AND STEPPED ISOSTRESS METHOD

## 5.1 Introduction

Recent material developments have increased the need for material qualification in shorter periods of time. Turbomachinery and pressure vessel components are subject to high temperatures which promotes the need for new heat-resistance materials [1]. Materials are expected to be suitable for a 30-year service life for steam turbines, boiler components, and other high temperature applications such as IGT's [111]. To qualify the creep-resistance of materials conventional creep tests (CCTs) are to be conducted. The ASME B&PV III code requires that newly developed materials must have 10,000+ hours of experiments for each heat to be approved for service [11]. As material development has increase, particularly with newly additive manufacturing technologies, this process has become too costly and not feasible; especially, considering the uncertainty of creep testing. It has been shown for multiple steels that uncertainty governs data, where, if the same conditions of temperature and stress are given, a scatter on creep curves is projected [103]. Conversely, attempts to lessen the uncertainty with different combinations of temperature and stress results in a similar scatter [112]. As a result of, cost, uncertainty, protocols for testing; newly discovered materials are put into service in a period of 10-20 years. Material designs and processes must be accelerated to provide faster solutions to problems like efficiencies for turbomachinery, steam turbines, and other energy-based applications [113]. There is a need for accelerated testing methods that can characterize materials faster and models that can predict creep behaviors reliably. In this chapter, the WCS model is used to assess the creep-resistance of material

Inconel 718 using an accelerated creep test (ACT) method called the stepped-isostress method (SSM).

### 5.2 Stepped-Isostress Method (SSM)

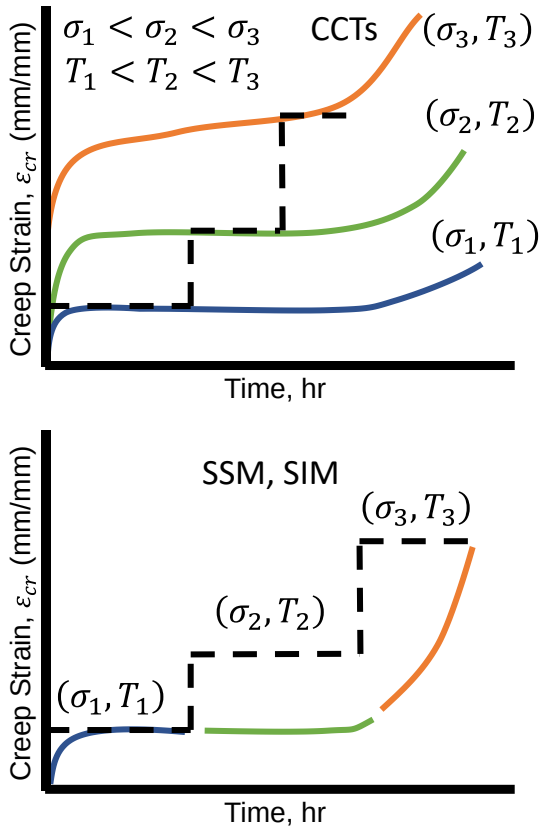


Figure 5.1 - Time-temperature-stress superposition principle (TTSSP) illustrated with conventional creep test (CCTs) and then projected in the accelerated creep test (ACT) for either stepped-isostress method or stepped-isothermal method (SIM). Note that the dotted line is the stepped increase of either stress or temperature.

Accelerated methods such as ACT are well-accepted to determine the remaining life of components at elevated temperatures [114]. These ACT methods have been established using

conditions such as a linear cumulative damage law, stress ratio cyclic loading for fatigue applications, and the time-temperature-stress superposition (TTSSP) principle [114-115].

It has been proven experimentally, that stress has a similar impact as temperature in viscoplastic materials [116]. This suggests that stress, temperature, and time can be manipulated to decrease the duration of experiments, as it describes the accelerated aging process [117]. The TTSSP in creep deformation can be used if the creep-strain-rate of an experiment conducted at elevated temperatures or stress can replicate that of a CCT as shown in Figure 5.1. Although both temperature and stress variations can be performed together, this method is typically divided into two types, the stepped-isothermal method (SIM) and the stepped-isostress method (SSM). Typically, this relationship is given in the following form

$$\begin{array}{lll} \textbf{Conventional} & \textbf{SIM} & \textbf{SSM} \\ \dot{\varepsilon}_{cr}\left(\sigma_0, T_0, t\right) & = \dot{\varepsilon}_{cr}\left(\sigma_0, T_i, \dfrac{t-t_{0,i}}{\phi_i}\right) & = \dot{\varepsilon}_{cr}\left(\sigma_i, T_0, \dfrac{t-t_{0,i}}{\phi_i}\right) \end{array} \tag{5.1}$$

where $\dot{\varepsilon}_{cr}$ is creep strain rate, $T_0$ is the service temperature, $\sigma_0$ service stress, $T_i$, and $\sigma_i$ are the stepped temperature and stress, $\phi_i$ the shift factor, and $t_{0,i}$ is the virtual start time. Multiple stepped increases can be performed to a specimen and $\phi_i$ is calculated using empirical equations.

In this study, SSM is used as a preferred method, as it is easier experimentally to obtained load control rather than temperature control. Using the empirical equations, the SSM method has been assess for multiple polymers and polymeric composite materials and has been successful [109-110,118-123]. Recently, the SSM has been exploited to be used in metals as well. In a study conducted by Stewart et. al, a SSM test matrix captured the observed creep-resistance phenomenon with the hyperbolic sine model, or Sinh [95]. In doing so, this study provided strong evidence that the SSM approach could be extended to metallic materials. There still work to be done, as the

CCTs were used during the calibration process. The Sinh model has some limitations as some constants have stress and temperature dependency, alternative models, such as the WCS, can be utilized to verify how well SSM performs with metallic materials.

### 5.3 Objective of SSM and WCS

Past work has shown a variety of applications of the SSM in polymer and polymeric composite materials. However, SSMs require further development for applications with metal alloys [95,124]. The Sinh model has some limitations as most material constants are obtained purely numerically. Some other material constants have stress and temperature dependency. There have not been extrapolative and interpolative predictions using solely the SSM data for metallic materials, which would not only prove the feasibility of the method but would allow turbomachinery industries to perform short time SSM experiments and make CCT predictions even when data is not given.

The objective of this Chapter and study is to qualify the accelerated creep-resistance of Inconel 718 using the WCS model and SSMs to predict CCTs. Data is provided from previous studies of Inconel 718 at 750°C [95]. The SSM data of this study is used to calibrate the model. After calibrating the SSMs, and with the obtained material constants, the results are compared to Inconel 718 data obtained from studies conducted by the National Institute of Material Science (NIMS), Asadi, as well as the CCTs obtained from Stewart et al.

### 5.4 SSM Test Matrix

The test matrix proposed by Stewart's study is to perform CCTs at 750 °C at multiple stress level (100, 200, 300, and 350 MPa). The data is used for post-audit validation as those CCTs are not included in the calibration method. Five SSMs are performed as well at 750 °C with different initial stresses (100, 150, 200, 250, and 300 MPa) and a final stress of 350 MPa. Four steps are

considered, and the step size is defined as (final stress – initial stress)/(N-1) where N is the number of steps. The SSM considers deformation mechanism maps and hold times of 5 hours using time-temperature (TTT) and -precipitation (TTP) diagrams. The resulting creep behavior is shown in Table 5.1 [95].

Table 5.1 - SSM and CCT data for Inconel 718 at 750°C [95].

| Specimen ID | Initial Stress $\sigma_0$ (MPa) | MCSR at $\sigma_0$ ($hr^{-1} \times 10^{-6}$) | Rupture $t_r$ (hr) | Creep at $t_r$ (%) |
|---|---|---|---|---|
| SSM_100 | 100 | 4.00 | 85.95 | 13.8 |
| SSM_150 | 150 | 2.86 | 68.42 | 11.7 |
| SSM_200 | 200 | 7.98 | 61.25 | 14.7 |
| SSM_250 | 250 | 18.8 | 62.88 | 13.3 |
| SSM_300 | 300 | 155 | 52.37 | 14.6 |
| CCT_100 | 100 | 8.17 | 1535.4 | 2.85 |
| CCT_200 | 200 | 50.0 | 362.5 | 27.7 |
| CCT_300 | 300 | 155 | 89.1 | 15.5 |
| CCT_350 | 300 | 376 | 42.72 | 13.1 |

### 5.5 Modified WCS for SSM Calibration

While the WCS model has a clear calibration approach, there exist limitations and considerations to the method when applying it to SSM. In conventional test methods, rupture time is a physically meaningful property as it relates to the actual critical point of the material. In SSM, due to the increments of stress and the damage caused by the multiple steps, rupture at the final stress does not necessarily correlates to the actual material rupture time. This does not allow the conventional WCS and Wilshire methods to calibrate both $k_1$ and $u$ as it depends on the actual rupture times. Similarly, to calibrate $\lambda$, the final rate must be considered which, at the final stress step on the SSM, is also affected by the additional damage caused by the stress increase. However, the MCSR can be considered as a conventional value, as it reaches in the first step, before any

damage is added through the stress stepping. Hence, $k_2$ and $\nu$ can be calculated using the conventional Wilshire approach.

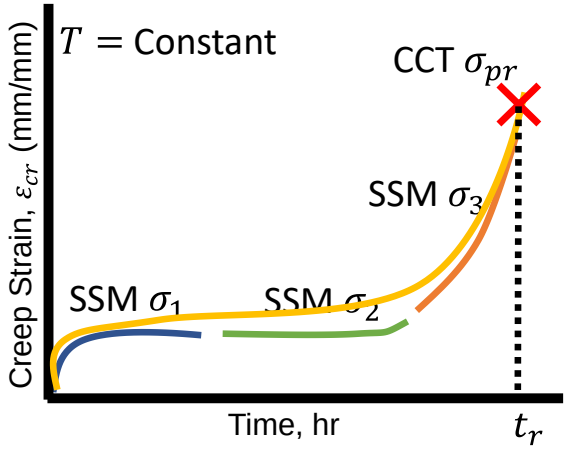


Figure 5.2 - Stress projection of a CCT imitating the rupture path of an SSM curve with multiple steps. Note: the projection stress does not simulate the entire SSM curve.

Although these limitations exist, each SSM has a particular path that is like that of a CCT. In fact, each SSM has a similar rupture to a corresponding CCT with a corresponding stress as shown in Figure 5.2. A stress is projected and mimics the conditions at the last step. The stress projected, $\sigma_{pr}$, therefore, corresponds to an actual rupture time. The projection stress does not attempt to simulate all the SSM, only the last step.

To project this stress a relationship between stress and rupture is considered from the study conducted by Tanks [110]. Tanks considers an energy-based failure criterion and in this study the equation is modified in the following form

$$\sigma_{pr} = \sqrt{\frac{\sigma_R^{\,2}}{\left(\frac{2\sigma_c}{\sigma_0}\right)\left(\frac{t_R}{\tau_0}\right)^n + 1}} \tag{5.2}$$

where $\sigma_R$ and $t_R$ are the stress and rupture time of the SSM experiment, $\sigma_c$ is an activation stress, $\tau_0$ is a reference time, and $n$ is a fitting constant. Note that on the study conducted by Tanks $\sigma_c = D$ and $\sigma_0 = C_0$. The model was modified from those unitless constants and applied real values to project the stress. The reference time considered in this study is the stepping time use in the SSM which is 5 hours. Material constants $\sigma_c$ and $n$ are fitting values estimated to be 4 MPa and 0.5, respectively. After [Eq. (5.2)] is applied, the projected stresses are obtained and shown in Table 5.2. Notice that for SSM_100 the projected stress and rupture time is like the one reported in CCT 300 as shown in Table 5.1. It was expected that if at 300 MPa the rupture time is 89.1 then the projected stress for a rupture of 85.96 should be slightly greater. Therefore, this method is close to actual CCTs as hypothesized. Considering that the projected stresses are related to the rupture times, the Wilshire method for calibrating $k_1$ and $u$ can be followed as well as the given method to calibrate $\lambda$.

Table 5.2 - Projected stress using [Eq. (5.2)].

| Specimen ID | Initial Stress | Rupture | Projection Stress |
|---|---|---|---|
| SSM_100 | 100 | 85.95 | 303.31 |
| SSM_150 | 150 | 68.42 | 316.74 |
| SSM_200 | 200 | 61.25 | 324.16 |
| SSM_250 | 250 | 62.88 | 328.87 |
| SSM_300 | 300 | 52.37 | 332.12 |

**5.6 Stress-Rupture and MCSR Material Constants**

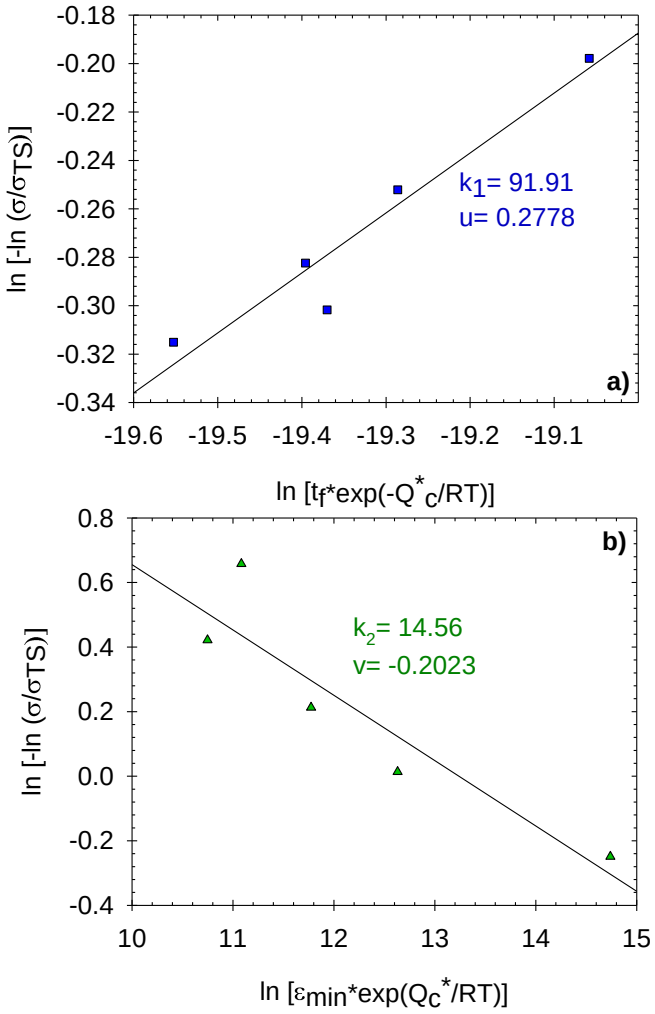


Figure 5.3 - (a) Material constants for stress-rupture $k_1$, $u$ and (b) minimum-creep-strain-rate (MCSR) $k_2$ and $v$ obtained.

Considering that $Q_c^* = 200\ kJ/mol$, the plots to calibrate $k_1$, $u$, $k_2$, and $v$ are shown in Figure 5.3 a) and b). Using the data gather from the SSM experiments at the first step as shown in Table 5.1 $k_2$ and $v$ are obtained. There is one discrepancy where in SSM_300 does not reach the MCSR. Therefore, only for that case the second step is considered which is at 316 MPa. To calibrate $k_1$ and $u$ the stress used is the obtained projection stress from Table 5.2. With the

obtained results predictions for both stress-rupture and MCSR can be made from [Eq. (4.1)] and [Eq. (4.2)]. A summary of such material constants is shown in Table 5.3.

Table 5.3 - Summary of Wilshire material constants for [Eq. (4.1)] and [Eq. (4.2)]

| $Q_c^*$ | $k_1$ | $u$ | $k_2$ | $v$ |
|---|---|---|---|---|
| $kJ/mol$ | $hr^{-u}$ | unitless | $hr^{v}$ | unitless |
| 200 | 91.91 | 0.2778 | 14.56 | -0.2023 |

## 5.7 Stress-Rupture and MCSR Predictions

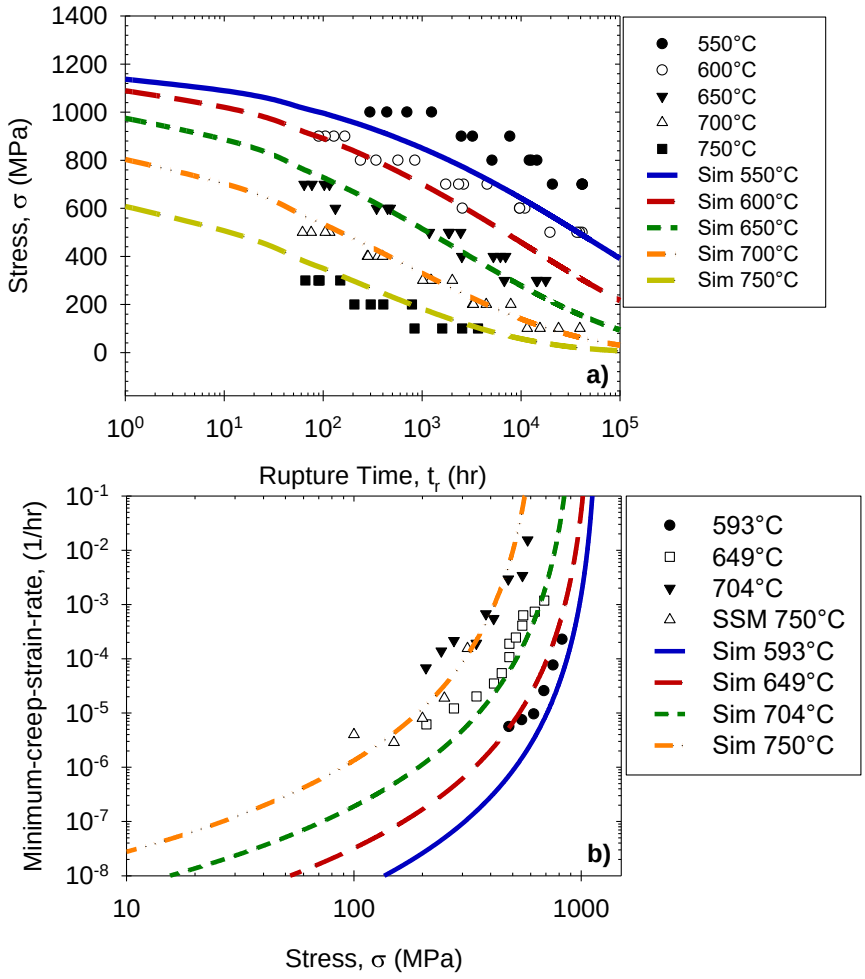


Figure 5.4- (a) Stress-rupture prediction from [Eq. (4.1)] and (b) Minimum-creep-strain-rate from [Eq. (4.2)]. Data for a) is from NIMS and for b) is from Asadi.

Once the material constant $k_1$, $u$, $k_2$, and $v$ are obtained predictions for both stress rupture and MCSR are attained as shown in Figure 5.4 a) and b). These predictions did not use the data sets from their respective sources. Rather, the material constants are shown in Table 5.3, obtained from the SSM experiments. Quantified error is provided in Table 5.4 for both stress rupture and MCSR prediction using the objective function RMSLE [Eq. (4.6)].

The post-audit validated stress-rupture predictions from Figure 5.4a) are made using the NIMS database. The NIMS database contains multiple heat treatments and the actual UTS use for each prediction are the average as shown in Table 3.7. It is shown that predictions are consistent and sit well between the expected uncertainty band. Predictions are made for multiple heat treatments and isotherms using accelerated data. In Table 5.4 it is shown that most of the errors are $< 0.5$ which is typically an acceptable value for root error logarithmic functions (RMSE, RMLSE, etc.) although this can vary for different studies. The Sim $550^{\circ}C$ is the only one that exceeds this parameter. This is expected as the farthest the extrapolative is from the temperature used in calibration ($750^{\circ}C$) the less accurate the results would be. Such trend is consistent for every other isotherm.

The MCSR predictions have more uncertainty as shown in Figure 5.4 b). The data used was obtained from Asadi and the UTS is the same as the one for NIMS, shown in Table 3.7. In this plot, the MCSR data obtained from the SSM experiments is plotted as well and it is shown to have a similar rate to that of temperature $704^{\circ}C$. Comparing the rates of SSM $750^{\circ}C$ and Asadi's $704^{\circ}C$, shows that the SSM material has a greater creep resistance. The trend expected for a material performing at higher temperatures is typically of a higher rate. This adds uncertainty to the model, as the predictions are capturing the performance of a material with a greater creep

resistance. Therefore, predictions are not consistent to that data set and a probabilistic study is needed to reveal the reliability bands to analyze how well between the bands the predictions are. In fact, in Table 5.4 it is shown that every error exceeds 0.5. Regardless, the trend is consistent and is safe to hypothesized that if the materials were of the same quality, even with the SSM method, it would extrapolate with accuracy. Predictions for both stress-rupture and MCSR are consistent, validating the feasibility of the SSM experiments.

Table 5.4 – Stress rupture and MCSR prediction errors using the RMSLE [Eq. (4.6)].

| Stress rupture | Error | MCSR | Error |
|---|---|---|---|
| Sim $550^{\circ}C$ | 0.82 | Sim $593^{\circ}C$ | 0.67 |
| Sim $600^{\circ}C$ | 0.44 | Sim $649^{\circ}C$ | 1.40 |
| Sim $650^{\circ}C$ | 0.25 | Sim $704^{\circ}C$ | 1.63 |
| Sim $700^{\circ}C$ | 0.19 | | |
| Sim $750^{\circ}C$ | 0.38 | | |

### 5.8 Strain Rate and Damage Material Constants

After predictions for stress-rupture and MCSR are made the remaining material constants to predict creep deformation and damage are $\lambda$ and $\phi$. In this study, both $\lambda$ and $\phi$ are obtained numerically using RMSLE [Eq. (4.6)] as the objective function. The error is minimized, and the resulting material constants are given in Table 5.5. Notice there is a significant discrepancy on SSM_250 as it is experimentally proven to not be consistent with the remaining experiments. The remaining error is shown for the entire creep curve.

Table 5.5 – Summary of $\lambda$ and $\phi$ with the error.

| Specimen ID | $\lambda$ | $\phi$ |
|---|---|---|
| SSM_100 | 5.18 | 1.7898 |
| SSM_150 | 4.95 | 1.6450 |
| SSM_200 | 5.25 | 1.8456 |
| SSM_250 | 3.94 | 2.3452 |
| SSM_300 | 5.45 | 1.7514 |

The calibrated material constants obtained from Table 5.5 are used to calibrate Eyring's [Eq. (4.7)] and [Eq. (4.8)] as well as he projection stresses from Table 5.2. Material constants are shown in Table 5.6 obtained through numerical optimization.

Table 5.6 – Eyring's material constants [Eq. (4.7)] and [Eq. (4.8)]

| $\lambda_0$ | $V_\lambda^*$ | $\phi_0$ | $V_\phi^*$ |
|---|---|---|---|
| Unitless | $cm^3$ | Unitless | $cm^3$ |
| 2.89 | 2.60E-23 | 0.026 | 1.54E-22 |

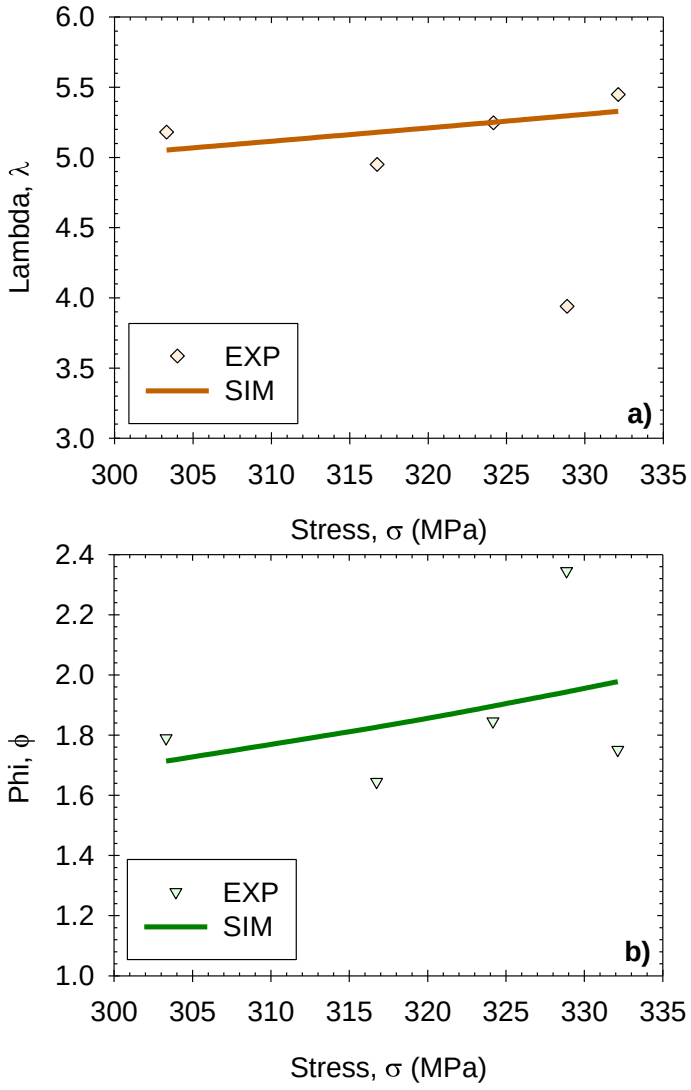


Figure 5.5- (a) Predictions for lambda, $\lambda$ using [Eq.(4.7)] and (b) predictions for phi, $\phi$ using [Eq. (4.8)].

The Eyring model is plotted to predict both $\lambda$ and $\phi$ at multiple stress levels and isotherms if necessary. The plots for these material constants are given in Table 5.6.

## 5.9 Creep Deformation and Damage Predictions

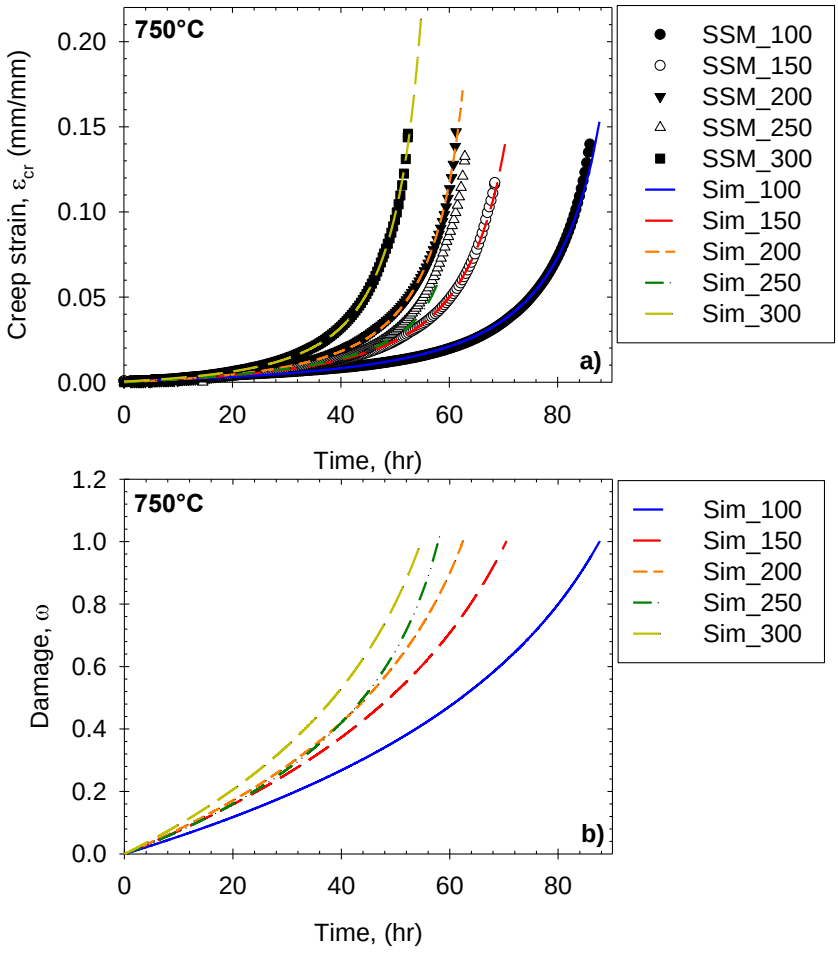


Figure 5.6 – (a) Creep deformation SSM fitting for Inconel-718 using [Eq. (4.3)] and (b) damage predictions using [Eq. (4.4)].

Using the Wilshire material constants obtained shown in Table 5.3 and the Sinh material constants shown in Table 5.5 the SSM data is fitted. The SSM data fits are shown in Figure 5.6 for both a) creep deformation and b) damage using [Eq. (4.3)] and [Eq. (4.4)]. A summary of the error of SSM and the CCT predictions are given in Table 5.7.

Table 5.7 – Error summary for the SSM fitting and the CCT predictions using RMSLE [Eq. (4.6)].

| SSM | Error | CCT | Error |
|---|---|---|---|
| SSM_100 | 0.0660 | CCT_100 | 0.6229 |
| SSM_150 | 0.0395 | CCT_200 | 0.7847 |
| SSM_200 | 0.1082 | CCT_300 | 0.0891 |
| SSM_250 | 0.1299 | CCT_350 | 0.1608 |
| SSM_300 | 0.0138 | | |

It is shown that the model fits the data accurately with a minor overestimation of ductility. In SSM_250, the model reaches failure, damage equal to unity, too fast not allowing a proper ductility estimation. This is due to the uncertainty of this data set. It is expected that SSM_250 sits between SSM_300 and SSM_200 but instead crosses SSM_200. In fact, it has a higher rupture time than SSM_200 which is unrealistic. The model is analytical in nature and the fitting numerical constants, $\lambda$ and $\phi$ , do not capture such behavior. Regardless, the error is in a considerable error range as shown in Table 5.7. From there the model is accurate and consistent fitting the SSM data.

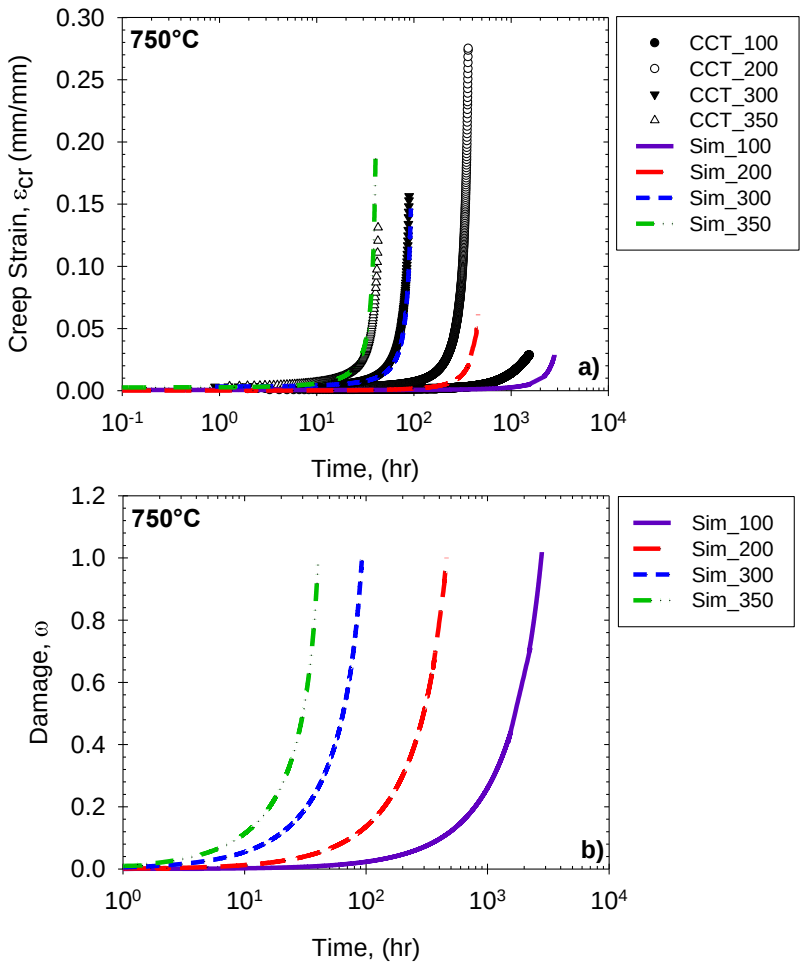


Figure 5.7 - (a) Creep deformation predictions using [Eq. (4.3)]and (b) damage predictions using [Eq. (4.4)]both for CCT data.

Using both the material constants obtained from Table 5.3 and the Eyring model shown in Figure 5.5 predictions for CCT are made. The predictions are shown in Figure 5.7 a) and b) for creep deformation and damage, respectively. In Table 5.7 it is shown that CCT_100 and CCT_200 exceed 0.5. This does not necessarily suggest the model fails as it can be determined qualitatively that the MCSR and rupture times are accurate. In fact, the only non-accurate rupture prediction is CCT_100, which is expected, as it has the longest rupture time (+1500 hours) and is predicted with less than 90 hours of experiments. Rather, most of the error is cause by the ductility. The data

itself shows discrepancy in ductility as it is not consistent with the expected creep trend. Creep ductility increased from CCT_350 to CCT_300 and then to CCT_200. Typically, the lower the stress, the less creep ductility is reported. The model attempts to capture this behavior and it is shown as the error decreases from CCT_200 to CCT_100 which would not be expected to. It is important to considered that the CCT predictions are made blindly as none of the data is used in the calibration process. This validates more the predicting capabilities that can be obtained using both the SSM and WCS model. Using the predictions, the creep resistance of Inconel 718 has been verified as, using this method, multiple parametric studies can be performed to predict the expected creep behavior.

## 5.10 Conclusions

In conclusion, the objective of qualifying the accelerated creep-resistance of Inconel 718 using the WCS model and SSM and predict CCTs has been achieved. This combined methodology has shown the ability to predict stress-rupture for multiple heats and isotherms and MCSR predictions. The model has shown the ability to fit the SSMs properly and can extrapolate and predict CCT.

# CHAPTER 6 ACCELERATED QUALIFICATION OF CREEP-RESISTANT MATERIALS USING A DATUM TEMPERATURE METHOD (DTM) TO CALIBRATION

## 6.1 Introduction

In this Chapter, the datum temperature method (DTM) is applied to the Wilshire-Cano-Stewart (WCS) model to predict rupture time, minimum-creep-strain-rate, and creep deformation. The datum temperature method (DTM) is an alternative calibration approach that can be applied to existing models to improve accuracy and extrapolation reliability. The availability of creep data is limited due to the time and costs associated with testing. Often data is not available at desired operating conditions or creep life. Although accelerated testing methods have been developed, there is still a need to extrapolate creep data to conditions of interest. Conventional time-temperature-parametric (TTP) models have been used but the need for a decision in which TTP model to use for specific materials, the point of convergence, and the inflection points limits their applicability. As an alternative, the DTM is proposed, where all data is transferred to a datum temperature for ease of calibration.

## 6.2 Datum Temperature Method (DTM)

The Datum Temperature method (DTM) proposed by Haque is a calibration approach that can be applied to existing models for accurate predictions and reliable extrapolations [125]. The DTM is a modification of the Parametric-numerical isotherm datum (P-NID) method originally proposed by Bolton [126-127]. Bolton approach is defined in the following steps; a) scrutinize and delete anomalous data, b) plot log stress against log rupture time at each temperature, c) determine a median rupture life at a series of chosen stresses, d) select the parametric equation and transform the median data at all temperatures to a datum temperature, e) if convergence is not reached

through trial variation change the parametric equation, f) use the median data and use interpolative routines to create upper and lower tolerances, g) transform the numerical datum model to each test temperature, h) extrapolate rupture properties according to validity limits of the parametric equation, and lastly, i) plot the scrutinized data and check the consistency of the predictions [128-129]. The P-NID method has successfully been applied to calibrate TTP models such as Larson-Miller, Manson-Haferd, and Orr-Sherby-Dorn for numerous alloys such as 1%CrMoV, 2.25%CrMo, 9%CrMo and 12%CrMoVNb, 304 Stainless Steel, and Inconel 800 [126-129]. Bolton proposed a method for multiple TTP and non-TTP models in his study including the Wilshire model [126].

Haque modified the P-NID method with the DTM approach by simplifying it to three major steps. These steps did not apply the upper and lower tolerances for convergence and are less scrutinizing with the data used for calibration. The DTM's three steps are 1) parametric data transfer, 2) calibration of the model with the transferred data, and 3) parametric model transfer as illustrated in Figure 6.1.

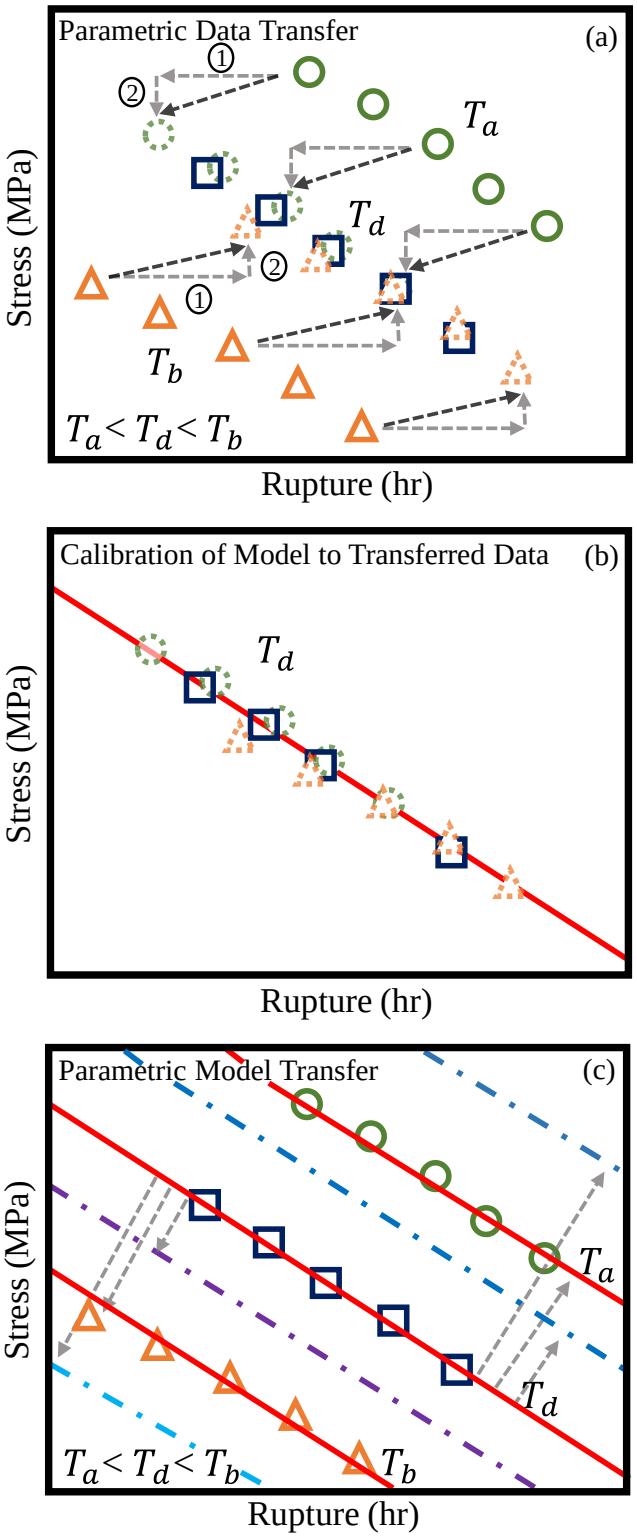


Figure 6.1 - Datum temperature method for the a) parametric data transfer, b) calibration of model to transferred data, and c) parametric model transfer [125].

The parametric data transferred is illustrated in Figure 6.1a where the experimental data at multiple temperatures are transferred to a datum temperature. An example of a creep test at three temperatures is shown in Figure 6.1 where $T_a < T_d < T_b$. The median temperature $T_d$ is selected as the datum temperature; however, the datum temperature can be any temperature of interest. Note that depending on the model (e.g., Wilshire) the data transfer could need both horizontal and vertical data transfer as shown in Figure 6.1a outlined as (1) for the temperature transformation and (2) for the stress transformation. The temperature and stress transformation equations proposed by Bolton for Wilshire are written as follows

$$\ln\left(t_d\right) = \ln\left(t\right) - T_c\left(\frac{1}{T} - \frac{1}{T_d}\right) \tag{6.1}$$

$$\ln\left(S_d\right) = \ln\left(S\right) - \ln\left(\frac{\sigma_{TS}}{\sigma_{TS,d}}\right) \tag{6.2}$$

where $t$ and $t_d$ are the actual and the transferred rupture times respectively, $T$ and $T_d$ are the actual and the datum temperature, $T_c$ is a temperature-independent material constant use for data fitting, $S$ and $S_d$ are the actual and transferred stress, and $\sigma_{TS}$ and $\sigma_{TS,d}$ are the ultimate tensile strength of the actual and datum temperature respectively [126-127]. The transformation equations [Eqs. (6.1)-(6.2)] are calibrated by optimizing $T_c$ to maximize the $R^2$ value of a regression of the transferred data which collapses the data across multiple temperatures into a single line at the datum temperature.

The calibration of the model (e.g., Wilshire) to the transferred data becomes simple as shown in Figure 6.1b where a single isotherm represents all data. The model is calibrated to the isotherm and the material constants are obtained.

The parametric model transfer is illustrated in Figure 6.1c, where the calibrated model is shifted back to the original temperatures. By re-arranging the transformation equations [Eqs. (6.1)-(6.2)], the model is transferred back as follows

$$\ln\left(t\right)=\ln\left(t_d\right)+T_c\left(\frac{1}{T}-\frac{1}{T_d}\right) \tag{6.3}$$

$$\ln\left(S\right)=\ln\left(S_d\right)+\ln\left(\frac{\sigma_{TS}}{\sigma_{TS,d}}\right) \tag{6.4}$$

Interpolations and extrapolations can be obtained by changing the temperature $T$ as shown in Figure 6.1c, where the solid lines are the predictions of the original temperatures $T_a$ and $T_b$, and the dash lines are interpolations and extrapolations.

Haque's study concluded in an accurate prediction of rupture for Inconel 617 using the datum temperature method applied to the Larson-Miller model [125]. Although both P-NID and DTM have proven to accurately predict rupture with a simple calibration approach, MCSR and creep deformation predictions have not been explored. Bolton proposed the Wilshire model together with P-NID [126]. The WCS model that contains Wilshire in its framework can be use together with the DTM approach.

Overall, the DTM offers

- The ability to reduce the test matrix size and duration required for the qualification of creep-resistant materials, where instead of conventional creep testing to 10,000+ hours per heat of material; shorter creep tests over a range of temperatures can be performed and transferred to generate a single isotherm representing data more than 100,000+ hours.

- An easier method to calibrate life predictions models that improves the extrapolations for three times the longest test duration as well as reduces the stress inflection of conventional calibration approaches.
- Maintains accuracy from the P-NID model with a simplified form, enabling predictions even when temperature dependence in rupture life is complex.

### 6.3 Objective of DTM and WCS

There is a need to increase the speed and reduce the costs of qualify the creep-resistance of materials. The datum temperature method offers much in meeting this goal; however, it has yet to be applied to the predictions of MCSR and creep deformation. The WCS model has been demonstrated to accurately predict the creep behavior of multiple alloys and exhibits a straightforward calibration approach which could be suitable for DTM. The combination of the prediction accuracy of WCS and the ease of calibration of the DTM can significantly decrease the time needed to qualify creep-resistant materials.

In this Chapter, the DTM is applied to calibrate the WCS model and predict stress-rupture, minimum-creep-strain-rate, and creep deformation of alloy P91 steel. The data obtain from NIMS is use Figure 3.2. A single Heat (MGC) and form (tube) is employed for the calibration. Post-audit validation is performed where the calibrated model is compared to the remaining Heats to assess the accuracy and extrapolation-ability of the model. For further validation, the calibrated model is applied to predict creep deformation.

### 6.4 Datum Temperature Method for MCSR

The DTM has never been applied to MCSR data. A new transformation equation for MCSR data is introduced as follows

$$\ln\left(\dot{\varepsilon}_{\min,d}\right) = \ln\left(\dot{\varepsilon}_{\min}\right) + T_c^*\left(\frac{1}{T} - \frac{1}{T_d}\right) \tag{6.5}$$

where $\dot{\varepsilon}_{\min,d}$ and $\dot{\varepsilon}_{\min}$ are the transferred and actual MCSR respectively, $T$ and $T_d$ are the actual and the datum temperature, $T_c^*$ is the temperature-independent material constant use for data fitting, and follows a similar framework as [Eq. (6.1)] and is used in conjunction with [Eq. (6.2)]. Note that $T_c^*$ is independent of the $T_c$ used in [Eq. (6.1)]. After model calibration, the model is transferred back by re-arranging [Eq. (6.5)], to furnish

$$\ln\left(\dot{\varepsilon}_{\min}\right) = \ln\left(\dot{\varepsilon}_{\min,\mathrm{d}}\right) - T_c^*\left(\frac{1}{T} - \frac{1}{T_d}\right) \tag{6.6}$$

which is used in conjunction with [Eq. (6.4)].

## 6.5 Material Constant Calibration for DTM

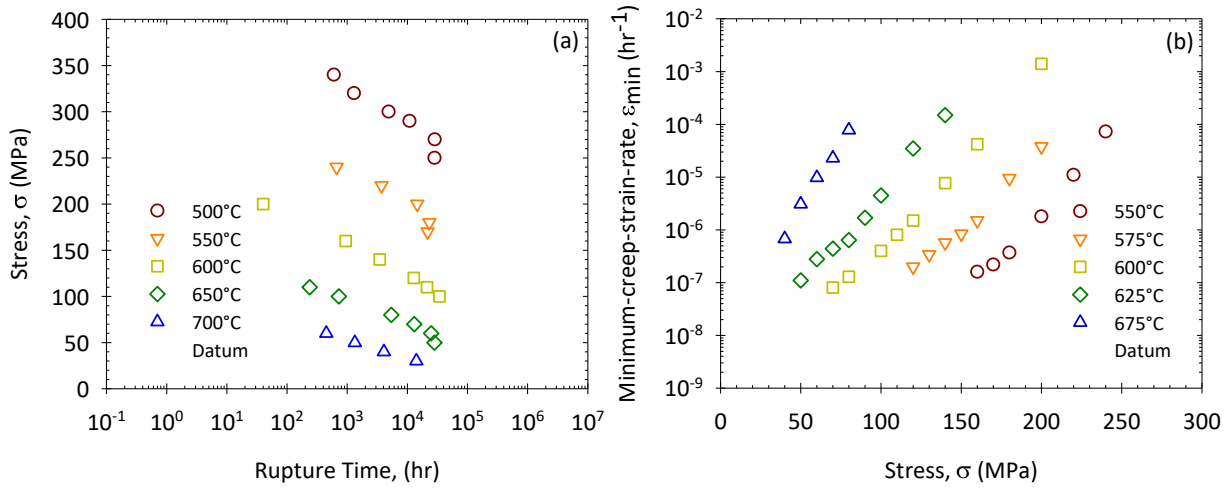


Figure 6.2 – Parametric data transfer for alloy P91 for a) stress-rupture using [Eq. (6.1)] and [Eq. (6.2)] and b) minimum-creep-strain-rate using [Eq. (6.5)] and [Eq. (6.2)].

The DTM is applied to calibrate the WCS model starting with the stress-rupture and MCSR equations. Only data from Heat MGC of alloy P91 is employed during calibration. The stress rupture (500, 550, 650, and 700°C) and MCSR (550, 575, 625, 675°C) data are transferred to the datum temperature of 600°C. Here, 600°C was selected as it is the median temperature of the data. The parametric data transfer of the stress-rupture and MCSR data is shown in Figure 6.2 (a) and (b) respectively. The stress-rupture data transfer is accomplished using [Eq. (6.1)] and [Eq. (6.2)], where $\left(\sigma_{TS}, \sigma_{TS,d}\right)$ are obtained from Table 3.3. Data is transferred using an initial guess $T_c$ that is numerically optimized to obtain $T_c = 3.90\times10^4\ K$ at a maximum $R^2 = 0.9916$. The MCSR data transfer is accomplished using [Eq. (6.5)] and [Eq. (6.2)], Data is transferred using an initial guess $T_c^*$ which is numerically optimized to obtain $T_c^* = 4.00\times10^4\ K$ at a maximum $R^2 = 0.9773$. It is examining that $T_c$ and $T_c^*$ are empirical coefficients and phenomenological in nature. In

literature, there is a wide range of values for temperature-independent material constants such as $T_c$ and $T_c^*$ [125-129]. Although there is a wide range of values, the multiple models used for DTM, and their distinct material constants makes it hard to compare a single value such as $T_c$ or $T_c^*$. It is observed that in Figure 6.2(a) the rupture time is expanded horizontally to match data outside its boundaries. The DTM approach successfully generated data greater than $10^6$ hours. Similarly, in (b), the MCSR, is expanded to $10^{-8}$ which is an accelerated response given from the DTM.

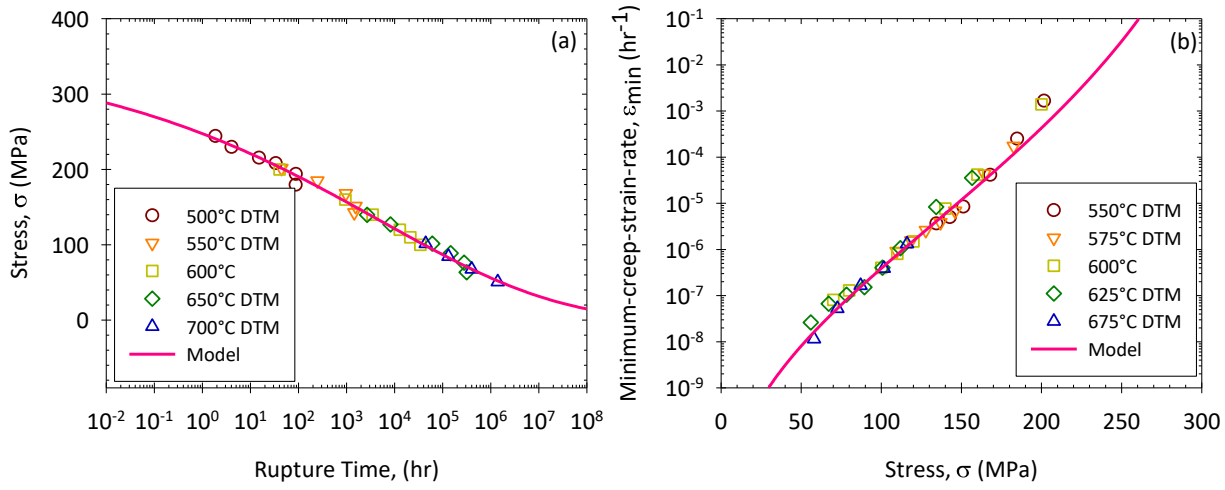


Figure 6.3 – Modeling of the transfer data using WCS [Eq. (4.1)] and [Eq. (4.2)] for a) stress-rupture and b) minimum-creep-strain-rate for alloy P91.

With the data transferred to the datum temperature, the WCS model can now be calibrated. The Wilshire equations for stress-rupture and MCSR [Eq. (4.1)] and [Eq. (4.2)] are calibrated to the transferred data as shown in Figure 6.3(a) and (b) respectively. Examining the predictions in Figure 6.3 it is observed that the predictions take a sigmoidal shape corresponding to the change in dominant creep mechanisms as a function of stress. In Figure 6.3(a) as the stress decreases,

rupture life approaches an infinite number with an asymptote at zero stress and when it approaches the ultimate tensile strength the rupture time equals zero. Similarly, in Figure 6.3(b), it is observed that as MCSR approaches the ultimate tensile strength it becomes a large number and as stress decreases it becomes infinitely small. Notice that at the ultimate tensile strength the MCSR model becomes undefined. There are no inflection points in neither Figure 6.3(a) and (b).

During calibration, creep activation energy of $Q_c^* = 230\ kJ/mol$ was applied which is average from the Heats of P91 Tube. The Wilshire constants universal gas constant ($R = 8.314\ J/mol \cdot K$), $k_1$, $u$, $k_2$, and $v$ are obtained numerically using the following objective function, *OBJ*

$$OBJ = \sqrt{\frac{1}{N}\sum_{i=1}^{N}\left(\frac{\left|\left(X_{\exp,i}\right)-\left(X_{sim,i}\right)\right|}{X_{\exp,i}}\right)} \tag{6.7}$$

where $X_{\exp,i}$ and $X_{sim,i}$ are the experimental and simulated data values respectively and $N$ is the number of data points. The material constants and the residual OBJ are given in Table 6.1. Typically, region-splitting would be applied at this step to obtain two sets of material constants, $k_1$, $u$, $k_2$, and $v$. When transferring the data to a single isotherm, the mechanism change, which is the drive of using region-splitting, is considered just at that datum (600°C). The mechanism from temperature to temperature is going to have a different splitting point which is difficult to capture when numerically optimizing the material constants using just one temperature.

Table 6.1 – Summary of WCS material constants for [Eq. (4.1)] and [Eq. (4.2)].

| Material Constant | Units | Value |
|---|---|---|
| $Q_c^*$ | $kJ/mol$ | 230 |
| $k_1$ | $hr^{-u}$ | 15.04 |
| $u$ | unitless | 0.1173 |
| $k_2$ | $hr^{v}$ | 8.52 |
| $v$ | unitless | -0.1123 |
| *OBJ* (rupture) | unitless | 0.5204 |
| *OBJ* (MCSR) | unitless | 0.5196 |

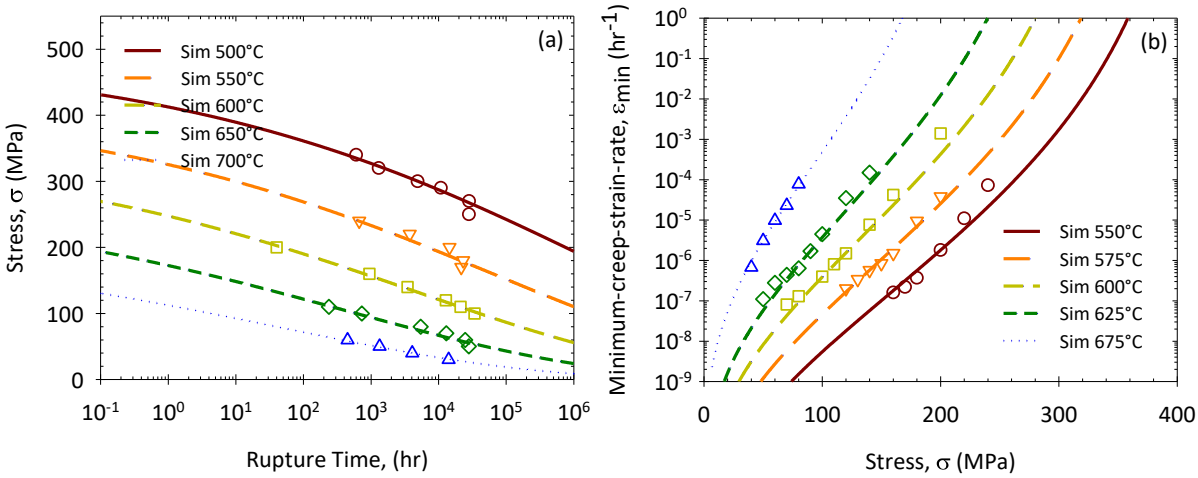


Figure 6.4 – Parametric model transfer for alloy P91 for a) stress-rupture using [Eq. (6.3)] and [Eq. (6.4)] and b) minimum-creep-strain-rate using [Eq.(6.6)] and [Eq. (6.4)].

Finally, the calibrated model is shifted back to the original temperatures using [Eq. (6.3)], [Eq. (6.4)], [Eq.(6.6)] and [Eq. (6.4)] for stress-rupture and MCSR respectively with the results shown in Figure 6.4(a) and (b) respectively. It is observed that the calibrated model is successfully transferred back to the original temperatures with a high degree of accuracy. Furthermore, the

sigmoidal behavior is preserved and matches the trends observed in each isotherm. No inflection points are observed which is ideal for long-term predictions especially at low stress levels. At low stresses rupture time approaches infinity and MCSR becomes infinite small. Approaches the ultimate tensile strength would result in a rupture time of zero and an undefined solution for the MCSR.

The WCS material constants $\lambda$ , $\phi$ are used to obtain creep deformation predictions. The constants are obtained numerically by reducing the error between the simulated strain against the experimental using the following objective function

$$OBJ = \sqrt{\frac{1}{N}\sum_{i=1}^{N}\left(\eta_{\exp,i} - \eta_{\sin,i}\right)^2} \tag{6.8}$$

where $\eta_{\exp,i}$ and $\eta_{sim,i}$ are the experimental and simulated strains respectively and $N$ is the number of data points. Material constants $\lambda$ and $\phi$ are obtained and summarized in Table 6.2.

After the calibration of $\lambda$ and $\phi$ , creep deformation predictions can be obtained

Table 6.2– Summary of material constants $\lambda$ , $\phi$ using objective function [Eq. (6.8)].

| Stress (MPa) | $\phi$ | $\lambda$ | Residual *OBJ* |
|---|---|---|---|
| 100 | 2.15 | 5.55 | 0.0215 |
| 110 | 1.91 | 5.42 | 0.0412 |
| 120 | 1.88 | 5.25 | 0.0513 |
| 140 | 1.75 | 5.18 | 0.0525 |
| 160 | 1.35 | 5.10 | 0.0649 |
| 200 | 1.05 | 5.09 | 0.0661 |

It is noticeable that both $\lambda$ and $\phi$ are dependent on stress and temperature.

An alternative method is proposed to use the DTM together with the Eyring functions to address the temperature and stress dependency. The DTM Eyring transformed functions are of the following form

$$\ln\left(\lambda_d\right) = \ln\left(\lambda\right) + \frac{V_\lambda^*}{k_b}\left(\frac{\sigma}{T} - \frac{\sigma_d}{T_d}\right) \tag{6.9}$$

$$\ln\left(\phi_d\right) = \ln\left(\phi\right) + \frac{V_\phi^*}{k_b}\left(\frac{\sigma}{T} - \frac{\sigma_d}{T_d}\right) \tag{6.10}$$

where $\lambda_d$ and $\phi_d$ are the Sinh material constants at the datum temperature. The calibration approach would take a similar form as shown in Figure 6.1 with $\lambda$ or $\phi$ versus stress. In this study this approach is not used due to lack of data for creep deformation at multiple isotherms. The authors discussed this to propose a framework for a fully DTM calibrated creep deformation model.

## 6.6 Creep Deformation Post-Audit Validation

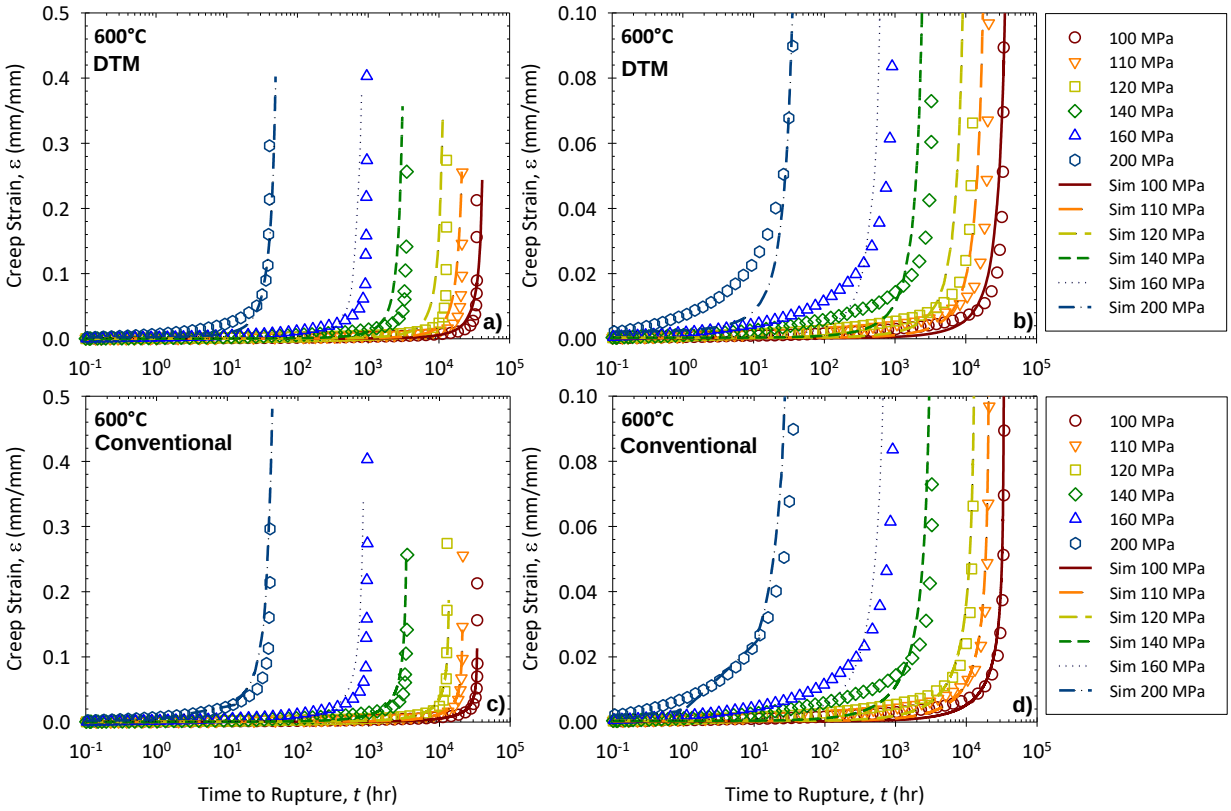


Figure 6.5 – Creep deformation predictions of alloy P91 at 600°C for (a), (b) the DTM calibration approach and (c), (d) for the conventional and previous method employed. Notice: (b) and (d) are zoom-ins from (a) and (c) respectively.

The creep deformation predictions of alloy P91 at 600°C shown in Figure 6.5 for both the DTM and the conventional described in Chapter 4. The predictions are made using [Eq. (4.3)] and [Eq. (4.4)] and the material constants in Table 6.1 and Table 6.2. It is observed that the DTM has a more accurate ductility compared to that of the conventional calibration. Ductility obtained from DTM, especially for 100, 110, and 120 MPa, are more consistent with the data. Notice that the ductility for these three stress levels (100, 110, and 120 MPa), does not reach the rupture point of the data for the conventional approach. Also, the ductility for 200 MPa has a significant decrease,

more in line with the data, in the DTM approach than the conventional approach making DTM superior in the creep ductility prediction. For Figure 6.5 (c) and (d) it is observed that the MCSR fits better. This could be due to the size of the data used for calibration, as the conventional method only used those presented in creep deformation. Region-splitting is not employed, and the error between the conventional method to DTM is minimal. A proposal for future work is to apply multiple datum temperatures at low and high temperatures, this might be difficult if the data set is limited. There is a minimal difference between the two methods, except for the 200 MPa where it is noticeable that the conventional method was superior. The DTM accurately predicted stress-rupture, MCSR, and creep deformation.

The MLE [Eq. (4.5)] of the analytical and DTM calibration approaches are compared in Table 6.3. The average percent difference between them is 23.43% in favor of the conventional approach. While the analytical approach performs marginally better than DTM there are some mitigating circumstances which make DTM preferred. The analytical approach requires a broader data set to be calibrated. To obtain the creep activation energy, multiple data points at multiple isotherms in the same stress ratio must exist. This is difficult due to the amount require for each test. The conventional approach also requires multiple rupture times to calibrate the Wilshire material constants. The more data point the more accurate the predictions are. In this case the DTM can obtain material constants from a limited data set, which is a problem encountered by modelers and design engineers.

Table 6.3– Comparison between the errors of the original calibration approach to the datum temperature method using MLE [Eq. (4.5)]

| Stress (MPa) | Original Method | Datum Temperature Method | Percent Difference (%) |
|---|---|---|---|
| 100 | 17.76 | 18.46 | 3.94 |
| 110 | 17.10 | 19.45 | 13.74 |
| 120 | 18.21 | 20.97 | 15.16 |
| 140 | 20.62 | 22.77 | 10.43 |
| 160 | 19.64 | 22.73 | 15.73 |
| 200 | 12.74 | 23.13 | 81.55 |

### 6.7 Stress-Rupture and MCSR Extrapolations

All predictions and material constants are obtain using a single heat (MGC) of stress rupture and MCSR. This study uses those material constants to extrapolate to other heats and material forms. The objective of this is to prove that the DTM method has an accurate extrapolation capability. In specific applications, calibrations must be made according to the material heats and forms for accurate predictions.

Using the material constants outlined in Table 6.1, extrapolations for both stress-rupture and MCSR are obtained. The mechanical properties for the predictions are obtained from Table 3.3. Note that the average $\sigma_{TS}$ is considered for all predictions across heat treatments and material forms. It is important to notice that if more accurate results are desired according to the application, the activation energy for each form should be used as the Wilshire model is sensitive to heat treatments and material forms.

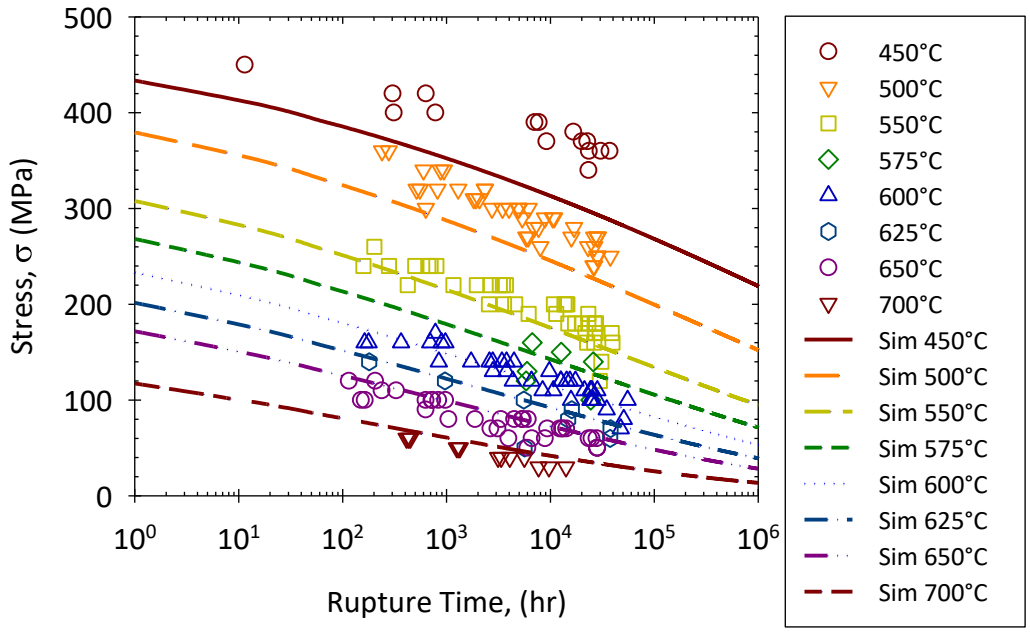


Figure 6.6 – Extrapolation for the entire NIMS stress-rupture data for P91 at multiple heat treatments, material forms, and temperatures. Material constants are obtained from Table 6.1.

The extrapolations for the entire NIMS database stress-rupture data for P91 is shown in Figure 6.6. It is observed that at some temperatures, especially at lower temperatures, there are underpredictions. This behavior is expected as the creep activation energy and the tensile strength of the material is the average of all material forms and temperatures. An example is for $450^{\circ}C$ where the heat treatments (MgA, MgB, and MgC) are different from the one used in calibration. Additionally, the specimen for $450^{\circ}C$ is a plate. A "blind folded" validation is made where the material constants obtained from the calibration are used to obtain predictions. It is important to note that it is more conservative to have underpredictions when making design decisions. A quantitative analysis is performed as well using the objective function shown in [Eq. (6.7)] and the errors are summarized in Table 6.4. There are multiple methods to improve the accuracy of the predictions. For example, instead of using the average $\sigma_{TS}$ the specific one can be used for each

heat treatment. Another method to improve accuracy is to group the data accordingly with each heat treatments so predictions are made under similar conditions. For example, calibrate using heat treatment MGC and predict MGC instead of using multiple heat treatments and material forms. Although this consideration would significantly improve the predictions it is out of the scope of this study. This study only shows the predictive capabilities of the WCS model using DTM. Considerations for improved predictions are dependent on applications picked by design engineers. The model proves to have a good trend of predictions despite the multiple temperatures, heat treatments, and material forms.

Table 6.4– Error summary for stress-rupture extrapolations from Figure 6.6 using [Eq. (6.7)].

| Temperature ($^{\circ}C$) | Residual *OBJ* [Eq. (6.7)] |
|---|---|
| 450 | 0.3929 |
| 500 | 0.3400 |
| 550 | 0.2939 |
| 575 | 0.3954 |
| 600 | 0.2622 |
| 625 | 0.4358 |
| 650 | 0.3392 |
| 700 | 0.4792 |

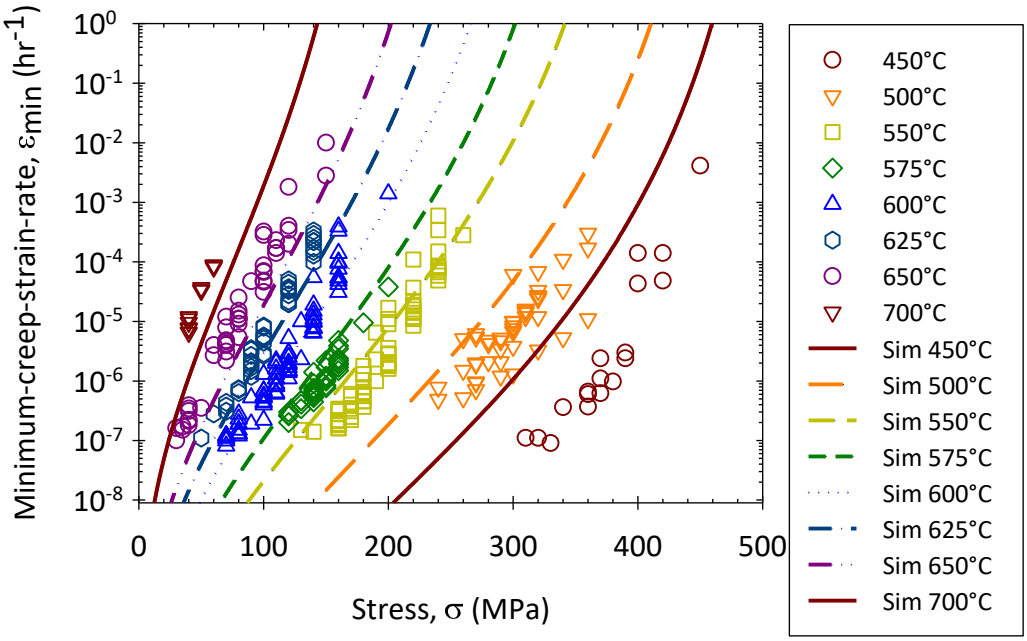


Figure 6.7 - Extrapolation for the entire NIMS minimum-creep-strain-rate data at multiple heat treatments, material forms, and temperatures. Material constants are obtained from Table 6.1.

In this study, the MCSR feature is added to the datum temperature method and extrapolations are shown in Figure 6.7. The introduction of the new feature is successful and follows a similar trend as the stress-rupture predictions. It is noticeable that temperatures $450^{\circ}C$ and $500^{\circ}C$ have significant overpredictions. The lowest temperature used for calibration is $550^{\circ}C$ which significantly impacts the extrapolations. Another point to consider is that $450^{\circ}C$ is a "different material' than the one used for calibration. Temperature $450^{\circ}C$ is a plate in heat treatments MgA, MgB, and MgC. A similar case happens with the underpredictions at $700^{\circ}C$ where the three material forms (tube, plate, and pipe) are predicted with different heat treatments as well. As discussed for the stress-rupture predictions, accuracy can be obtained by using the specific $\sigma_{TS}$ and $Q_c^*$ but this is out of the scope of the research. The summary for the error using [Eq. (6.7)] is shown in Table 6.5.

Table 6.5– Error summary for stress-rupture extrapolations from Figure 6.7 using [Eq. (6.7)].

| Temperature ($^{\circ}C$) | Residual OBJ [Eq. (6.7)]. |
|---|---|
| 450 | 0.4097 |
| 500 | 0.3279 |
| 550 | 0.2939 |
| 575 | 0.2805 |
| 600 | 0.2323 |
| 625 | 0.2718 |
| 650 | 0.4729 |
| 700 | 0.5778 |

## 6.8 Conclusions

The datum temperature method has proven to be accurate to qualify materials to understand long-term creep behaviors. The research objective of applying the datum temperature method to the WCS model to obtain stress-rupture, minimum-creep-strain-rate, and creep deformation for P91 steel is achieved in this study. A single heat treatment MGC for a P91 steel is used to calibrate the datum temperature model using the Wilshire equations. Using the calibration approach described in Figure 6.1 material constants are obtained, and post-audit validation is made to an entire P91 data set with different material forms, heat treatments, and temperatures. Additionally, the material constants are applied to the WCS model to obtain creep deformation predictions. This study has proven that:

- The datum temperature method can predict MCSR using a modified Wilshire equation. This is a new feature that has not been explored until this study for the datum temperature method. The model follows a similar established method, where the calibration approach is simple as the one shown for stress-rupture and has a similar accuracy.

- The material constants obtained from the datum temperature method can be used to obtain predictions of creep deformation with the WCS model. This is a new feature as well, where creep deformation was not explored until this study using this approach. By allowing the model to predict MCSR in a similar way that stress-rupture is obtained, the WCS can predict creep deformation from this behavior. Also new Eyring equations using the datum temperature method are proposed as a framework for a future creep deformation datum temperature approach.
- The datum temperature method is as accurate as conventional calibration approaches and reduces the amount of data needed to obtain long-term extrapolations. In Table 6.3, a comparison from a previous study is made and proves that there is a small difference between accuracy from the conventional methods to the datum temperature method.

## CHAPTER 7 CONCLUSIONS

The objective of showing applications of the Wilshire-Cano-Stewart (WCS) model to predict rupture time, minimum-creep-strain-rate (MCSR), damage, damage evolution, and creep deformation has been accomplished. The goals accomplish were (a) the validation of the framework of the WCS model (b) application of accelerated creep data demonstrated abilities to predict conventional data, and (c) the datum temperature method (DTM) has proven to be a useful tool together with the WCS model to make accurate predictions with limited data sets.

(a) The WCS model demonstrated accurate predictions for stress-rupture, minimum-creep-strain-rate, creep deformation, and damage of alloy P91 across multiple isotherms and stress levels. The WCS model incorporates the Wilshire and Sinh model preserving material constants and calibrations. A major benefit of the model is the explicit stress and temperature dependence from Wilshire and Eyring, which allows accurate interpolations

and extrapolations across isotherms and stresses. The coupled-differential equations of the WCS model are convenient for FEA implementation and are proven to have reasonable mathematical limitations. Parametric simulations validate the ability of the model for interpolations and extrapolations even where data is not provided. The model is a useful tool for design engineers.

(b) Material Inconel 718 is qualified using the accelerated creep test stepped-isostress method (SSM) and the WCS model to predict conventional creep test data (CCT). Predictions of CCT are accurate using less than 90 hours of experiments and the model can predict stress-rupture, MCSR, and creep deformation of multiple heats, isotherms, and stress levels. This method has proven to be beneficial as it can significantly reduce the amount of time required to qualify materials.

(c) The datum temperature method (DTM) has proven to accurately qualify materials together with the WCS model using a single heat of alloy P91 for stress-rupture and MCSR. The model WCS model can predict such behavior as well as creep deformation compared to the conventional approach. This method is beneficial as the amount of data needed for calibration can be significantly reduced to make predictions across heat treatments, isotherms, forms, and stress levels.

The WCS model has proven to be beneficial in multiple applications which can significantly help modelers and design engineers. There are some applications that had yet to be explored that are worth exploring. Future work to expand the applications of the WCS model is to (a) add a multiaxial stress model to allow modeling of compressive stress and dynamic loadings, (b) add the model into a commercial FEA software for complex geometries, (c) add a primary creep model such as McVetty to capture the primary regime of creep on materials with a more significant

primary response, (d) applied the WCS model to a unified viscoplastic constitutive model to capture creep-fatigue interactions.

## REFERENCES


[1] Takasawa, K., & Miki, K. (2011). Development of high-and intermediate-pressure steam turbine rotors for efficient fossil power generation technology. JSW Tech Rev, 20, 15-22.
[2] Haque, M. S. (2018). An Adaptive Creep Modeling Approach Using Metamodeling. The University of Texas at El Paso.
[3] Kassner, M. E., & Smith, K. (2014). Low temperature creep plasticity. Journal of materials research and technology, 3(3), 280-288.
[4] Meher-Homji, C. B., & Gabriles, G. (1998). Gas Turbine Blade Failures-Causes, Avoidance, And Troubleshooting. In Proceedings of the 27th turbomachinery symposium. Texas A&M University. Turbomachinery Laboratories.
[5] Cuzzillo, B. R., & Fulton, L. K. (2014). Failure Analysis Case Studies. Retrieved October 27, 2019, from http://www.berkeleyrc.com/FAcasestudies.html#top.
[6] Fastener failure. MEE Creep Rupture Case Study | MEE Fastener Failure | MEE Failure Analysis. (n.d.). Retrieved March 10, 2022, from https://www.mee-inc.com/case-studies-list/fastener-failure/
[7] Schijve, J. (2003). Fatigue of structures and materials in the 20th century and the state of the art. International Journal of fatigue, 25(8), 679-702.
[8] Janawitz, J., Masso, J., & Childs, C. (2015). Heavy-duty gas turbine operating and maintenance considerations. GER: Atlanta, GA, USA.
[9] Products: Ge Steam Power. gepower-steam. (n.d.). Retrieved March 10, 2022, from https://www.ge.com/steam-power/products
[10] W. Ren, C. Luttrell, Gen IV Materials Handbook Beta Release for Structural and Functional Evaluation, US Department of Energy, 2006, Report No. ORNL/GEN4/LTR-06–027.
[11] ASME, 2015, ASME Boiler and Pressure Vessel Code, Section III, Division 1, Subsection NH – Class 1, Components in Elevated Temperature Service, New York, NY.
[12] Haque, M.S, and Stewart, C. M., 2018, "The Disparate Data Problem: The Calibration of Creep Laws Across Test Type and Stress, Temperature, and Time Scales," Theoretical and Applied Fracture Mechanics, (under review). TAFMEC_2018_166
[13] Haque, M. S., and Stewart, C. M., 2016, "Exploiting Functional Relationships between MPC Omega, Theta, and Sinh-Hyperbolic Models" ASME PVP 2016, PVP2016-63089, Vancouver, BC, Canada, July 17-21, 2016.
[14] Sawada, K., Tabuchi, M., & Kimura, K. (2009). Analysis of long-term creep curves by constitutive equations. Materials Science and Engineering: A, 510, 190-194.
[15] Kraus, H. (1980). Creep analysis. Research supported by the Welding Research Council. New York, Wiley-Interscience, 1980. 263 p.
[16] Lemaitre, J., Chaboche. 1985. J.L. Mechanics of Solid Materials. Paris: Cambridge University Press.
[17] Evans, H. E. (1984). Mechanisms of creep fracture. Elsevier Applied Science Publishers Ltd., 1984,, 319.
[18] Meyers, M. A., & Chawla, K. K. (2008). Mechanical behavior of materials. Cambridge university press.
[19] Frost, H. J., & Ashby, M. F. (1982). Deformation mechanism maps: the plasticity and creep of metals and ceramics. Pergamon press.
[20] Gorash, Y. (2008). Development of a creep-damage model for non-isothermal long-term strength analysis of high-temperature components operating in a wide stress range.

[21] Betten, J. (2008). Creep mechanics. Springer Science & Business Media.
[22] ASTM E139-11. (2011). Standard Test Methods for Conducting Creep, Creep-Rupture, and Stress-Rupture Tests of Metallic Materials. American Society for Testing and Materials, Philadelphia, Pa, 19103.
[23] ASTM E4-21. (2021). Standard Practices for Force Calibration and Verification of Testing Machines. American Society for Testing and Materials, Philadelphia, Pa, 19103.
[24] Material testing machine, creep, and stress rupture testing machine-wance: Material Testing Machines Manufacturer. WANCE. (n.d.). Retrieved April 22, 2022, from http://www.wance.net/creepandstressrupture/
[25] Norton, Frederick Harwood. The Creep of Steel at High Temperature. McGraw-Hill Book Company Incorporated. New York .(1929)
[26] Vega, R, & Stewart, C.M (2019). Development And Application Of Minimum Creep Strain Rate Metamodeling ASME Turbo Expo 2019: Turbomachinery Technical Conference and Exposition Phoenix, Arizona.
[27] Nádai, Arpád, and Arthur M. Wahl. Plasticity. McGraw-Hill Book Company, inc., 1931.
[28] Soderberg, C. R. (1936). The Interpretation of Creep Tests for Machine Design. Trans. ASME, 58(8): 733-743.
[29] McVetty, P. G. (1943). Creep of Metals at Elevated Temperatures-The Hyperbolic Sine Relation between Stress and Creep Rate. Trans. ASME, 65: 761.
[30] Dorn, J. E. (1962). Progress in Understanding High-Temperature Creep, H. W. Gillet Mem. Lecture. Philadelphia: ASTM.
[31] Penny, R. K., and Marriott, D. L., 1995, Design for Creep, Springer, pp.11.
[32] Garofalo, F. (1965). Fundamental of Creep and Creep Rupture in Metals. New York: Macmillan.
[33] Ruano, O. A., J. Wadsworth, and O. D. Sherby. "Harper-Dorn creep in pure metals." Acta Metallurgica 36, no. 4 (1988): pp.1117-1128.
[34] Mohammed, F. A., Murty, K.L. and Morris, J. W., Jr. In: The John E. Dorn Memorial Symposium. Cleveland, Ohio, ASM(1973).
[35] Ashby, M., Shercliff, H., and Cebon, D., Materials: Engineering, Science, Processing and Design. Butterworth-Heinemann, Oxford. 2013.
[36] Ashby, M. F. and Jones, D. R. H., “Engineering Materials 1: An Introduction to Their Properties and Applications”. Oxford: Butterworth Heinemann, 2nd ed., 1996.
[37] Dimmler, G., P. Weinert, and H. Cerjak. "Investigations and analysis on the stationary creep behaviour of 9–12% chromium ferritic martensitic steels." Materials for Advanced Power Engineering 2002 (2002): pp.1539-1550.
[38] Dimmler, G., P. Weinert, and H. Cerjak. "Extrapolation of short-term creep rupture data—The potential risk of over-estimation." International journal of pressure vessels and piping 85, no. 1 (2008): pp.55-62.
[39] Langdon, Terence G. "Creep at low stresses: An evaluation of diffusion creep and Harper-Dorn creep as viable creep mechanisms." Metallurgical and Materials Transactions A 33, no. 2 (2002): pp.249-259.
[40] Yavari, Parviz, and Terence G. Langdon. "An examination of the breakdown in creep by viscous glide in solid solution alloys at high stress levels." Acta Metallurgica 30, no. 12 (1982): pp.2181-2196.
[41] Larson, F. R., Miller, J., 1952, “A time temperature relationship for rupture and creep stress,” Trans. ASME. 74, pp. 765–775.

[42] Monkman, F. C. (1956). An empirical relationship between rupture life and minimum creep rate in creep rupture tests. In proc. ASTM (Vol. 56, pp. 91-103).
[43] Maruyama, K., Abe, F., Sato, H., Shimojo, J., Sekido, N.,Yoshimi, K., 2018, "On the physical basis of a Larson-Miller constant of 20," International Journal of Pressure Vessel and Piping,159, pp. 93–100. doi:10.1016/j.ijpvp.2017.11.013.
[44] Onizawa, T., Wakai, T., Ando, M, Aoto, K, 2008, "Effect of V and Nb on precipitation behavior and mechanical properties of high Cr steel," Nuclear Engineering and Design, 238(2), pp. 408-416. doi: 10.1016/j.nucengdes.2006.09.013
[45] Kumar, J. G., Ganesan, V., Laha, K., and Mathew, M. D., 2013, "Time dependent design curves for a high nitrogen grade of 316LN stainless steel for fast reactor applications," *Nuclear Engineering and Design*, 265, pp. 949-956. doi: 10.1016/j.nucengdes.2013.09.035
[46] Golan, O., Arbel, A., Eliezer, D., & Moreno, D. (1996). The applicability of Norton's creep power law and its modified version to a single-crystal superalloy type CMSX-2. Materials Science and Engineering: A, 216(1-2), 125-130.
[47] Hug, E., Keller, C., Favergeon, J., & Dawi, K. (2009). Application of the Monkman–Grant law to the creep fracture of nodular cast irons with various matrix compositions and structures. Materials Science and Engineering: A, 518(1-2), 65-75.
[48] Kassner, Michael E. Fundamentals of creep in metals and alloys. Butterworth-Heinemann, 2015.
[49] Phaniraj, C., Choudhary, B. K., Rao, K. B. S., & Raj, B. (2003). Relationship between time to reach Monkman–Grant ductility and rupture life. Scripta Materialia, 48(9), 1313-1318.
[50] Burt, H. & Wilshire, B. Metall and Mat Trans A (2006) 37: 1005. https://doi.org/10.1007/s11 661-006-0073-3
[51] Wilshire, B., & Battenbough, A. J. (2007). Creep and creep fracture of polycrystalline copper. Materials science and engineering: a, 443(1-2), 156-166.
[52] Kumar, P., Kassner, M. E., and Langdon, T. G., 2007, "Fifty years of Harper–Dorn creep: a viable creep mechanism or a Californian artifact? "Journal of Materials Science, 42(2), pp. 409-420.
[53] Wilshire, B., & Scharning, P. J. (2007). Long-term creep life prediction for a high chromium steel. Scripta Materialia, 56(8), 701-704.
[54] Wilshire, B., Scharning, P. J., & Hurst, R. (2007). New methodology for long term creep data generation for power plant components. Energy Materials, 2(2), 84-88.
[55] Wilshire, B., & Scharning, P. J. (2008). A new methodology for analysis of creep and creep fracture data for 9–12% chromium steels. International materials reviews, 53(2), 91-104.
[56] Wilshire, B., & Scharning, P. J. (2008). Prediction of long-term creep data for forged 1Cr–1Mo–0· 25V steel. Materials science and technology, 24(1), 1-9.
[57] Whittaker, M. T., & Harrison, W. J. (2014). Evolution of Wilshire equations for creep life prediction. Materials at High Temperatures, 31(3), 233-238.
[58] Evans, M. (2015). Constraints Imposed by the Wilshire Methodology on Creep Rupture Data and Procedures for Testing the Validity of Such Constraints: Illustration Using 1Cr-1Mo-0.25 V Steel. Metallurgical and Materials Transactions A, 46(2), 937-947.
[59] Abdallah, Z., Perkins, K., & Williams, S. (2012). Advances in the Wilshire extrapolation technique—Full creep curve representation for the aerospace alloy Titanium 834. Materials Science and Engineering: A, 550, 176-182.

[60] Zhao, Y. R., Yao, H. P., Song, X. L., Jia, J., & Xiang, Z. D. (2017). On the physical models for predicting the long-term creep strengths and lifetimes of modified 9Cr-1Mo steel. Journal of Alloys and Compounds, 726, 1246-1254.
[61] Gray, V.; Whittaker, M. The changing constants of creep: A letter on region splitting in creep lifing. Mater. Sci.Eng. A 2015, 632, 96–102.
[62] Stewart, C. M., & Gordon, A. P. (2012). Constitutive modeling of multistage creep damage in isotropic and transversely isotropic alloys with elastic damage. Journal of pressure vessel technology, 134(4).
[63] Cedro, V., Garcia, C., & Render, M. (2018). Use of the Wilshire Equations to Correlate and Extrapolate Creep Data of HR6W and Sanicro 25. Materials, 11(9), 1585.
[64] Whittaker, M. T., Evans, M., & Wilshire, B. (2012). Long-term creep data prediction for type 316H stainless steel. Materials Science and Engineering: A, 552, 145-150.
[65] Evans, M. (2016). Incorporating specific batch characteristics such as chemistry, heat treatment, hardness, and grain size into the Wilshire equations for safe life prediction in high temperature applications: An application to 12Cr stainless steel bars for turbine blades. Applied Mathematical Modelling, 40(23-24), 10342-10359.
[66] Ye, W., Hu, X., & Song, Y. (2020). The relationship between creep and tensile properties of a nickel-based superalloy. Materials Science and Engineering: A, 774, 138847.
[67] Evans, M. (2020). Testing Model Structure Through a Unification of Some Modern Parametric Models of Creep: An Application to 316H Stainless Steel. Metallurgical and Materials Transactions A, 51(2), 697-707.
[68] Haque, M. S., & Stewart, C. M. (2019). Comparative analysis of the sin-hyperbolic and Kachanov–Rabotnov creep-damage models. International Journal of Pressure Vessels and Piping, 171, 1-9.
[69] Kachanov, L. M., 1967, The Theory of Creep, National Lending Library for Science and Technology, Boston Spa, England, Chaps. IX, X.
[70] Rabotnov, Y. N., 1969, Creep Problems in Structural Members, North Holland, Amsterdam.
[71] Arnold, S. M., & Kruch, S. (1991). Differential continuum damage mechanics models for creep and fatigue of unidirectional metal matrix composites (No. NAS 1.15: 105213).
[72] Stewart, C. (2013). A Hybrid Constitutive Model for Creep, Fatigue, and Creep-Fatigue Damage.
[73] Chokshi, A. H. (1996). An analysis of creep deformation in nanocrystalline materials. Scripta materialia, 34(12), 1905-1910.
[74] Mesarovic, S. D. (2017). Dislocation creep: climb and glide in the lattice continuum. Crystals, 7(8), 243.
[75] Evans, R., and Wilshire, B., 1985, Creep of metal and alloys, Institute of Metals, London.
[76] Prager, M., 1995, Development of the MPC Omega Method for Life Assessment in the Creep Range, Journal of Pressure Vessel Technology, 117(2), pg. 95-103.
[77] Chaboche, J. L. (1987). Continuum damage mechanics: Present state and future trends. Nuclear Engineering and Design, 105(1), 19-33.
[78] Chaboche, J. L. (1988). Continuum damage mechanics: Part I—General concepts.
[79] Krajcinovic, D., & Lemaitre, J. (Eds.). (1987). Continuum damage mechanics: theory and applications (p. 294). New York: Springer-Verlag.
[80] Wohua, Z., & Valliappan, S. (1998). Continuum damage mechanics theory and application-Part I: Theory. International Journal of Damage Mechanics, 7(3), 250-273.

[81] Duvaut, C, 1976, "Analyse Fonctionnelle—Mecanique des Milieux Continus Homogeneisation," Theoretical and Applied Mechanics, NorthHolland, Amsterdam.
[82] Liu, Y., & Murakami, S. (1998). Damage localization of conventional creep damage models and proposition of a new model for creep damage analysis. JSME International journal series A solid mechanics and material engineering, 41(1), 57-65.
[83] Hyde, C. J., Sun, W., Hyde, T. H., Saber, M., & Becker, A. A. (2014). Application of the Liu and Murakami damage model for creep crack growth predictions in power plant steels.
[84] Stewart, C. M., & Gordon, A. P. (2012). Strain and Damage-Based Analytical Methods to Determine the Kachanov–Rabotnov Tertiary Creep-Damage Constants. International Journal of Damage Mechanics, 21(8), 1186-1201.
[85] Haque, M. S., & Stewart, C. M. (2016, July). Modeling the creep deformation, damage, and rupture of Hastelloy X Using MPC omega, theta, and sin-hyperbolic models. In ASME 2016 Pressure Vessels and Piping Conference. American Society of Mechanical Engineers Digital Collection.
[86] Hossain, M. A., and Stewart, C.M., 2019, "Reliability Prediction of Sine-Hyperbolic Creep-Damage Model using Monte Carlo Simulation Method," ASME PVP 2019, San Antonio, Texas, July 14 – 19, 2019.
[87] Bendick, W., Gabrel, J., Hahn, B., & Vandenberghe, B. (2007). New low alloy heat resistant ferritic steels T/P23 and T/P24 for power plant application. International Journal of Pressure Vessels and Piping, 84(1-2), 13-20.
[88] Pandey, C., Mahapatra, M. M., Kumar, P., & Saini, N. (2018). Some studies on P91 steel and their weldments. Journal of Alloys and Compounds
[89] Guguloth, K., & Roy, N. (2017). Creep deformation behavior of 9Cr1MoVNb (ASME Grade 91) steel. Materials Science and Engineering: A, 680, 388-404.
[90] Panait, C. G., Bendick, W., Fuchsmann, A., Gourgues-Lorenzon, A. F., & Besson, J. (2010). Study of the microstructure of the Grade 91 steel after more than 100,000 h of creep exposure at 600 C. International journal of pressure vessels and piping, 87(6), 326-335.
[91] NIMS- Database for P91 Creep Datasheet 43A, http://smds.nims.go.jp/MSDS/pdf/sheet/C43AJ.pdf, [2022-03-08]
[92] Kimura, K., Kushima, H., & Sawada, K. (2009). Long-term creep deformation property of modified 9Cr–1Mo steel. Materials Science and Engineering: A, 510, 58-63.
[93] Zhang, H., Zhang, K., Lu, Z., Zhao, C., & Yang, X. (2014). Hot deformation behavior and processing map of a γ′-hardened nickel-based superalloy. Materials Science and Engineering: A, 604, 1-8.
[94] Ni, T., & Dong, J. (2017). Creep behaviors and mechanisms of Inconel718 and Allvac718plus. Materials Science and Engineering: A, 700, 406-415.
[95] Stewart, C. M., Hossain, Md.A., Mach, R., Pellicote, J., Alexander, D. & Siddiqui, S.F. (2020). Accelerated Creep Testing of Inconel 718 using the Stepped Isostress Method (SSM). Material Performance and Characterization, ASTM.
[96] Gujrati, R., Gupta, C., Jha, J. S., Mishra, S., & Alankar, A. (2019). Understanding activation energy of dynamic recrystallization in Inconel 718. Materials Science and Engineering: A, 744, 638-651.
[97] Chaturvedi, M. C., & Han, Y. (1989). Creep deformation of Alloy 718. Institute of Aeronautical Materials.

[98] NIMS, 2011, NIMS Creep Data Sheet No.59 - Data sheets on the elevated-temperature properties of Nickel Based 19Cr-18Fe-3Mo-5Nb-Ti-Al Corrosion-Resisting and Heat-Resisting Superalloy Bars (JIS NCF 718-B), National Institute for Materials Science, Japan
[99] Cano, J. A., & Stewart, C. M. (2021). A continuum damage mechanics (CDM) based Wilshire model for creep deformation, damage, and rupture prediction. Materials Science and Engineering: A, 799, 140231.
[100] Hossain, M. A., & Stewart, C. M. (2021). A probabilistic creep model incorporating test condition, initial damage, and material property uncertainty. International Journal of Pressure Vessels and Piping, 193, 104446.
[101] Cano, J. A., & Stewart, C. M. (2019, June). Application of the Wilshire Stress-rupture and Minimum-Creep-Strain-Rate Prediction Models for Alloy P91 in Tube, Plate and Pipe Form. In Turbo Expo: Power for Land, Sea, and Air (Vol. 58684, p. V07AT31A007). American Society of Mechanical Engineers.
[102] Asadi, M., Guillot, D., Weck, A., Hegde, S. R., Koul, A. K., Sawatzky, T., & Saari, H. (2012, July). Constructing a validated deformation mechanisms map using low temperature creep strain accommodation processes for nickel-base alloy 718. In ASME 2012 Pressure Vessels and Piping Conference (pp. 65-73). American Society of Mechanical Engineers.
[103] Hossain, Md.A., Cano, J.A., & Stewart, C. M. (2022). Probabilistic Creep with the Wilshire-Cano-Stewart Model. International Journal of Pressure Vessels and Piping (Submitted)
[104] S.J. Kim, Y.S. Kong, Y.J. Roh, W.G. Kim, Statistical properties of creep rupture data distribution for STS304 stainless steels, Mater. Sci. Eng. A. 483–484 (2008) 529–532. https://doi.org/10.1016/j.msea.2006.12.153.
[105] J. Moteff, R.K. Bhargava, W.L. McCullough, Correlation of the hot-hardness with the tensile strength of 304 stainless steel to temperatures of 1200 C, Metall. Trans. A. 6 (1975) 1101.
[106] Samadi, S., Jin, S., Gruber, D., Harmuth, H., & Schachner, S. (2020). Statistical study of compressive creep parameters of an alumina spinel refractory. Ceramics International, 46(10), 14662-14668.
[107] Patel, S. J., DeBarbadillo, J. J., Baker, B. A., & Gollihue, R. D. (2013). Nickel base superalloys for next generation coal fired AUSC power plants. *Procedia Engineering*, *55*, 246-252.
[108] Sun, F., Gu, Y. F., Yan, J. B., Xu, Y. X., Zhong, Z. H., & Yuyama, M. (2016). Creep deformation and rupture mechanism of an advanced wrought NiFe-based superalloy for 700° C class A-USC steam turbine rotor application. *Journal of Alloys and Compounds*, *687*, 389-401.
[109] Giannopoulos, I. P., & Burgoyne, C. J. (2011). Prediction of the long-term behaviour of high modulus fibres using the stepped isostress method (SSM). Journal of materials science, 46(24), 7660-7671.
[110] Tanks, J., Rader, K., Sharp, S., & Sakai, T. (2017). Accelerated creep and creep-rupture testing of transverse unidirectional carbon/epoxy lamina based on the stepped isostress method. Composite Structures, 159, 455-462.
[111] Robert Purgert, Jeffrey Phillips, Howard Hendrix, John Shingledecker, and James Tanzosh, 2016 “Materials for Advanced Ultrasupercritical Steam Turbines - Advanced Ultra-supercritical
[112] Verma, A. K., Hawk, J. A., Romanov, V., & Carter, J. L. (2020). Predictions of long-term creep life for the family of 9–12 wt% Cr martensitic steels. Journal of Alloys and Compounds, 815, 152417.

[113] National Science and Technology Council, “Advanced Manufacturing: A Snapshot of Priority Technology Areas Across the Federal Government,” Office of Science and Technology Policy, Washington, DC, 2016.
[114] Viswanathan, R., and Foulds, J., 1998, “Accelerated Stress Rupture Testing for Creep Life Prediction – Its Value and Limitations,” Journal of Pressure Vessel Technology, 120(2), pp. 105-115.
[115] Nakada, M. (2019). Accelerated testing methodology for long-term creep and fatigue strengths of polymer composites. In Creep and Fatigue in Polymer Matrix Composites (pp. 325-348). Woodhead Publishing.
[116] Luo, W., Wang, C., Hu, X., & Yang, T. (2012). Long-term creep assessment of viscoelastic polymer by time-temperature-stress superposition. Acta Mechanica Solida Sinica, 25(6), 571-578.
[117] Peng, Q., Zhu, Z., Jiang, C., & Jiang, H. (2019). Effect of stress relaxation on accelerated physical aging of hydrogenated nitrile butadiene rubber using time-temperature-strain superposition principle. Advanced Industrial and Engineering Polymer Research, 2(2), 61-68.
[118] Jazouli, S., Luo, W., Bremand, F., and Vu-Khanh, T., 2005, “Application of time–stress equivalence to nonlinear creep of polycarbonate,” Polymer testing, 24(4), pp. 463-467.
[119] Luo, W. B., Yang, T. Q., and An, Q. (2001). Time-temperature-stress equivalence and its application to nonlinear viscoelastic materials. Acta Mechanica Solida Sinica, `(3), 195-199.
[120] Luo, W. B., Wang, C. H., and Zhao, R. G., 2007, “Application of time-temperature-stress superposition principle to nonlinear creep of poly (methyl methacrylate),” Key Engineering Materials, 340, pp. 1091-1096.
[121] Giannopoulos, I. P., and Burgoyne, C. J., 2012, “Accelerated and real-time creep and creep-rupture results for aramid fibers,” Journal of Applied Polymer Science, 125(5), pp. 3856-3870.
[122] Tanks, J.D., Rader, K., and Sharp, S.R., 2015, “Accelerated creep testing of CFRP with the stepped isostress method,” Mechanics of Composite and Multi-functional Materials, 7(46), Springer International Publishing, Editor K. Zimmerman.
[123] Hadid, M., Guerira, B., Bahri, M., & Zouani, A. (2014). Assessment of the stepped isostress method in the prediction of long-term creep of thermoplastics. Polymer testing, 34, 113-119.
[124] Mach, R., Pellicotte, J., Haynes, A., & Stewart, C. (2019, June). Assessment of Long-Term Creep Using Strain Rate Matching from the Stepped Isostress Method. In Turbo Expo: Power for Land, Sea, and Air (Vol. 58684, p. V07AT31A011). American Society of Mechanical Engineers.
[125] Haque, M. S. (2020, August). Extrapolation of Creep Rupture Data Using Parametric Numerical Isothermal Datum (P-NID) Method for Inconel 617. In Pressure Vessels and Piping Conference (Vol. 83860, p. V006T06A036). American Society of Mechanical Engineers.
[126] Bolton, J., 2013, “A visual perspective of creep rupture extrapolation, *“Materials at High Temperatures*,30(2), pp. 87-98.
[127] Bolton, J. (2014). The potential for major extrapolation of creep rupture and creep strain data. Materials at High Temperatures, 31(2), 109-120.
[128] Bolton, J. (2017). Reliable analysis and extrapolation of creep rupture data. International Journal of Pressure Vessels and Piping, 157, 1-19.
[129] Bolton, J. (2019). Addendum to: Reliable analysis and extrapolation of creep rupture data. International Journal of Pressure Vessels and Piping, 172, 348-359.

## VITA

My name is Jaime Aaron Cano Escamilla. I have earned my Bachelor and Master of Science degrees in Mechanical Engineering at the University of Texas at El Paso (UTEP). I graduated with honors in May 2018 from my bachelor's and in December 2019 from my master's degree. This dissertation is the culmination of my graduate studies and is a requirement for the completion of my doctoral degree in mechanical engineering at UTEP. Through my graduate studies I have been a member of the Materials at Extremes Research Group (MERG) under the supervision of my mentor Dr. Calvin M. Stewart. My area of expertise is in constitutive creep modeling of metallic alloys and the topics covered through this dissertation are creep, modeling, rupture-time, minimum-creep-strain-rate, continuum mechanics, rupture life prediction, accelerated testing method, and numerical methods. Related to this work are three major publications completed through my graduate studies:

1) Cano, J. A., & Stewart, C. M. (2021). A continuum damage mechanics (CDM) based Wilshire model for creep deformation, damage, and rupture prediction. Materials Science and Engineering: A, 799, 140231.
2) Cano, J. A., & Stewart, C. M. (2022). Accelerated Creep Test Qualification of Creep-Resistance Using the Wilshire–Cano–Stewart Constitutive Model and Stepped Isostress Method. Journal of Engineering for Gas Turbines and Power, 144(1).
3) Cano, J. A., & Stewart, C. M. (2022). Accelerated Qualification of Creep-Resistant Materials using a Datum Temperature Method (DTM) to Calibration. International Journal of Pressure Vessels and Piping.

Contact Information: Jaime Aaron Cano, institutional email: jacano2@miners.utep.edu and personal email is eng.jacano2@gmail.com